ALMA MATER STUDIORUM
UNIVERSITÀ DI BOLOGNA

DOTTORATO DI RICERCA IN

INGEGNERIA ELETTRONICA, TELECOMUNICAZIONI E TECNOLOGIE DELL'INFORMAZIONE

Ciclo 36

Settore Concorsuale: 09/E3 - ELETTRONICA

Settore Scientifico Disciplinare: ING-INF/01 - ELETTRONICA

PERFORMANCE OPTIMIZATION METHODS FOR MULTIPLE-INPUT 5G TRANSMITTERS

Presentata da: Mattia Mengozzi

Coordinatore Dottorato

Aldo Romani

Supervisore

Alberto Santarelli

Co-supervisore

Gian Piero Gibiino

Esame finale anno 2024

Contents

Abstract v

Acknowledgment vii

List of Abbreviations ix

List of Figures xi

List of Tables xxi

1 Introduction 1

1.1 Overview . . . 1

1.2 Power Amplifiers Metrics . . . 3

1.2.1 Modulated Signal Characteristics . . . 3

1.2.2 Linearity Metrics . . . 5

1.2.3 Power and Efficiency metrics . . . 7

1.3 Digital Predistortion . . . 8

1.3.1 Behavioral Modeling . . . 8

1.3.2 DPD Model Identification . . . 13

1.3.3 Indirect Learning . . . 15

1.3.4 Direct Learning . . . 17

1.4 Device Parameters Optimization . . . 20

1.4.1 Single-Objective Optimization Problem . . . 20

1.4.2 Gradient-Based Algorithm . . . 22

1.4.3 Derivative-Free Algorithm . . . 22

1.4.4 Multi-Objective Optimization Problem 23
1.5 Multiple-Input Power Amplifiers Architectures 24
1.5.1 Beamforming Arrays 24
1.5.2 Supply Modulated PAs 25
1.5.3 Load-Modulated PAs 28
1.6 State of the Art 30
1.7 Thesis Organization 31

2 Beamforming Array **35**
2.1 Problem Statement 35
2.2 Beam-Dependent Linearization 35
2.2.1 DPD architecture 35
2.2.2 Feature-based Model Reduction 37
2.3 Over-the-Air Measurement Setup 39
2.4 Experimental Results 41
2.4.1 DPD Identification 41
2.4.2 DPD Validation 42
2.5 Computational Complexity Analysis 45
2.6 Achievements 47

3 Supply-Modulated Power Amplifier **49**
3.1 Problem Statement and State of the Art 49
3.2 Joint Dual-Input Digital Predistortion 52
3.2.1 Multi-objective Optimization 52
3.2.2 Surrogate Modeling 54
3.2.3 SuMo-based MOO algorithm 54
3.2.4 Multi-Objective Optimization Implementation 56
3.3 Measurement Setup 61
3.3.1 Synchronism between LF and RF Branches 63
3.4 Preliminary Static Analysis 65
3.5 Choice of the DPD Model 70
3.6 Optimization Results 71

3.6.1 MOO-based Static Shaping Table . . . 71
3.6.2 MOO-based joint LF/RF Digital Predistortion . . . 77
3.6.3 Iterative behavior . . . 80
3.7 Comments on the Residual Distortion . . . 82
3.8 Achievements . . . 84

4 Simulation-based optimization of the DIDPA 87
4.1 Introduction . . . 87
4.1.1 DIDPA Design . . . 88
4.1.2 Optimization Problem . . . 89
4.1.3 Quasi-Static Surrogate Modeling . . . 93
4.2 Coordinate Descent Optimization . . . 95
4.3 Bayesian Optimization . . . 99
4.4 Multi-Objective Bayesian Optimization . . . 100
4.5 DIDPA Performance under Wideband Modulation . . . 105
4.6 Conclusion . . . 109

5 DIDPA Optimization on Direct Measurements 111
5.1 Problem Statement . . . 111
5.2 Millimeter-wave MIMO VNA Setup . . . 113
5.2.1 Measurement system . . . 113
5.2.2 Dual Input Signal Control . . . 114
5.3 Optimization Problem Statement . . . 117
5.3.1 Dual Input - Single Output Device-Under-Test . . . 117
5.3.2 Digital Splitter Parametrization . . . 118
5.3.3 Digital Predistortion Architecture . . . 120
5.3.4 Optimization Algorithm . . . 121
5.4 Bayesian Optimization . . . 123
5.4.1 Quasi-Static Model Optimization . . . 123
5.4.2 Optimization Applied to Modulated Acquisitions . . . 124
5.5 Circuit Test with WB Measurement . . . 125
5.5.1 DIDPA Linearization . . . 125

5.5.2 Selection of Input Splitting under Wideband Modulation 126
5.6 Quasi-Static Model Optimization Results 129
5.6.1 Constant Digital Splitter 129
5.6.2 Static Nonlinear Digital Splitter 131
5.7 BO on Direct Modulated Measurements Results 135
5.7.1 Constant Digital Splitter 135
5.7.2 Static Nonlinear Digital Splitter 136
5.8 Achievements 139

6 Conclusions and Future Works **143**
6.1 Main Achievements 143
6.2 Possible Topics for Future Work 145
6.3 List of Publications 147
6.3.1 International Journals 147
6.3.2 International Conferences 147

Abstract

The rapid evolution of telecommunication systems has led to the introduction of new generations of wireless communication standards, which require signals with wide bandwidth (BW) and a very high peak-to-average power ratio (PAPR) to improve spectral efficiency and maximize data speed. However, such advancements can only occur through the evolution of radio frequency (RF) and microwave devices, which should be capable of operating at higher frequencies, greater BWs, and with higher efficiency than before. To meet these demanding specifications, transmitter architectures evolved from a single linear RF power amplifier (PA) to more complex topologies.

The objective of the thesis is to analyze the possibility of exploiting the additional degrees of freedom in multi-input (MI) PA topologies to improve their performance in terms of trade-offs among the main figures of merit: linearity, efficiency, and power. The proposed algorithms were tested on three different topologies of MI PAs, each presenting different optimization challenges and objectives.

On a PA array, a beam-dependent digital predistortion (BD-DPD) algorithm was tested to enhance the linearity of the system under varying PA load conditions, by adjusting the beam direction. The method is based on machine learning and allows a low-complexity real-time update of the DPD coefficients by exploiting feature-based model reduction. The validation is performed through over-the-air measurements of a 1x4 array operating at 28 GHz with 100-MHz of modulated BW.

On a supply-modulated PA (SM-PA), a gradient-based multi-objective

optimization (MOO) algorithm was applied to optimize the trade-off between linearity and efficiency of the PA. To avoid dealing with an unbearably high number of experimental acquisitions, MOO is made feasible by fast simulation of an empirical surrogate model of the PA, which is progressively refined from a reduced set of iterative acquisitions. The proposed technique enables the adoption of a dynamic supply shaping function, and it automatically accounts for the signal statistics. Eventually, the method outperforms classical SM approaches yet using a DPD of the same order. This is demonstrated by the experimental results on a Gallium Nitride SM-PA operating at 3.5 GHz in the presence of OFDM-like high-PAPR modulated signals with 10-MHz and 20-MHz BWs.

Finally, a derivative-free algorithm, the Bayesian optimization, was tested on a multi-input load-modulated amplifier, specifically on a dual-input Doherty PA (DIDPA) targeting 100-MHz modulated BW at 24 GHz. The optimization focuses on improving power added efficiency (PAE) while maintaining linearity with DPD linearization. A joint optimization considers the mutual effect of DPD linearization and PAE-maximization. Validation is done with a multiport on-wafer measurement system using a vector network analyzer for wideband characterization of a millimeter-wave DIDPA. To realize this, a dual-input control algorithm is proposed for user-defined control across a 600-MHz BW with a central frequency of 24 GHz between the inputs of the DIDPA.

Acknowledgment

The work would not have been possible without the support from the group at EDM-LAB research group of the University of Bologna (Unibo) and the RF Power Lab Group at the Ferdinand Braun Institut (FBH) in Berlin. The author would also like to thank the Microwave Engineering Center for Space Applications (MECSA) and WIN Semiconductors for providing access to the NP15-00 150-nm GaN-on-SiC process and the model used to design the dual-input Doherty power amplifier at Unibo. The FBH characterization setup used in Chapter 5 was funded by the German Federal Ministry of Education and Research under the project reference 16FMD02 (Forschungsfabrik Mikroelektronik Deutschland). The author would like to thank TMYTEK and bq-microwave for providing the TMYTEK hardware used to realize the over-air-setup.

List of Abbreviations

ACPER adjacent channel error power ratio
ACPR adjacent channel power ratio
AWG arbitrary waveform generator
BA beam adapter
BD beam-dependent
BO Bayesian optimization
BW bandwidth
CE circuit envelope
CO constrained optimization
CW continuous-wave
DIC dual-input control
DISO dual-input single-output
DLA direct learning architecture
DIDPA dual-input Doherty power amplifier
DPA Doherty power amplifier
DUT device under test
EER envelope elimination and restoration
ET envelope tracking
EVM error vector magnitude
FLOPs floating point operations per seconds
FoM figure of merit
GaN gallium nitride
GMP generalized memory polynomial

ILA indirect learning architecture
ILC iterative learning control
LSQ least square
LF low-frequency
MI multiple-input
MIMO multiple-input multiple-output
MISO multiple-input single-output
MMIC microwave monolithic integrated circuits
MP memory polynomial
MOO multi-objective optimization
NMSE normalized mean square error
OTA over-the-air
OFDM orthogonal frequency division multiplexing
PAPR peak-to-average power ratio
PA power amplifier
PAE power added efficiency
PDK process design kit
PDS power spectral density
PSD probability density function
QSM quasi-static model
RF radio frequency
SM supply-modulation
SM-PA supply-modulated power amplifier
ST shaping table
SISO single-input single-output
SuMo surrogate model/modeling
VNA vector signal analyzer

List of Figures

1.1 Generic single-transistor linear PA electrical scheme 7
1.2 Class AB PA with high-level gain compression. (a) NMSE vs number of parameters of the model, (b) NMSE vs computational complexity measured in number of floating point operations per seconds (FLOPs), (c) adjacent channel error power ratio (ACPER) vs FLOPs [1]. 11
1.3 AM/AM characteristics of each block of the predistorter-PA chain. 14
1.4 Indirect learning Architecture implemented realized through the (a) analytical model inversion and the (b) postdistorter identification 16
1.5 Direct Learning Architecture 18
1.6 Iterative learning control architecture. 18
1.7 a)Envelope Elimination and Restoration b)Envelope Tracking [2]. 26
1.8 PA gain characteristic and PAE with various drain supply voltages (from 10 to 28 V). 27
1.9 Comparison between the distorted and linearized output signal probability density function (PDF) of a given PA with its PAE characteristic. 32

2.1 Block diagram of the adopted DPD configuration for active beamforming arrays. 36

2.2 (a) Real and (b) imaginary part of the first DPD coefficient while the beam angle θ and the input signal PAPR θ change. The surface is a spline interpolation. 37

2.3 (a) Block diagram and (b) photo of the OTA measurement setup. 40

2.4 Array operating conditions used as a pre-training set (blue circles) and as a validation set (red crosses). 42

2.5 (a) Singular values of matrix $\boldsymbol{D}$ as from Algorithm 1. (b) Model fitting error (NMSE) of the GMP-based predistorter. . 43

2.6 Cubic polynomial and spline interpolation of the first reduced feature across all tested conditions. (a) Real and (b) imaginary part. 43

2.7 DPD performance comparison. (a) ACPR and (c) EVM in the validation points plotted across beam angle. (b) ACPR and (d) EVM in the validation points plotted across PAPR. The continuous line indicates the average value in a given DPD configuration across all tested operating conditions. 44

2.8 (a) Gain and (b) phase characteristics of the predistorted and non-predistorted array in the test condition P as from Fig. 2.4 ($\theta = 27°$, PAPR = 8.2 dB). 46

2.9 Spectrum of the predistorted and non-predistorted array in the condition P as from Fig. 2.4 ($\theta = 27°$, PAPR = 8.2 dB). . 47

3.1 Block diagram for ET PA linerization with (a) SISO predistorter and (b) single-input dual-output predistorter with joint RF-LF coefficient learning. 51

3.2 Flow chart of the surrogate-based MOO algorithm for joint RF input/supply DPD. 57

3.3 Block diagram (a) and photo (b) of the measurement setup for supply-modulated PAs used to perform the experiments. . 62

3.4 Result of the delay compensation. The reported values for the input controls are the ones realized at the PA ports, in linear scale (V). 64

3.5 Output power (a), static gain (b)-(c) and PAE (d) characteristics of the SM-PA for different values of the RF and LF control voltages. The RF input power ranges from 2.6 dBm to 28.6 dBm (shown in linear scale on the x-axis). The LF control is swept in order to obtain measured the drain voltages in the 8 V (black) to 30 V (red) range. The Rayleigh probability density function for an input rms power of 19 dBm of interest is shown in (e). 65

3.6 Rayleigh probability density function for an input rms power of 19 dBm of interest. 66

3.7 Static supply-shaping strategies for the SM-PA under test: fixed supply (28 V, black), iso-gain (12.5 dB, red) and maximum PAE (cyan). The RF input power ranges from 2.6 dBm to 28.6 dBm (shown in linear scale on the x-axis). Gain magnitude (purple) and PAE (green) contours with respect to the control variables are also reported. 67

3.8 RF Output Power, NMSE and PAE trade-offs for fixed supply (a-d), iso-gain (b-e) and (c-f) maximum PAE shaping strategies. Squares indicate the non-linearized case, circles indicate the statically predistorted case using a 5-th order polynomial. 68

3.9 MOO-based Pareto front for maximum PAE and constrained NMSE using a static ST (dark blue x), compared with the standard iso-gain ST (@ 12.5 dB) with SISO DPD (red circles) and maximum PAE ST with SISO DPD (light blue +). The corresponding DPD complexity is reported in Table 3.1. The test signal is a 10-MHz random-phase 1k-tone with PAPR = 9.3 dB. 72

3.10 MOO-based Pareto front for maximum PAE and constrained NMSE using a static ST (dark blue x), compared with the standard iso-gain ST (@ 12.5 dB) with SISO DPD (red circles) and maximum PAE ST with SISO DPD (light blue +). The DPD complexity used is higher than the one in Fig. 3.9 (see Table 3.1). The test signal is a 10-MHz random-phase 1k-tone with PAPR = 9.3 dB. 73

3.11 MOO-based Pareto front for maximum PAE and constrained NMSE using a static ST (dark blue x), compared with the approach in [3] (purple squares), the standard iso-gain ST (@ 12.5 dB) with SISO DPD (red circles), and maximum PAE ST with SISO DPD (light blue +). The test signal is a 20-MHz random-phase 2k-tone with PAPR = 10.11 dB. 73

3.12 Comparison among the PAE/NMSE (a) and RF output power/NMSE (b) Pareto fronts obtained by the MOO algorithm by maximizing PAE under constrained NMSE and fixed linearization gain. Three cases are reported: static LF predistorter (blue crosses), LF predistorter with memory (red pluses), LF predistorter with memory at a lower RF output power level. . . . 78

3.13 Different supply control functions obtained with the MOO (dark red, black, blue, and green curves) compared to the classical shaping tables from the static PA analysis (red and light blue lines). The RF input power ranges from 2.6 dBm to 28.6 dBm (shown in linear scale on the x-axis). 79

3.14 Time frame of the LF input control waveform at different iterations, corresponding to the operating point P1 in Fig. 3.9. The test signal is a 10-MHz random-phase 1k-tone with PAPR = 9.5 dB. 80

3.15 MOO iterative behaviour corresponding to the non-dominated solution P1 in Fig. 3.9. The values of (a) PAE and NMSE (b) at each iteration for the SuMo (red) and the measured PA (blue) are compared. Black dashed line in (b) identifies the level of the fixed linearity constraint. 81

3.16 (a) AM/AM characteristics, (b) AM/PM characteristics, and (c) RF output spectra at different iterations. The test signal is a 10-MHz random-phase 1k-tone with PAPR = 9.5 dB. . . . 82

3.17 (a,d) Gain characteristics, (b,e) AM/PM characteristics, and (c,f) RF output spectra for two examples of non-dominated operating points (blue: initial conditions; red: last iteration). Operating point P9 in Table 3.1 (10-MHz OFDM-like signal with PAPR=9.5 dB: PAE=38.1%, RF P_{out}=31.0 dBm, NMSE=-39.7 dB) in top row; Operating point P13 in Table 3.2 (20-MHz OFDM-like signal with PAPR=10.1 dB: PAE=18.4%, RF P_{out}=30.6 dBm, NMSE=-39.8 dB) in bottom row. 83

3.18 (a,d) Gain characteristics, (b,e) AM/PM characteristics, and (c,f) RF output spectra before and after ILA DPD at constant 28V supply. (10-MHz OFDM-like signal with PAPR=9.5 dB: PAE=18.0%, RF P_{out}=31.8 dBm, NMSE=-40.4 dB) in top row; (20-MHz OFDM-like signal with PAPR=10.1 dB: PAE=17.0%, RF P_{out}=30.9 dBm, NMSE=-38.4 dB) in bottom row. 84

4.1 Block diagram of the DIDPA schematic with explicit labeling of the optimization variables (α, ϕ, $V_{GG}^{M,D}$, $V_{GG}^{M,F}$, $V_{GG}^{A,D}$, and $V_{GG}^{A,F}$), the main and auxiliary branch RF inputs (respectively, $\mathbf{u}_M$ and $\mathbf{u}_A$), and the RF output ($\mathbf{y}$). The block diagram highlights the two-stage DIDPA with the input and output matching networks of each stage, and the quarter-wave output combiner. 89

4.2 Layout of the simulated DIDPA MMIC with labeling of the main and auxiliary branch RF inputs (respectively, $\mathbf{u}_M$ and $\mathbf{u}_A$), and the RF output ($\mathbf{y}$). 90
4.3 (**a**) S-parameters and (**b**) CW large-signal characteristic of the DIDPA when the nominal bias and input splitting are applied. 90
4.4 Example of 2D sweeps cyclically realized by the coordinate descent optimization of PAE for the DIDPA under study versus (**a**) input splitter parameters (α, ϕ), (**b**) auxiliary amplifier bias voltages ($V_{GG}^{A,D}$, $V_{GG}^{A,F}$), and (**c**) main amplifier bias voltages ($V_{GG}^{M,D}$, $V_{GG}^{M,F}$). 96
4.5 Flow chart for the coordinate descent optimization algorithm for the case of descent order (α,ϕ) $\rightarrow$ ($V_{GG}^{A,D}$,$V_{GG}^{A,F}$) $\rightarrow$ ($V_{GG}^{M,D}$,$V_{GG}^{M,F}$). 97
4.6 Flow chart for single-objective Bayesian optimization. 101
4.7 Sampling of the six-dimensional variable space showing many possible trade-off points between RMS RF output power and PAE, highlighting the profile of non-dominated points (Pareto frontier). 103
4.8 Estimated optimal points (red circles) in a non-convex Pareto frontier with different FoM combinations with contour lines of the combined objective function for $\lambda = 0.5$. (**a**) Linear combination ($k = 1$), (**b**) non-linear combination ($k = 3$). The arrows indicate the combined minimization of the two scaled FoMs. 104
4.9 Estimated Pareto frontier between RMS RF output power and PAE obtained with a (**a**) linear combination ($k = 1$) and (**b**) non-linear combination ($k = 3$), while sweeping the combination factor λ. 104
4.10 Spectra of the output RF signal before (blue lines) and after linearization (red lines) with PA parameters at (**a**) nominal values, (**b**) after coordinate descent (iterated) optimization, and (**c**) after Bayesian optimization (P4). 106

4.11 PA gain and AM/PM characteristics before (blue lines) and after linearization (red lines) with PA parameters at (**a**) nominal values, (**b**) after coordinate descent (iterated) optimization, and (**c**) after Bayesian optimization (P4). 106
4.12 RF output spectrum before (blue lines) and after linearization (red lines) at optimal point P3. 108
4.13 PA gain and AM/PM characteristics before (blue lines) and after linearization (red lines) at optimal point P3. 108

5.1 (a) Measurement system block diagram and (b) picture. 115
5.2 Dual-input control block diagram. 117
5.3 Iterative behavior of the dual-input control while setting (a) a constant power splitting ratio and (b) a static shaping between a_1 and a_3. 118
5.4 fitting error in terms of NMSE among a_1, a_3 and their respective targets. The different markers highlight the case in which a constant relationship or a static shape is set between the two branches. 119
5.5 Simplified flow chart of the ILC-based algorithm for dual input control. 120
5.6 (a) dual-input tested device block diagram and (b) picture. . . 121
5.7 Logistic regression shaping function with its defining parameters. 121
5.8 ILC-DPD block diagram, which the k^{th} iteration of the ILD-DPD. 123
5.9 Relationship between the PAE of the DDPA and the output power distribution of the linearized DUT. 125
5.10 DIDPA waves before linearization. (a) Spectra of $\mathbf{b}_2$ and $\mathbf{a}_1$. (b) Spectrum of iterative error $\mathbf{a}_3 - \alpha_r e^{j\phi}\mathbf{a}_1$ across the ILC-based inner loop. 127
5.11 DIDPA waves after linearization. (a) Spectra of $\mathbf{b}_2$ and $\mathbf{a}_1$ spectra. (b) Spectrum of iterative error $\mathbf{a}_3 - \alpha_r e^{j\phi}\mathbf{a}_1$ across the ILC-based inner loop. 128

5.12 Iterative behavior of the NMSE between $\mathbf{a}_3^{(k,h)}$ and $\alpha_r e^{j\phi}\mathbf{a}_1^{(k,h)}$ for dual input emulation (inner loop) and PA linearization (outer loop, color coding in the legend). 128

5.13 PAE under modulated excitation for swept values of the input splitting conditions. (a) Without DIDPA linearization. (b) After DIDPA linearization. 129

5.14 Distorted and linearized (a) gain and (b) phase characteristics of the DUT in the optimal point obtained without considering the effect of DPD on PAE (**P1**). 131

5.15 Distorted and linearized (a) gain and (b) phase characteristics of the DUT in the optimal point obtained considering the effect of DPD on PAE (P_2). 132

5.16 Measured spectra of $\mathbf{b}_2$ at input splitting conditions **P1** and **P2** before (a) and after linearization (b). 133

5.17 Value of the objective function through the iteration of the 10D QSM-BO. 133

5.18 Static (a) gain and (b) efficiency characteristics of the optimized PA, while changing the number of tuning variables and optimization type. 134

5.19 Gain and phase characteristics of the before and after linearization (the blue and red lines, respectively) of the DDPA after (a-b) 2 QSM-BO, (c-d) 6 QSM-BO, (e-f) 10 QSM-BO. . 134

5.20 (a) PAE values while sweeping α and P_{AVS} of the 10D QSM-BO optimized PA, highlighting maximum PAE envelope. (b) Fitting using logistic function of the extracted shaping. 135

5.21 (a) Gain and (b) phase characteristics of the before and after linearization (the blue and red lines, respectively) of the max-PAE shaped DDPA. 136

5.22 Heat-maps representing the PAE-α-P_{out} relationship. (a) α-P_{out} static relationships for the maximum PAE shaping, constant α obtained for QSM-BO, and constant α obtained for maximum peak PAE. (b) α-P_{out} relationships set applying modulated input excitation (after DUT linearization) for the maximum PAE shaping, constant α obtained for QSM-BO, and constant α obtained for maximum peak PAE. 137
5.23 Spectra of the output RF signal after linearization at the optimal points found running the QSM-BOs. 138
5.24 Value of the objective function through the iteration of the 10D Dir-BO. 138
5.25 Gain and phase characteristics of the before and after linearization (the blue and red lines, respectively) of the DDPA after (a-b) 2D Dir-BO, (c-d) 6D Dir-BO, (e-f) 10D Dir-BO. . . 139
5.26 (a) Gain and (b) phase characteristics of the before and after linearization (the blue and red lines, respectively) of 10D Dir-BO optimized DDPA with input shaping. 139
5.27 Comparison between the Maximum PAE input shaping obtained for the QSM-BO optimized DDPA and the shaping obtained for the Dir-BO optimized PA 140
5.28 Spectra of the output RF signal after linearization at the optimal points found running the Dir-BOs. 140

List of Tables

2.1 Number of total complex multiplication needed during the real-time DPD coefficients update. Where $P_{PA} = P_{DPD} = 184$ and $N_F = 5$. $N_{PAs} = 4$ is the number of PAs in the beam-forming array. $N_s = 10^5$ is number of samples in the tested signal. $P_{BA} = 14$ is the equivalent number of complex-valued multiplications that are required in the 2D cubic interpolation of the real and imaginary part of the function $\boldsymbol{\omega}(\theta, \rho)$. K is not provided since there is no analogous value in the method proposed in the manuscript that can be adapted. 48

3.1 Operating points for a 10-MHz OFDM-like RF input (Figs. 3.9, 3.10, 3.12). 75

3.2 Operating points for a 20-MHz OFDM-like RF input (Fig. 3.11). 75

4.1 Nominal values of the parameters considered for DIDPA optimization. 91

4.2 Resolutions of the variables employed in the 2D factorial sweeps. 95

4.3 Comparison among optimum DIDPA performance obtained by applying the coordinate descent algorithm to the QSM for PAE maximization. All optimized performances involve the ILC-based analytical linearization of the QSM during the optimization. 98

4.4 Comparison among nominal and optimum DIDPA performance obtained by applying the various single-objective optimization algorithms to the QSM for PAE maximization. All optimized performances involve the ILC-based analytical linearization of the QSM during the optimization. 98
4.5 Comparison of PA performances obtained by means of PDF-based SuMo simulation at the optimal points. 105
4.6 Comparison of PA performances obtained by means of envelope simulation with modulated signals at the optimal points found running the coordinate descent or Bayesian optimizations on the PDF-based SuMo. 107
4.7 Nominal values of the parameters considered for DIDPA optimization. 107

5.1 Range of the DUT tuning variables. 122
5.2 DIDPA performance under modulated excitation at different input splitting conditions. 130
5.3 Comparison between the quasi-static pdf-based estimation for the PAE of the optimized PA targeting maximum peak PAE and targeting the quasi-static pdf-based PAE. 130
5.4 Optimized PA efficiency, power and linearity FoMs evaluated using WB modulated measurements after DPD at the optimal points found running the QSM-BOs and CW-BO. 131
5.5 Optimized PA efficiency, power and linearity FoMs evaluated using WB modulated measurements after DPD at the optimal points found running the Dir-BOs. 136
5.6 Comparison among the shaped-power-splitter-related tuning variables obtained in Sec. 5.6.2 and those obtained using Dir-BO. 138
5.7 Values of the tuning variables for DIDPA optimization. 141

Chapter 1

Introduction

1.1 Overview

To fulfill stringent linearity and power added efficiency (PAE) requirements, radio-frequency (RF) transmitters and power amplifiers (PAs) are evolving into complex systems with multiple-inputs (MIs). PA arrays, for instance, inherently incorporate MIs for beam steering capabilities. Various designs such as dual-input Doherty [4], outphasing [5], and load-modulated balanced amplifiers [6] employ an additional modulated input to induce predefined load-pull between two amplifier branches, enhancing PAE. Supply modulation in ET and polar PAs involves an additional input at the baseband terminal [7].

As PA complexity rises and high linearity is needed across broader modulation bandwidths (BWs), digital predistortion (DPD) is a critical necessity for efficient RF PAs. In load-modulated PAs or ET PAs, where supply is modulated based on a predetermined shaping table (ST) function of the RF envelope, MIs are derived from the single signal to be amplified. Consequently, these PAs could still be treated globally as single-input single-output (SISO) systems, relying on classical SISO DPD techniques. However, this limits PA operation to choices made during the design stage, relying on simulation models. Despite recent advances in wideband device character-

ization [8, 9], broadband operation and concurrent supply/load modulation may introduce spurious critical distortions that are challenging to predict at the design stage or compensate for with SISO DPD after implementation.

Considering a multiple-input single-output (MISO) PA description would provide additional degrees of freedom to extract maximum performance from a designed PA. As MIs are typically generated digitally, minimal changes in the transmitter configuration are necessary, but more intricate MISO behavioral models and alternative DPD strategies must be considered. Multiple-input multiple-output (MIMO) Volterra-based behavioral models considering mutual nonlinear effects among inputs [10–12] have been explored for PA arrays [13, 14], load-modulated [15, 16], supply-modulated [3, 17–19] PAs, and concurrent multi-band PAs [20]. For instance, the work in [3] implements a two-step method for dynamic load modulation, with the first step involving offline identification based on a static control function derived heuristically from continuous-wave (CW) characterization of the PA. However, this method may not guarantee optimal joint control of the two inputs in real-world applications with modulated signals and spurious mutual dynamics. The second step involves DPD using an inverse model explicitly considering the time-varying load control voltage fixed from the previous step. Architecturally, the predistorted signal is obtained using a classical coefficient learning routine, resembling typical DPD where only linearity improvement is targeted.

In practice, a well-defined PA inverse function with dynamics is only established for the symmetrical $N \times N$ case (equal inputs and outputs) [21]. Although the outputs of each single PA can still be obtained in PA arrays [22], other mentioned PA architectures inherently present similar problems to a MISO systems case. Considering an asymmetric architecture $M \times N$ with N (inputs) $> M$ (outputs), the non-injective relationship between inputs and outputs suggests some degree of overfitting as different input configurations might yield the same linearized output.

1.2 Power Amplifiers Metrics

1.2.1 Modulated Signal Characteristics

The use of multitone signals in PA testing could be considered as an enhancement of the classical two-tone analysis. The main feature of multitone signals is the possibility to better approximate the frequency content of modern communication signals. [23] Consequently, multitone signals are typically used in measurement labs to provide a periodic, well characterized waveform that can simulate complex modulated RF signals. The already mentioned two-tone test signal is typically employed to illustrate many FoMs which represents linearity of RF circuits. [24] Such as intermodulation distortion (the unwanted generation of signals close to the multitone band caused by mixing products from the harmonic products from all frequency orders), cross-modulation (the transfer of the modulating part from one modulated signal to another, with a different carrier frequency) [25], memory effects, and gain compression/expansion. Unfortunately, because of modern communication standard requirements (i.e. high data rates and high spectral efficiency), signals can present large bandwidth in relation to the carrier and high peak to average power ratio (PAPR). That makes these signals impossible to correctly represent by two-tone test signals. A multitone excitation is defined by the number of tones it contains, their spacing and the total bandwidth of the excitation signal, in addition to the magnitude and the relative phases of the tones. Thus, the multitone signal can be defined as follows:

$$x(t) = \sum_{k=1}^{N} A_k cos(\omega_k t + \theta_k), \tag{1.1}$$

where A_k is the amplitude and θ_k is the phase of the k^{th} sine function, N is the number of sinusoids, and $\omega_k = \omega_0 + (k-1)\delta\omega$, with ω_0 being the frequency of the first tone and $\delta\omega$ the constant frequency separation between them. It is possible to obtain different shapes of the time domain envelope by changing the relative phases between the multitone frequency components. Therefore, multitones can be used to emulate communication standards by

varying the relative phases in order to fit the desired probability density function (PSD) [26].

Since the signal it is necessary to emulate has a defined bandwidth f_{bw} and time duration T, the selection of the two first parameters is straightforward. Having defined the bandwidth of the multitone excitation with f_{bw}, the number of tones can be derived such that the multitone excitation has enough resolution in time domain to correctly represent the emulated complex envelope, using the formula:

$$N_{Tones} = f_{bw} * T. \tag{1.2}$$

Alternatively, a desired tone spacing can be defined and then the required number of tones calculated. One straightforward approach to obtain the relative magnitudes and phases of the tones is to consider a Fourier series representation of a particular time realization of a communication signal [26]. In practice, a discrite Fourier transform is used to obtain Fourier series coefficients of a complex discrete-time signal of finite time duration:

$$x(n) = \frac{1}{N}\sum_{k=1}^{N} X(k)e^{\frac{j2\pi kn}{N}} = \sum_{k=1}^{N} A_k e^{j\left(\frac{2\pi kn}{N}+\theta_k\right)} \tag{1.3}$$

where A_k and θ_k are the as in Eq. 1.1.

There are many reasons why multitone signals are prefered instead of actual modulated signals for device testing and modeling. First of all, with these signals it is possible to emulate the statistical characteristics of the modulated signals through the use of the relative phases of the tones. Therefore it is possible to perform an analysis that is not related to any particular standard, emulating a class of modulated signals characterized by a PDF. This is possible selecting a set of A_k and θ_k with an iterative procedure, which aims to minimize the difference between the synthesized PDF and the desired one [23]. In addition, multitone signals are periodic, so they are straightforward to generate and measure by using many instruments commonly used to characterize bandpass modulated signals, such as vector signal generators, spectrum analysers, and vector network analyzers (VNAs). It is

therefore possible to use the measuring instrumentation that cannot directly manage the modulated signals (e.g. large signal analyser) or that needs a periodical versions of the modulated signals in order to perform broadband measurements (e.g. a VNA).

1.2.2 Linearity Metrics

After the definition of the excitation signal used in this work to test RF devices, it is now possible to define some multitone FoMs which are used to evaluate linearity performance of the device under test (DUT). The first figure of merit presented is the adjacent channel power ratio (ACPR), which is a measure of the spectral regrowth caused by devices' non-linearities. This quantity is defined as the ratio between the power generated in the side bands, i.e. the adjacent channels, due to spectral regrowth and the in-band average output power:

$$ACPR = \frac{P_S}{P_{out}} = \frac{\int_{\Delta\omega_S} S(\omega)d\omega}{\int_{\Delta\omega_C} S(\omega)d\omega}, \tag{1.4}$$

where P_{out} denotes the total measured output power in the interval $\Delta\omega_C$, which represents the channel bandwidth, while P_S refer to the power in the adjacent channel, whose frequency ranges is $\Delta\omega_S$. $S(\omega)$ is the power spectral density (PSD) of the PA output signal. Furthermore, to better emulate the metrics for various standards, it is possible to define variants of the expression using different integration masks (for example by calculating only the power of one of the two side-bands).

Although ACPR is a widely used figure of merit in wireless standards, it is a metric for the out-of-band distortion and a poor metric to measure nonlinear distortion whose effects are visible in the main channel (the in-band distortion). For this purpose, when referring to modulated signals, the error vector magnitude (EVM) is typically used, which however needs a demodulation and measures the error between measured and expected symbols. Although multitones are not properly modulated signals, the EVM

can be measured as the ratio of the purely nonlinear distortion power (i.e., the output signal power minus the linearly related power to the input) to the input signal power [27] across the excitation bandwidth. Considering a generic model of a nonlinear amplifier:

$$\mathbf{y} = f(\mathbf{x}), \tag{1.5}$$

where $\mathbf{y}$ and $\mathbf{x}$ are vector which represents the time-domain envelope signal measured at the amplifier output and input, while $f(\bullet)$ is the generic nonlinear relation between them; the EVM can be defined as:

$$\begin{aligned} E(\omega) &= S_y(\omega) - |G_{BLA}(\omega)|^2 S_x(\omega), \\ \mathrm{EVM} &= \sqrt{\frac{\int_{\Delta\omega_C} E(\omega) d\omega}{\int_{\Delta\omega_C} |G_{BLA}(\omega)|^2 S_x(\omega) d\omega}}, \\ \mathrm{EVM_{dB}} &= 20 \log_{10}(\mathrm{EVM}), \end{aligned} \tag{1.6}$$

where $S_y(\omega)$ is the PSD of the output signal $\mathbf{y}$, $S_x(\omega)$ is the PSD of the input signal $\mathbf{x}$, and G_{BLA} the approximation of a linear dynamic gain that mimics the operation of a typical radio receiver, where the equalizer estimates a frequency response function to compensate for the equivalent linear distortion of the channel and transmission chain [28].

A figure of metric analogous to EVM which can be used with this kind of signal is the normalized mean square error (NMSE), which measures the error between the measured and expected samples of a generic time waveform:

$$NMSE = \frac{\sum_n |\tilde{y}(n) - Gx(n)|^2}{\sum_n |\tilde{y}(n)|^2}; \tag{1.7}$$

where $\tilde{y}(n)$ and $x(n)$ are the n-th samples of $\tilde{\mathbf{y}}$ and $\mathbf{x}$, while G is the desired linear complex gain of the amplifier. The main advantage of the NMSE consists of having a time-domain measurement of the distortions introduced by the device, but it requires an envelope measurement. Without a direct measurement of the signal samples in the time domain, it is possible to extract the NMSE starting from the measurement of the amplitude and phase spectrum. The NMSE measures the total distortion introduced by the PA

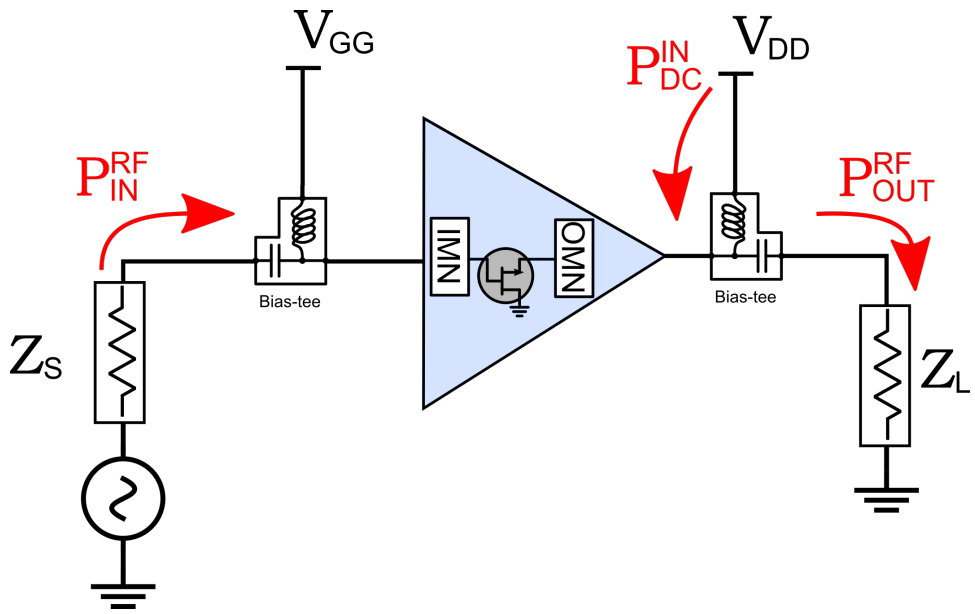

Figure 1.1: Generic single-transistor linear PA electrical scheme

comparing the output complex envelope with a linearly amplified version of the input

1.2.3 Power and Efficiency metrics

Denoting with P_{OUT}^{RF} the total RF power transferred to the load and with P_{IN}^{RF} the total power provided by the RF signal (Fig. 1.1), the PA must provide the following power gain:

$$G = \frac{P_{OUT}^{RF}}{P_{IN}^{RF}}. \tag{1.8}$$

With reference to Fig. 1.1 the power balance of a single transistor amplifier is defined as follows:

$$P_D = P_{IN}^{DC} + P_{IN}^{RF} - P_{OUT}^{RF}, \tag{1.9}$$

where P_{IN}^{DC} represents the overall power provided by the PSU. The efficiency metrics mainly used are two:

- Drain Efficiency: the standard efficiency Figure-of-Merit (FoM) which measures the ratio between the average RF power transferred to the load P_{out} and the average power drawn from the power supply P_{DC}.

$$\eta = \frac{P_{OUT}^{RF}}{P_{IN}^{DC}}. \tag{1.10}$$

- Power Added Efficiency (PAE): this metric takes into account the RF power provided from input signal of the amplifier (P_{IN}^{RF}). This is particularly important when the amplifier shows such a low power gain that the power needed to drive the input is not negligible, and should be considered in the power balance. The PAE can therefore be defined as:

$$PAE = \frac{P_{OUT}^{RF} - P_{IN}^{RF}}{P_{IN}^{DC}}. \tag{1.11}$$

1.3 Digital Predistortion

1.3.1 Behavioral Modeling

The characterization of a device through behavioral modeling can be understood by dividing it into some simpler steps.

- The choice of two observables which is considered as the input and the output of the system and whose mathematical relation must be approximated. For instance, in the case of RF PAs, the lowpass equivalent of the modulated signal at the input and output sections of the circuit.

- The choice of a mathematical expression that can approximate the transfer function between the input and output, always considering the inevitable compromise between computational complexity and the capability of the function to map all the possible effects of non-idealities of the PA (i.e. nonlinearities, memory effects). The function can be implemented as a linear-in-the-parameters expression, in order to simplify coefficient fitting.

- The choice of a model identification procedure and validation methodology, which measures the model fitting. The aim of the identification algorithm is to find the optimal point, in terms of a set of coefficients of the model, which minimizes the fitting error of the behavioral model.

In practice, for PAs, the observables are the low-pass complex envelope of the RF signals. Band-pass signals can be converted into their low-pass equivalents through a down-conversion operation and vice versa through an up-conversion operation. Therefore considering a generic modulated signal:

$$\widetilde{x}(t) = I(t)\cos(\omega_c t) - Q(t)\sin(\omega_c t), \tag{1.12}$$

where $I(t)$ and $Q(t)$ denote the in-phase and quadrature components. So, it is possible to use the phasor representation:

$$\widetilde{x}(t) = Re[(I(t) + jQ(t))e^{j\omega_c t}] = Re[x(t)e^{j\omega_c t}], \tag{1.13}$$

where $x(t)$ is called low-pass equivalent signal or complex envelope and owns the same information content as the band-pass signal $\tilde{x}(t)$.

Then, the behavioral approach can be mathematically modeled the power amplifier as a time-invariant and discrete-time nonlinear filter which maps an input function x to an output function y, where x and y represent the whole complex envelopes of the RF signal measured respectively at the input and output sections of the PA. Obviously dealing with the measurement of signals' time samples and having already specified that we desire to elaborate a discrete time model of the device, the x and y functions represent discrete time signals, measured as complex vectors. Finally, the time samples $x(n)$, $y(n)$ are the complex symbols of the input and output low-pass equivalent, as stated in Eq. 1.14, where the transfer from the continous-time to the discrete-time representation is explained:

$$x(n) = x(nT), \tag{1.14}$$

where T is the sampling time.

Volterra Model

The choice of the mathematical model of the PA is subject to some physical considerations on the device. Under the conditions of operator causality, stability, continuity, and fading memory, the PA is modeled through the following function [29]:

$$y(n) = f_D[x(n), x(n-1), ..., x(n-Q)], \tag{1.15}$$

where Q is the amplifier memory span and f_D is a multidimensional nonlinear function of its arguments. There are various ways to approximate this function and obtain a representation that can be suitably fitted in order to imitate the behavior of a particular device. For instance it is possible to use look-up-table-based models, artificial neural networks or polynomials [29]. The latter type of approximation is the most used in the DPD field and it will be used to implement the predistorter in this thesis.

If f_D is approximated by a polynomial obtained with a multidimensional Taylor series development, then a structure similar to a nonlinear FIR filter known as a Volterra series or a Volterra filter is obtained. The Volterra model is the most comprehensive model for nonlinear dynamic systems. Thus, with this approximation the function f_D is developed in series and represented in this form:

$$y(n) = \sum_{m_1=0}^{M-1} \sum_{m_2=m_1}^{M-1} ... \sum_{m_K=m_{K-1}}^{M-1} h(m_1, m_2, ...m_K) \prod_{k=1}^{K} x(n-m_k), \tag{1.16}$$

where $h(m_1, m_2, ...m_K)$ is the function that identifies the parameters of the Volterra series expansion (also called the discrete-time Volterra kernels), K is the model nonlinearity order and M is the memory depth. The set of coefficients h are the already mentioned parameters that will be identified in order to fit the behavior of the DUT. The number of parameters in the conventional Volterra series increases exponentially with the of order of non-linearity and the memory depth. Increasing the size of the optimization problem by incrementing the number of coefficient soon leads to an unsustainable computational complexity. This affects both the coefficient identification problem

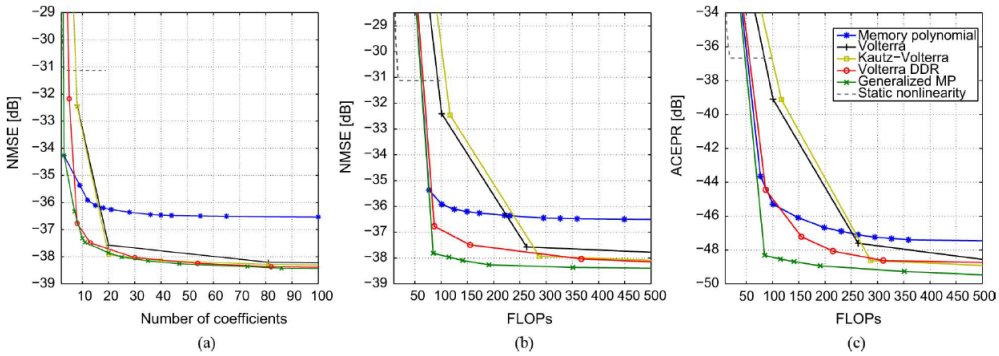

Figure 1.2: Class AB PA with high-level gain compression. (a) NMSE vs number of parameters of the model, (b) NMSE vs computational complexity measured in number of floating point operations per seconds (FLOPs), (c) adjacent channel error power ratio (ACPER) vs FLOPs [1].

(increasing the load for the optimization method) and the actual implementation and calculation of the function (for example in terms of the number of sums and products). Therefore the practical use of the Volterra series is limited. To reduce this computational complexity, various techniques have been proposed to simplify the Volterra model. These Volterra-based models can be managed with dynamic deviation reduction techniques or through a systematic pruning of the coefficients, obtaining for instance a memory polynomial (MP) model, a generalized memory polynomial (GMP) model or a Kautz-Volterra model [1] [30] [31]. The aim of these procedures is to select a subset of the Volterra coefficients, ideally keeping those that have greater influence in the approximation of the device.

Memory Polynomial Model

The MP model represents a very compact version of the Volterra series and is widely used in behavioral modeling and in the predistortion of PAs with memory effects. If we represent the possible approximate models for a PA in a graph that relates its computational complexity to its performance, in terms of adherence to the real behavior of the device (measured with the

NMSE between the PA and model output), as in Fig. 1.2a. It is clear that the MP has low complexity with limited performance, while the Volterra series is much more complex with a consequently better approximation of the behavior of the device. The MP model is obtained through the pruning of the Volterra series, removing all the coefficients that take into account the cross-terms, i.e. all those monomials that correspond to products between values referring to different time instants. So the MP model results in the following description:

$$y(n) = \sum_{m=0}^{M-1} \sum_{k=1}^{K} a_{m,k} x(n-m)|x(n-m)|^{k-1}, \tag{1.17}$$

where K and M are the nonlinearity order and the memory depth of the DUT, respectively, and $a_{m,k}$ are the model coefficients.

It is important to note that all polynomial models are linear functions with respect to their coefficients, often allowing the adoption of straightforward optimization algorithms to identify them. Therefore, the MP model, but more generally all the models based on a polynomial expansion of f_D, can be visualized with a practical vectorial representation:

$$\mathbf{y} = \mathbf{H}\mathbf{a}, \tag{1.18}$$

$$\mathbf{y} = [y(0), y(T), \ldots, y(nT), \ldots, y((N-1)T)]^t, \tag{1.19}$$

$$\mathbf{a} = [a_{0,1}, \ldots, a_{0,K}, \ldots, a_{M-1,1}, \ldots, a_{M-1,K}]^t, \tag{1.20}$$

where $\mathbf{y}$ is the time samples vector of the complex envelope sampled with a period T at the model output (Eq. 1.19), $\mathbf{a}$ is a vector that contains the coefficients of the model, which in the case of the memory polynomial is obtained with the expression 1.20. Finally, $\mathbf{H}$ is a matrix built starting from the complex baseband input signal of the system, in accordance with the model basis function set. This matrix, which will be addressed as regression matrix, can in the case of memory polynomial and a generic input of the

model x be represented with the expression:

$$\mathbf{H} = \begin{pmatrix} x(0) & \dots & x(0)|x(0)|^{(K-1)} & \dots & 0 & \dots & 0 \\ \vdots & \ddots & \vdots & \ddots & \vdots & \ddots & \vdots \\ x(n) & \dots & x(n)|x(n)|^{(K-1)} & \dots & x(n-(M-1)) & \dots & x(n-(M-1))|x(n-(M-1))|^{(K-1)} \\ \vdots & \ddots & \vdots & \ddots & \vdots & \ddots & \vdots \\ x(N) & \dots & x(N)|x(N)|^{(K-1)} & \dots & x(N-(M-1)) & \dots & x(N-(M-1))|x(N-(M-1))|^{(K-1)} \end{pmatrix}. \tag{1.21}$$

It is important to highlight that the formulation of the Eq. 1.19 (unlike the Eqs. 1.17, 1.20, 1.21) is valid for any polynomial model, regardless of the adopted pruning.

1.3.2 DPD Model Identification

The target is to design an appropriate predistorter that is able to compensate for non-idealities and ensure a more linear amplification of the signal to be transmitted. All the mathematical considerations expressed in the previous paragraphs remain valid to explain the fundamental concepts of the design of a predistorter. By presenting the definitions of the signals considered and the models adopted by behavioral modeling, the next paragraphs will focus on the identification process of the models as they occur in the DPD. Conceptually, the DPD consists in implementing a block upstream of the PA as in Fig. 1.3.

The block must preprocess the input signal to the DUT using a nonlinear function complementary to the one of the PA, so that the cascade of the predistorter and the PA operates as a linear amplification system. Fig. 1.3 also shows the AM/AM and AM/PM characteristics of the various cascade blocks in order to better understand the concept of complementarity between predistorter and PA, in fact, the target is to have a constant gain over the whole operating range of the Linearized Power Amplifier (LPA). The figure clearly shows how the predistorter is designed to generate a gain expansion that compensates for the gain compression commonly observed in PAs. It is important to note that, in this case, the maximum input power of the predistorter, and consequently also of the LPA, is lower than that of the nonlinerized PA. This maximum input power of the LPA is determined by the

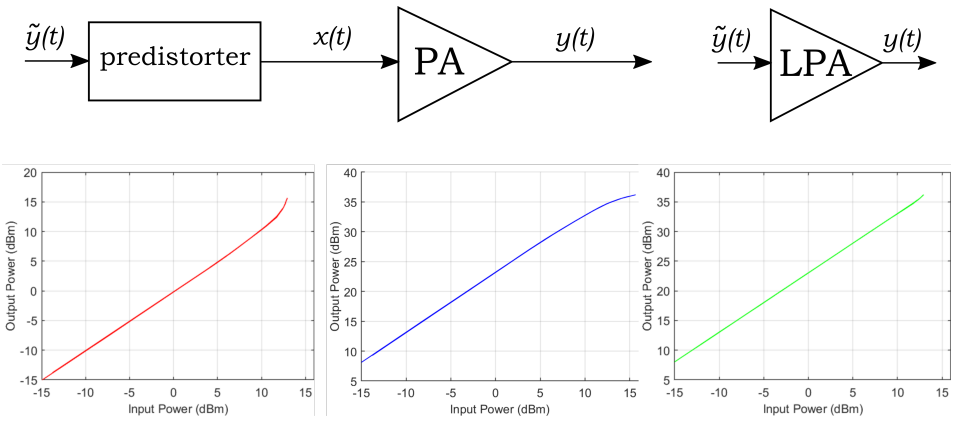

Figure 1.3: AM/AM characteristics of each block of the predistorter-PA chain.

maximum linear output power chosen for the LPA. This fundamental aspect will be discussed several times later in the selection of the normalization gain for the DPD. Considering a nonlinear device, the relationship between the instantaneous power input to the predistorter $P_{in,PD}$ and the output of the PA $P_{out,PA}$ expressed in dBm is:

$$P_{in,PD}(n) = P_{out,PA}(n) - |G_{LPA}|_{dB} \tag{1.22}$$

where G_{LPA} is the desired complex gain of the LPA. Then, taking into account that the relationship between the input and output power of the PA is given by the instantaneous gain of the device $G_{PA}(n)$:

$$P_{in,PA}(n) = P_{out,PA}(n) - |G_{PA}(n)|_{dB} \tag{1.23}$$

In this way, it is possible to define the desired instantaneous gain of the predistorter $G_{PD}(n)$:

$$|G_{PD}(n)|_{dB} = P_{in,PA}(n) - P_{in,PD}(n) = |G_{LPA}|_{dB} - |G_{PA}(n)|_{dB}. \tag{1.24}$$

The desired phase shift of the predistorter $\Phi_{PD}(n)$ is defined analogously:

$$\Phi_{PD}(n) = \Phi_{LPA} - \Phi_{PA}(n) \tag{1.25}$$

where Φ_{PA} and Φ_{LPA} are the phase shift introduced by the power of the PA and linearized PA. These relations show how, for a given signal, by knowing the AM/AM and AM/PM characteristics of the amplifier, it is possible to directly obtain the AM/AM and AM/PM characteristics of the predistorter. The ability of the DPD system to compensate the distortions introduced by the PA depends on the match between the characteristic of the predistorter and the DUT to be linearized. Since the nonlinearities of the DUT may vary with the drive signal over time, due to various dynamic and time-varying effects that can be generically defined as memory effects, it would be essential to continuously update the predistortion function to keep the system composed of the DUT and the predistorter linear. A memory-less predistorter is not practicable, due to the latency of a feedback capable of constantly updating the model coefficients. Consequently, it is necessary to implement and identify predistorters with more complex models (like the one described in Subsection 1.3.1), by including nonlinear dynamic effects, that allows for broader prediction capabilities. The identification of these types of predistorters typically follows a direct or an indirect learning architecture.

1.3.3 Indirect Learning

In the topologies shown in Fig. 1.4, the input and output signals to the PA are used to calculate the coefficients of the predistorter model. Also, in the same Fig. 1.4 it is shown how this possible implementation of DPD can be achieved in two alternative ways. In the first architecture, the direct behavioral model of the PA is identified and subsequently inverted analytically or numerically, then the predistorter coefficient update will be performed. The post inversion of the model is problematic as its complexity increases, i.e. its ability to correctly approximate strongly nonlinear devices or with the presence of marked memory effects.

In the second variant of indirect method the predistorter is identified simply by copying the model of the post inverse of the PA. This method is based on the assumption that the post-inverse is identical to the pre-inverse

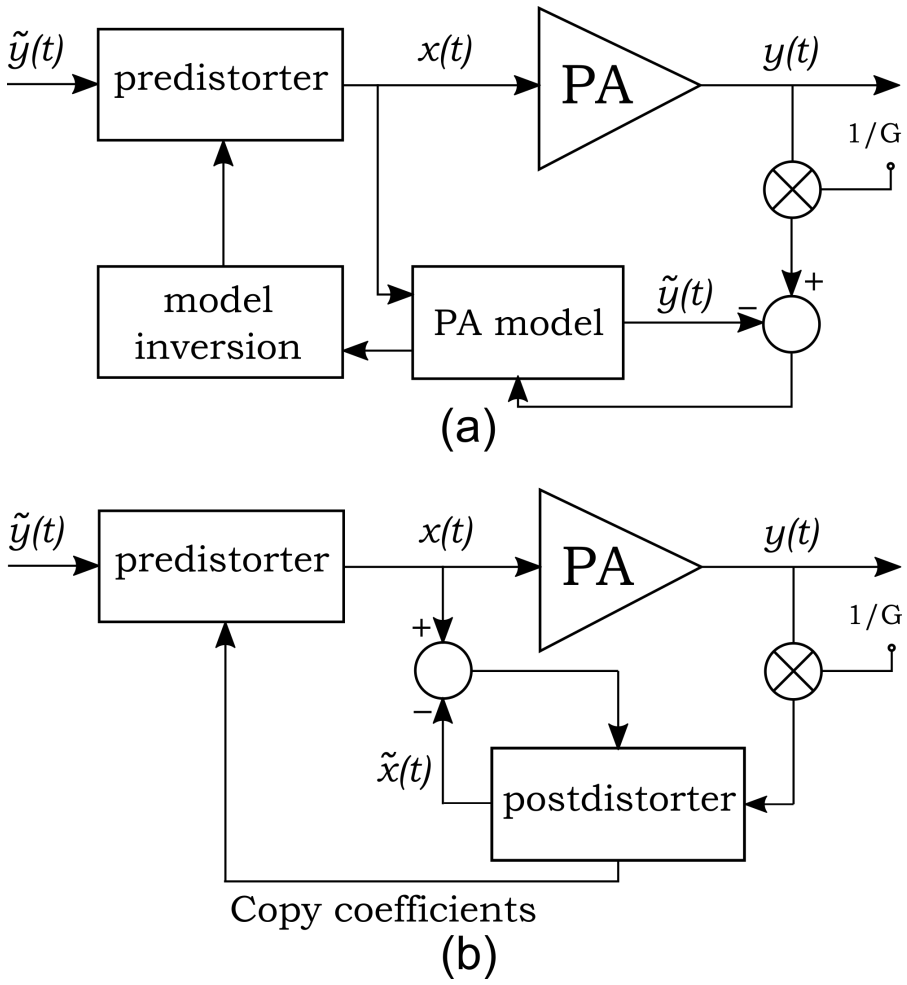

Figure 1.4: Indirect learning Architecture implemented realized through the (a) analytical model inversion and the (b) postdistorter identification

this version is properly called Indirect Learning Architecture (ILA). In order to identify the postdistorter model, the most commonly used method is the least square (LSQ) identification. Once the fixed linearization gain G and the input excitation $\widetilde{y}(t)$ used for the identification phase have been defined, it is possible to measure the distorted output $y(t)$ of the PA, as depicted in Fig. 1.4b. The LSQ method aims to minimize the difference between the postdistorter output $\widetilde{x}(t)$ and the PA input $x(t)$. After the measurement of the output of the PA, it is possible to define the regression matrix H of

a generic postdistorter, obtained from $y(t)$ samples divided by the desired linear gain G, similarly to Eq. 1.18:

$$\widetilde{\mathbf{x}} = \mathbf{H}\mathbf{a} \tag{1.26}$$

Hence, the postdistorter set of coefficient a, therefore also the predistorter model, by minimizing the squared error between $\widetilde{\mathbf{x}}$ and $\mathbf{x}$:

$$\min_{\mathbf{a}} \|\widetilde{\mathbf{x}} - \mathbf{x}\| \implies \mathbf{H}^{+}\widetilde{\mathbf{x}} = (\mathbf{H}\mathbf{H}^{+})^{-1}\mathbf{a} \tag{1.27}$$

using the Moore-Penrose inverse:

$$\mathbf{a} = \mathbf{H}^{\dagger}\widetilde{\mathbf{x}} = (\mathbf{H}\mathbf{H}^{+})^{-1}\mathbf{H}^{+}\widetilde{\mathbf{x}} \tag{1.28}$$

After the identification phase, it comes a verification phase in which the $\widetilde{y}$ is used as input excitation of the linearized PA to verify the linearization procedure. The linearization gain G can be chosen selecting a desired output peak power (e.g. at 1-dB compression point) and following one of this two different approach: the constant output average power technique or the constant output peak power technique. In the first approach G is chosen in order to preserve the average output power between the identification and the verification phases, while the second method aims to preserve the peak output power.

1.3.4 Direct Learning

In the direct learning architecture (DLA), the predistorter is directly identified from the PA stimulus-response pairs. Since the PA is a complex system featuring nonlinear dynamic effects, the direct identification of the pre-inverse is not trivial. One way to directly identify the model is by using iterative nonlinear optimization algorithms. Thus, the model identification can be performed iteratively by adding feedback to the system which includes the predistorter in the updating loop, as in Fig. 1.5. The closed loop exploits concepts derived from control theory, trying to directly minimize the error

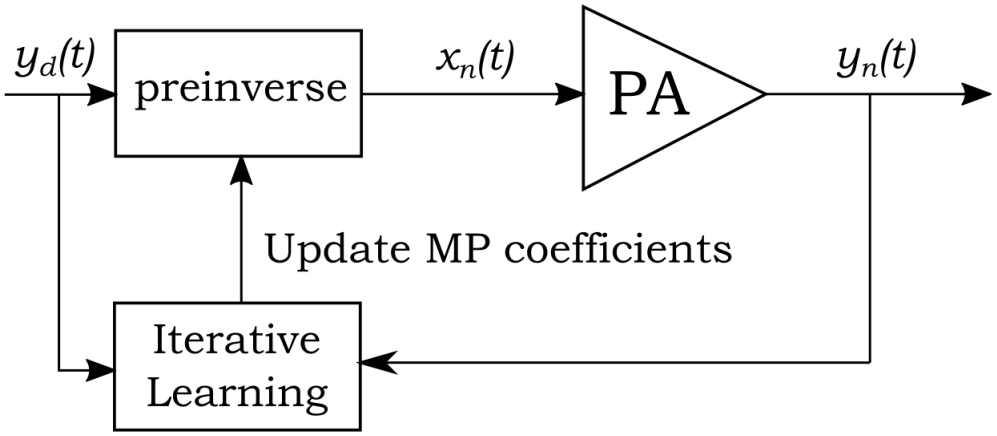

Figure 1.5: Direct Learning Architecture

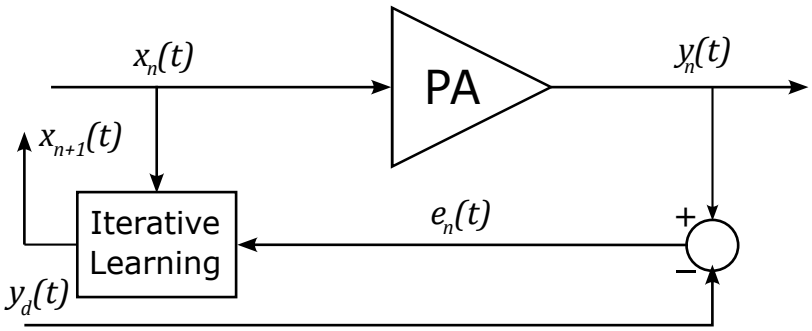

Figure 1.6: Iterative learning control architecture.

and tracking between the measured output y, suitably normalized with the desired linear gain, and the input of the predistorted system y_d.

The direct learning consists of updating the coefficients that directly uses the input and output of the linearized system. Closed loop direct learning systems show some problems especially with regards to slow convergence and high computational complexity given the absence of a regular relationship between the coefficients and the linearity error. Added to this is the possibility of divergence of the algorithm due to the closed loop. In addition, the convergence issues must be handled.

Iterative Learning Control

A typical implementation of the direct learning DPD architecture is represented by the well know iterative learning control (ILC) [32]. With reference to Fig.1.6, it is possible to define a vector representation for sampling of the signals (as adopted in the previous Sections):

$$\begin{aligned} \mathbf{x} &= [x(0), x(T), \ldots, x(kT), \ldots, x((K-1)T)]^t, \\ \mathbf{y} &= [y(0), y(T), \ldots, y(kT), \ldots, y((K-1)T)]^t, \\ \mathbf{e} &= [e(0), e(T), \ldots, e(kT), \ldots, e((K-1)T)]^t, \\ \mathbf{y}_d &= [y_d(0), y_d(T), \ldots, y_d(kT), \ldots, y_d((K-1)T)]^t. \end{aligned} \tag{1.29}$$

The linearization problem could be generalized as

$$\begin{aligned} f : \mathbb{R}^K \rightarrow \mathbb{R}^K, \mathbf{x} \rightarrow \mathbf{y}, \\ \mathbf{e} = \mathbf{y} - \mathbf{y}_t = f(\mathbf{x}) - \mathbf{y}_t = \mathbf{0}_V, \end{aligned} \tag{1.30}$$

Since the non-linear system $f(\mathbf{x}) - \mathbf{y}_t = \mathbf{0}_V$ has the same number of variables and equations, it can e solved using the well-known Newton iterative method:

$$\mathbf{x}_{n+1} = \mathbf{x}_n - \mathbf{J}^{-1}\mathbf{e}_n, \tag{1.31}$$

where $\mathbf{J}$ is the Jacobian matrix of f, and $\mathbf{x}_n$ is the predistorted signal at the n^{th} iteration.

$$\mathbf{x}_{n+1} = \mathbf{x}_n - \mathbf{\Gamma}\mathbf{e}_n, \quad \mathbf{\Gamma} = \begin{pmatrix} \Gamma(0) & \ldots & 0 & \ldots & 0 \\ \vdots & \ddots & \vdots & & \vdots \\ 0 & \ldots & \Gamma(k) & \ldots & 0 \\ \vdots & & \vdots & \ddots & \vdots \\ 0 & \ldots & 0 & \ldots & \Gamma(K-1) \end{pmatrix}. \tag{1.32}$$

in general, the higher the values of the learning gain $\Gamma(k)$ are, the faster is the ILC convergence, with the drawback of a higher risk of instability of the iterative loop. The convergence of the ILC has been demonstrated

if $\Gamma(k) < \frac{2}{\mathbf{J}_{k,k}}$. Considering a quasi-memoryless PA, the relationship can be simplified as $\mathbf{J}_{k,k} < \frac{\mathbf{y}(kT)}{\mathbf{x}(kT)}$. Therefore, a good guess (which maintains convergence) is represented by the instantaneous gain:

$$\Gamma(k) = \frac{\mathbf{x}(kT)}{\mathbf{y}(kT)}. \tag{1.33}$$

When convergence is reached, $\mathbf{x}_n$ represents the predistorted signal.

The ILC procedure described above can be considered a non-parametric DPD approach, since the predistorted signal $\mathbf{x}_n$ is obtained without defining any model for the predistorter. The principal drawback for this non-parametric approach is represented by the iterative procedure, which requires many acquisitions . The system that adopted this mechanism would require a long time to achieve the DPD, which requires an iteration loop for every bunch of data to be sent. This makes the non-parametric DPD based on the ILC not feasible for real-time operation.

In the context of direct learning architectures, the ILC could be used as part of a predistorter coefficient fitting algorithm [32]. Once the DPD model has been chosen and the regression matrix $\mathbf{H}$ for $\mathbf{y}_d$ has been calculated, it is possible to fit the predistorter parametric model by solving the problem described in Eqs. 1.26 1.27 1.28.

1.4 Device Parameters Optimization

1.4.1 Single-Objective Optimization Problem

In this work, the optimization approach follow a generic black-box approach:

$$\max_{\phi} f(\phi), \tag{1.34}$$

where f is a generic FoM (e.g. PAE, NMSE, ACPR, etc.) which is extracted by simulations or directly measured using modulated signals. ϕ is a vector representing the whole set o variables: DPD coefficients, voltage biases and circuit parameters when they are accessible. The following list describes

some characteristics aimed at assessing how suitable a method is for solving our problem:

- **Number of function evaluation** The objective function needs a not negligible time to be evaluated due to high computational cost for the simulation of the device and the time necessary to carry out a measurement. Consequently, the optimization method must try to minimize the number of function evaluations.

- **Dependency on the initial point** The performance of an optimization strictly depends on the choice of the initial point. In general, the convergence point could depend on the iteration starting point, since the objective function is unknown and non-convex. The task of the method is to reduce this dependency as much as possible, by aiming for a global solution.

- **Non-smooth optimization** During an iteration, the algorithm could push the device out of the safe-zone, i.e. it could try to evaluate the objective function at a point corresponding to excitations that are not allowed for a specific DUT (e.g. too much input power or a too high supply voltage). Hence, the assumption of classical differentiability is not realistic since for many points the objective function cannot be evaluated. Therefore, the method must be robust enough in order to overcome this problem.

- **Initial point** Due to the non-convex nature of f, the optimization could converge at different points depending on the choice of the initial guess point ϕ_0.

- **Stopping criteria** The achievement of a local minimum point can be measured in various ways, for example by directly evaluating the gradient at the point, or by measuring the convergence of the series of evaluations. Since the addressed optimization aims at finding a global maximum/minimum point, the definition of a stopping criteria that

defines the achievement of the objective of the problem is not trivial. Indeed, there is no way to define a precise metric that measures the degree of global optimality of a point of a non-convex function.

1.4.2 Gradient-Based Algorithm

The gradient-based methods are a class of optimization algorithm that leverage on local information about the unknown function f. They leverage the gradient information to guide the optimization process efficiently. In many cases, gradient-based optimization methods guarantee convergence to a local minimum of the objective function. This property ensures that the optimization process reaches a stable solution, at least in the vicinity of the starting point. Gradient-based methods are susceptible to getting stuck in local minima, especially in high-dimensional spaces. This can compromise the ability to find the global minimum of the objective function. The major drawback of the class of algorithms is the derivatives extraction: computing gradients can be computationally expensive, especially when dealing with large datasets or complex models. This can slow down the optimization process. The convergence of gradient-based methods can be highly dependent on the initial values of the model parameters. Poor initial conditions may lead to convergence to suboptimal solutions or slow convergence.

1.4.3 Derivative-Free Algorithm

Derivative-free optimization algorithms are optimization methods that do not rely on the computation of gradients or derivatives of the objective function. Derivative-free optimization is well-suited for optimizing functions that are nonsmooth, discontinuous, or have complex and irregular behavior. Traditional gradient-based methods may struggle in such cases. These methods are often less sensitive to the choice of initial conditions compared to gradient-based methods. This can be advantageous when dealing with poorly conditioned or ill-posed optimization problems. Derivative-free algo-

rithms can be effective for global optimization, as they do not rely on local gradient information that might lead them to converge to local minima. They are often capable of exploring a broader solution space. Derivative-free optimization methods typically require more function evaluations compared to gradient-based methods for achieving convergence. This can result in slower convergence rates, especially for high-dimensional problems. Compared to some gradient-based methods, derivative-free optimization algorithms may have limited theoretical guarantees regarding convergence rates or optimality. Derivative-free methods often treat the objective function as a black box, making it challenging to incorporate problem-specific knowledge or constraints into the optimization process.

1.4.4 Multi-Objective Optimization Problem

When dealing with multiple FoMs is not possible to identify a single value for ϕ that can be considered as global optimum. This introduces the concept of Pareto front. In a multi-objective optimization (MOO), the Pareto front is the set of points whose related value of the objective functions can not be improved in value without degrading some of the other objective values.

FoMs Combination

Rather than performing an unfeasible high amount of function evaluations, an efficient way to identify the Pareto frontier consists of combining the FoMs to be optimized in a single scalar objective function $g(\mathbf{x})$ and thus adopt a single-objective optimization algorithm. Considering the case of a MOO that considers two FoMs, a polynomial combination among two different FoMs is considered:

$$g(\phi) = \lambda f_1(\phi)^k + (1-\lambda) f_2(\phi)^k; \qquad \text{with } \lambda \in [0,1]; \tag{1.35}$$

where k is the polynomial order, λ is the combination parameter, while $f_1(\mathbf{x})$ and $f_2(\mathbf{x})$ are normalized scalar FoMs. The Pareto front exploration is performed sweeping λ. The selection of the polynomial order k strictly depends

on the expected shape for the Pareto front. The effect of the selection of k in the Pareto extraction is analyzed in Sec. 4.4.

Constrained Optimization

The proposed procedure aims at identifying an optimal set of ϕ so that one or more functions of those coefficients, i.e., one or more scalar FoMs, are either maximized (equivalently, minimized) or constitute a constraint. In this way the MOO can be seen as a constrained optimization, in which the solutions obtained by varying the constraint represent the Pareto front among the optimized functions. Let us consider $f(\phi)$ as corresponding to a particular FoM to be maximized, and $g(\phi)$ as the one on which the constraint is imposed. The following optimization problem must be solved:

$$\max_{\phi} f(\phi) \quad \text{subject to} \quad g(\phi) < \eta, \tag{1.36}$$

where η is a scalar quantity and depends on the application. In particular, we target those situations where the functions f and g correspond to two conflicting specifications, which are to be jointly optimized. The possible solutions to the optimization problem will depend on the parameter η, which expresses the constraint on g. So, the problem described could be seen as a MOO, where the solutions obtained by varying η represent the Pareto front between the two optimized functions f and g.

1.5 Multiple-Input Power Amplifiers Architectures

1.5.1 Beamforming Arrays

Active beamforming arrays, currently employed in telecommunications systems, present challenges related to linearity specifications and the design of DPD. The traditional SISO DPD is influenced by inherent variations among the PAs within the array and the dynamic loading conditions during

changes in beam direction [33]. These factors can result in suboptimal SISO DPD performance when trained along one beam direction and then applied to other steering angles [34, 35].

Addressing the nonlinear distortion caused by beam dependency may involve real-time identification of DPD coefficients under varying operating conditions [36]. However, this typically necessitates high-performance feedback loops and hardware/software with high complexity, potentially rendering it impractical for real-world deployments. The DPD architecture proposed in [37] achieves real-time linearization of a beamforming device without a feedback loop but requires sensing the output of each PA during the DPD training phase. Additionally, a complex nonlinear predictive function must be calculated in real-time for every DPD coefficient, imposing a heavy burden on signal processing.

However, their performance tends to be suboptimal when the beam is directed at other angles. This is attributed to the mutual nonlinear coupling between the paths of the beamformer and antennas, along with variations in the overall channel response. To address this limitation and enable the use of a single DPD coefficient set for all steering configurations, DPD learning must involve different positions in the identification dataset [34] or leverage MIMO models [38].

1.5.2 Supply Modulated PAs

The enhancement of the spectral efficiency of modern communication standard leads to the use of high PAPR signals. This results in the PA operating in a very low-efficiency area, since its operating point has to be set in a grater back-off region to satisfy linearity constraint. Therefore, in this condition standard class AB/B linear amplifier works far below the point of maximum efficiency. To boost the efficiency in the back-off region various technologies have been proposed over time, which use different techniques to achieve better efficiency, such as load modulation, supply modulation and their hybrids [2]. One of the most promising candidates for this role is the

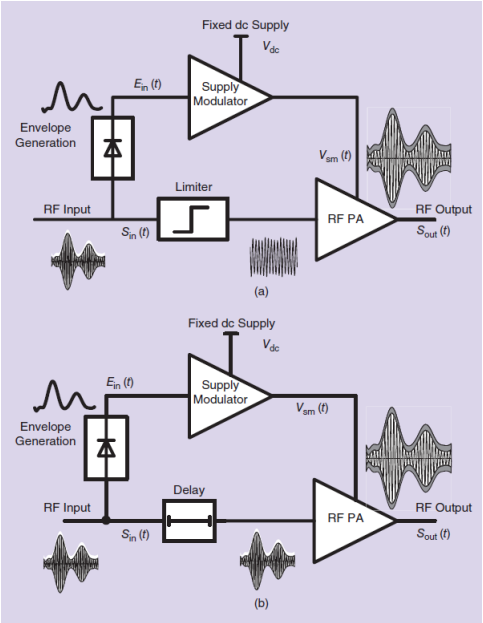

Figure 1.7: a)Envelope Elimination and Restoration b)Envelope Tracking [2].

supply modulation technique, which can be divided into two categories: the envelope elimination and restoration (EER), and ET technique. As shown in Fig. 1.7(a) the EER maintains the PA operating point in the saturation region, so in the point of maximum efficiency, by keeping constant the amplitude of the input signal. Therefore, the amplitude and phase information of the original input signal envelope is split: the phase information remains in the RF path and it is preserved in the actual PA driving signal; while the amplitude information follow the supply path in order to modulate the supply and restore the linear amplification. The ET PA (Fig. 1.7(b)) keeps both phase and amplitude information of the input complex envelope in the RF path. The basic idea of this technique is to drive the PA in its high-efficiency region by dynamically changing the supply voltage, following the amplitude of the input signal envelope. A critical design problem of the supply modulated PA is the nonlinear behavior of the circuit properties as a function of the supply voltage. This is a challenge both from a linearity and an efficiency point of view. For instance, the dependency of the output impedance from

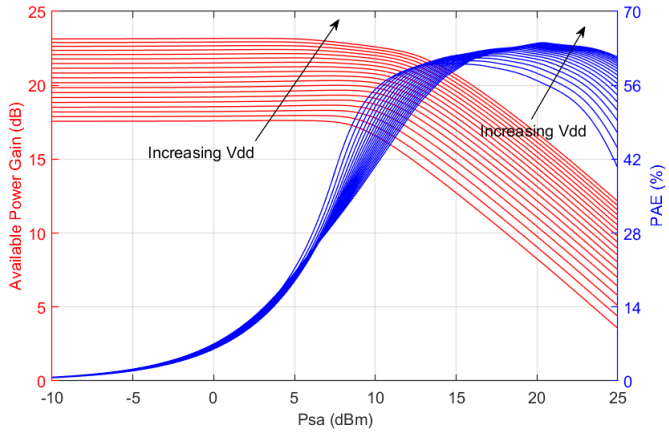

Figure 1.8: PA gain characteristic and PAE with various drain supply voltages (from 10 to 28 V).

the drain voltage may cause a power mismatch and makes it hard to maintain high efficiency for driving a signal with high PAPR. Also when the supply approaches zero the PA tends to shut down, this can cause gain collapse and unpredicted memory effects that increase distortion. Another critical task for the supply modulated architecture is the design of the supply modulator. This base-band amplifier must have sufficient bandwidth to be able to follow the amplitude of the input complex envelope, which is at least twice the input signal bandwidth. Furthermore, EER/ET PA require the use of a high-efficiency supply modulator to increase the overall efficiency.

In ET PA design, the relationship between the input power and efficiency (Fig. 1.8), together with the gain trajectory, can be examined to estimate the potential of the ET architecture applied to a particular PA. Indeed the PAE versus input power characteristic is employed to implement an envelope tracking (ET) system that optimizes efficiency. For this purpose the supply signal must follow the input envelope in order to follow maximum efficiency points for the various input power levels. This can be achieved by implementing a look-up table which ensures that the required voltage is provided to the amplifier for a given envelope amplitude. Choosing a properly designed shaping table, the gain over input power characteristic can be employed to

develop a system that optimize linearity, providing linear gain rather than maximum efficiency.

After the supply modulator design, many factors contribute to performance degradation, such as the already mentioned output impedance mismatch and the poor synchronization between the input envelope and the supply signal. In particular, time misalignment between the PA driving signal and the dynamic drain voltage generated by the supply modulator reduces system efficiency and increases output distortion. Indeed, the poor synchronization between the two waveforms increases power dissipation because the drain voltage minimum will not occur at the same time of RF envelope minimum. Moreover, unconsidered dynamic effect, with the resulting out of phase drain current, may result in output distortion. Waveforms mismatch will also mean that the PA may operate in far compression, causing nonlinear distortion. In addition poor synchronization may be observed in the output signal as a strong memory effect. Once overcome the synchronization problem, the other nonlinear effects can be reduced with a DPD approach. ET PA can be seen as an unique block to which it is possible to add a predistorter, consequently DPD can be performed to optimize linearity requirements.

1.5.3 Load-Modulated PAs

Load-Modulated PA architectures leverage multiple active devices and additional control signals to enhance PA performance with a dynamic change of PAs load conditions. The MI load-modulated architecture tested in this thesis is a variant of the Doherty PA (DPA).

The DPA has gained widespread application in the sub-6 GHz range [39] and is currently under investigation at microwave frequencies in the form of microwave monolithic integrated circuits (MMICs) [40]. In classical DPAs, the input signal is split by a 90-degree quadrature hybrid to feed an auxiliary (peaking) PA, which modifies the output impedance of the main PA at high power.

For proper DPA operation, the design flow should rely on accurate MMIC process design kits (PDKs). However, synthesizing optimal loadlines for broadband signals at high operating frequencies is challenging due to mutual dynamic load-pulling of the transistors in the two branches and the limited fractional BW of the output combiner. While wideband active load-pull characterization techniques [8, 9, 41] theoretically allow for accurate model extraction considering the global device behavior under dynamic active injection, MMIC PDKs are often validated under nominal conditions only and may lack precision for the successful design of MMIC DPAs at microwave frequencies.

An alternative approach, rather than establishing hardware behavior at the design stage, involves leaving additional parameters for load (or supply) modulation as digitally controlled external inputs. In this context, the dual-input DPA (DIDPA) [4] eliminates the implementation of the input 90-degree quadrature hybrid in hardware, enabling the two PA branches to be digitally controlled as independent inputs. The same concept applies to outphasing PAs [5], where the input signal separation network is often implemented digitally. While this approach still allows the digital implementation of the exact nominal behavior of the corresponding hardware version, the availability of multiple control variables provides greater flexibility in fine-tuning the overall PA performance. In principle, these additional degrees of freedom could be utilized to concurrently optimize other FoMs, such as PAE. However, identifying such an optimum may involve inefficient trial-and-error approaches or the formulation of a non-trivial high-dimensionality optimization problem. Consequently, ongoing research explores approaches based on numerical optimization or machine learning for optimal signal-input synthesis and operating point selection of digitally controlled PAs [42, 43], particularly focusing on DIDPAs [44, 45].

1.6 State of the Art

Unlike traditional SISO PA architectures, MI PAs (e.g. the DIDPAs, and SM-PAs) features independent RF inputs for the main and auxiliary amplification branches, similar to load-modulated or outphasing architectures. By controlling these inputs and adjusting the bias voltages, the PA operating conditions can be highly adaptable, optimizing different figure of merit (FoMs). However, effectively tuning the numerous parameters of the DIDPA using automatic optimization methods remains an active area of research [44,45]. The possibility of leveraging the additional degrees of freedom provided by the dual-input architecture has been explored in the literature, both to enhance efficiency and linearity by optimizing the relationships between inputs [4,46,47], and to develop new dual-input DPD architectures [48]. DPD is typically considered in systems that implements digitally controlled load-modulated devices [49,50], due to the strong distortion introduced by these highly-efficient architectures. Nevertheless, joint optimizations that take into account the mutual effects of DPD and variable tuning, especially for K-band devices, are not a particularly explored field in the literature.

In [51], the effect of phase shift in a load-modulated power amplifier is studied as the central frequency varies. It demonstrates that with a proper configuration of various free parameters to optimize the load-modulated PA, it is possible to increase energy efficiency while meeting linearity requirements.

In [52], a linearization method exploiting the dual-input architecture of an SM-PA is presented to improve the efficiency-linearity trade-off. The problem can be considered analogous to the case analyzed in this chapter, replacing the digital parameters used to adjust the supply modulation with those of the DIDPA. Efficiency maximization is achieved through a-priori analysis of the best set of digital parameters, without considering the effects of linearization and DPD on the behavior of the PA.

In [53], the digital parameters of the DIDPA are specifically optimized (e.g., power splitting ratio and relative phase between the two input branches)

to increase its efficiency. A derivative-free heuristic algorithm based on simulated annealing is employed for this purpose. The research demonstrates the potential for a significant improvement in the drain efficiency of a DIDPA by comparing its performance with an analog Doherty PA. The extension of this work is described in [54], and more in detail in [55]. In particular, the authors employ a custom heuristic algorithm based on a combination of simulated annealing and extremus seeking to maximize an objective function that combines linearity and efficiency. The DPD is integrated a-posteriori into the system optimization, repeating the optimization (changing the set of starting parameters) in cases where there is a significant degradation of performance due to linearization.

It is important to emphasize that a common characteristic of the aforementioned works is that DPD is always applied a-posteriori, without considering its effects on the actual distribution of the modulated signal output of the PA. As shown in Fig. 1.9, the distorted signal obtained from a non-linearized PA (e.g., without DPD applied) has a different distribution from that obtained by applying linearization. This different configuration of the output signal can change the value of optimal parameters. Furthermore, to the best of the author's knowledge, all the literature works regarding the optimization of dual-input devices have been validated using DUT with a sub-6GHz frequency target.

1.7 Thesis Organization

The objective of the thesis is to investigate optimization algorithm as well as machine learning techniques able of jointly identify DPD coefficients and PA parameters (when they are accessible by the design). The idea is to enhance PA performance following a generic MOO approach. In order to expose the work done in the sense of MI PAs optimization, the thesis is organized as follows:

- Chapter 2 describes the realization of a real-time beam-dependent DPD

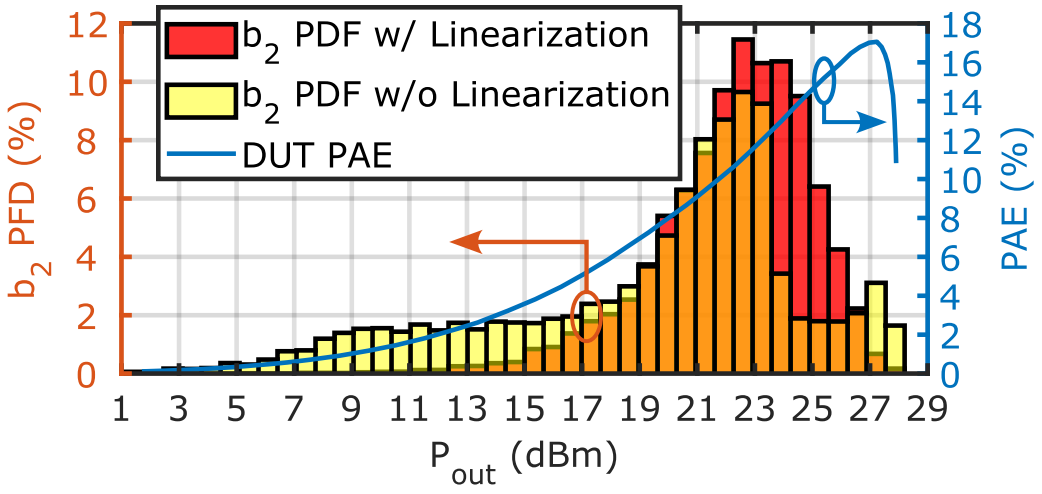

Figure 1.9: Comparison between the distorted and linearized output signal probability density function (PDF) of a given PA with its PAE characteristic.

(BD-DPD) that exploits the MI nature of beamforming arrays to improve device linearity.The MI architecture is exploited to implement a DPD system capable of linearizing the device as the load conditions change with varying beam angles. A machine learning-based strategy is suggested for globally linearizing microwave active beamforming arrays. This approach facilitates the real-time update of DPD coefficients with low complexity by leveraging order-reduced model characteristics. This eliminates the necessity for repetitive local DPD identification steps under diverse operating conditions of the beamformer, such as varying beam angles or RF power levels. The validation of this method is conducted through over-the-air measurements of a 1x4 array operating at 28 GHz over a 100-MHz modulation bandwidth.

- Chapter 3 presents a novel approach for DPD in SM-PAs that utilizes a generalized dual-input architecture. In contrast to traditional methods, this technique treats the SM and RF signals as distinct digital inputs, allowing for their joint predistortion. Employing a MOO strategy facilitates the exploration of inherent PA performance trade-offs

to simultaneously enhance PAE and increase RF output power, while maintaining a specified level of linearity performance. To address the challenge of a high number of experimental acquisitions, MOO is made practical through the rapid simulation of an empirical surrogate model of the PA. This surrogate model is progressively refined based on a limited set of iterative acquisitions. The proposed approach supports the use of a dynamic supply shaping function and automatically considers the statistics of the signals. Ultimately, the method surpasses conventional SM approaches while employing a DPD of the same order, as evidenced by experimental results on a GaN SM-PA operating at 3.5 GHz with OFDM-like high-PAPR modulated signals featuring 10-MHz and 20-MHz bandwidths.

- Chapter 4 describes a preliminary simulation-based work aimed at implementing and comparing optimization strategies to achieve optimal input splitting and biasing of a DIDPA. The Bayesian optimization (BO) is introduced and compared to another derivative-free heuristic optimization algorithm. An example of MOO is described by addressing the competitive maximization of PAE and RF output power.

- Chapter 5 introduces a methodology to optimize the performance of a DIDPA using BO using direct measurement. The BO employs two approaches: one based on a quasi-static model derived from continuous-wave measurements, and the other on direct modulated measurements. The optimization focuses on improving PAE while maintaining linearity with DPD linearization. A joint optimization considers the mutual effect of DPD linearization and PAE-maximization. Validation is performed using a multiport measurement system based on a VNA for wideband characterization of a millimeter-wave dual-input Doherty PA. A dual-input control algorithm is proposed for user-defined control across a 600-MHz bandwidth, enhancing PAE without sacrificing linearity.

Chapter 2

Beamforming Array

2.1 Problem Statement

This chapter describes the realization of a open-loop beam-dependent digital predistortion (BD-DPD), based on the works [35] and [56]. In particular, the BD-DPD exploits the multiple-input nature of beamforming arrays to improve device linearity without requiring feedback or the collection of any other information about individual PAs in the array. A global DPD beam adapter (BA) is identified from a reduced set of measurements at the air interface, providing all necessary information for adjusting DPD coefficients with a minimal number of predictive functions.

2.2 Beam-Dependent Linearization

2.2.1 DPD architecture

The proposed architecture for the BD-DPD, as illustrated in the block diagram in Fig. 2.1, is designed to identify an open-loop BA. Conceptually, the block diagram describes the two main phases of BD-DPD: the offline pre-training procedure which identifies the BA parameters, and the real-time BA. The role of the BA is to dynamically adjust the DPD coefficients

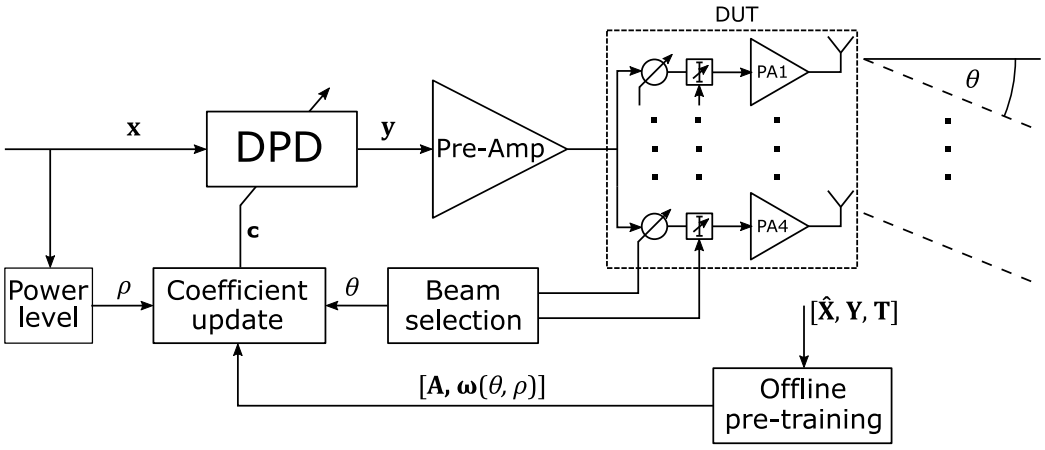

Figure 2.1: Block diagram of the adopted DPD configuration for active beamforming arrays.

along with the operating conditions in a predictive manner, operating without feedback from the output of the array. In this work, varying operating conditions mean the variation of the beam direction angle (θ) and the peak-to-average power ratio (PAPR) of the input signal (ρ). Assuming a linear-in-the-parameters model for the DPD, the open-loop BD-DPD can be expressed as $\boldsymbol{y} = \boldsymbol{X}\boldsymbol{c}(\theta, \rho)$, where $\boldsymbol{y}$ represents the predistorter output, $\boldsymbol{X}$ is the model regression matrix based on the predistorter input $\boldsymbol{x}$, and $\boldsymbol{c}$ denotes the variable predistorter coefficients, dependent on θ and ρ.

The implementation follows a two-phase approach. Firstly, an offline pretraining phase focuses on identifying the parameters of the open-loop BD-DPD generator model. During this phase, the power amplifier (PA) array is linearized for a subset Γ of operating conditions, and the data obtained from this linearization process are utilized to extract the BA model $\boldsymbol{c}(\theta, \rho)$. Subsequently, the real-time linearization phase takes place, where the DPD coefficients are adaptively adjusted by the BA in a predictive manner based on the provided beam angle and input signal PAPR. Notably, this DPD update occurs in an open-loop fashion, without incorporating any feedback in real-time operation.

Given the numerous potential states during the operation of a beamformer

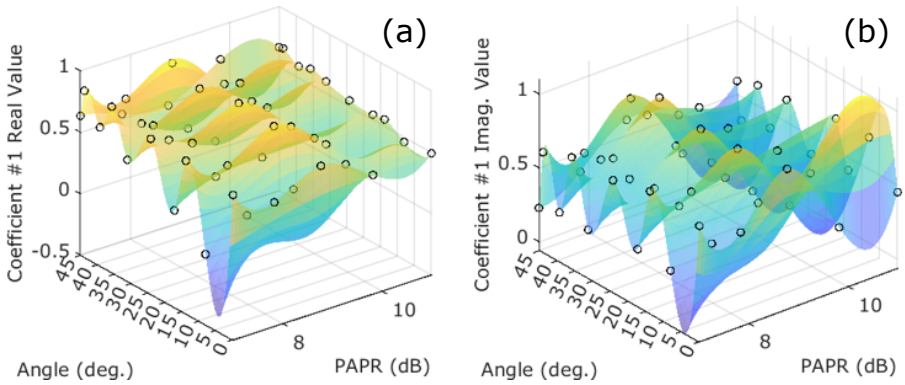

Figure 2.2: (a) Real and (b) imaginary part of the first DPD coefficient while the beam angle θ and the input signal PAPR θ change. The surface is a spline interpolation.

array, the derivation of a comprehensive DPD model might necessitate an extensive array of unique DPD parameter sets ($\boldsymbol{c}(\theta, \rho)$), conceivably requiring one for each state (θ, ρ). However, this approach is susceptible to overfitting. Figure 2.2 describe this concept by showing the variations of one DPD coefficient while changing θ and ρ. Therefore, the practical implementation of the BD-DPD would be too intricate for real-time BA. Consequently, the initial pre-training procedure aims to reduce these coefficients by identifying a diminished set of model features. Recent findings in [57] highlight that the PA behavior can be effectively approximated across various operating conditions using a reduced set of features. The reduced set of features generally represents a better conditioned problem (with a lower overfitting) than the mere prediction of DPD coefficients.

2.2.2 Feature-based Model Reduction

The feature-based model reduction leverages a transformation matrix $\boldsymbol{A}$, which is the change of basis matrix from the adopted DPD model and the reduced model:

$$\boldsymbol{y} = \boldsymbol{X}\boldsymbol{c}(\theta, \rho) \simeq \boldsymbol{X}\boldsymbol{A}\boldsymbol{\omega}(\theta, \rho), \tag{2.1}$$

Here, $\boldsymbol{\omega}(\theta, \rho)$ represents a coefficient vector functioning as a BA and exhibiting a reduced dimensionality compared to $\boldsymbol{c}(\theta, \rho)$. The initial linearization of the beamformer array is achieved using the iterative learning control (ILC) approach [32] applied to the pre-training subset. This process yields a DPD set denoted as $\boldsymbol{c}_k$, consisting of Γ coefficients for each of the K distinct operating conditions:

$$\boldsymbol{c}_k = (\boldsymbol{X}_k^H \boldsymbol{X}_k)^{-1} \boldsymbol{X}_k^H \boldsymbol{y}_k, \tag{2.2}$$

where $\boldsymbol{y}_k$ and $\boldsymbol{X}_k$ are the $N \times 1$ (where N is the number of time-domain complex samples) vectors representing respectively the optimal predistorted signal by ILC and the DPD regression matrix, both corresponding to the kth operating condition. Then, $\boldsymbol{A}$ can be identified by the following minimization problem:

$$\min_{(A)} \sum_k \|\boldsymbol{X}_k \boldsymbol{A} \boldsymbol{\omega}_k - \boldsymbol{y}_k\|^2, \tag{2.3}$$

where $\boldsymbol{\omega}_k$ is the $S \times 1$ reduced set of coefficients for the kth operating condition. As reported in Algorithm 1, a generalized QR-SVD algorithm [57] is here used to solve (2.3) and obtain $\boldsymbol{A}$ by taking as inputs all DPD coefficients and regression matrices structured as:

$$\boldsymbol{C} = [\boldsymbol{c}_1, ..., \boldsymbol{c}_K]; \qquad \hat{\boldsymbol{X}} = [\boldsymbol{X}_1^\top, ..., \boldsymbol{X}_{\hat{K}}^\top]^\top. \tag{2.4}$$

Here, $\hat{\boldsymbol{X}}$ denotes the vertical concatenation of $\hat{K}$ non-repeated $\boldsymbol{X}_k$ matrices from the pre-training set.

The reduced set $\boldsymbol{\omega}_k$ of DPD coefficients for the kth operating condition is ultimately determined by the expression:

$$\boldsymbol{\omega}_k = ((\boldsymbol{X}_k \boldsymbol{A})^H \boldsymbol{X}_k \boldsymbol{A})^{-1} (\boldsymbol{X}_k \boldsymbol{A})^H \boldsymbol{y}_k. \tag{2.5}$$

Subsequently, a global BA model $\boldsymbol{\omega}(\theta, \rho)$ can be derived by interpolating $\boldsymbol{\omega}_k$ across beam angles (θ_k) and input power levels (ρ_k). This study employs either a 2D cubic spline model or a polynomial model for interpolation. To linearize the array, the actual DPD coefficients can be easily updated as

Data: $\hat{\boldsymbol{X}} \in \mathbf{C}^{(N\hat{K})\times\Gamma}$, $\boldsymbol{C} \in \mathbf{C}^{\Gamma\times K}$
Result: $\boldsymbol{A} \in \mathbf{C}^{\Gamma\times S}$
1: Perform QR decomposition on $\hat{\boldsymbol{X}}$: $\hat{\boldsymbol{X}} = \hat{\boldsymbol{Q}}\hat{\boldsymbol{R}}$
2: $\boldsymbol{D} = \hat{\boldsymbol{R}}\boldsymbol{C}$
3: Perform QR decomposition on $\boldsymbol{D}$: $\boldsymbol{D} = \boldsymbol{U}\boldsymbol{\Sigma}\boldsymbol{V}$
4: Select an arbitrary number S of singular values of $\boldsymbol{\Sigma}$
5: Form $\boldsymbol{U}'$: Compress $\boldsymbol{U}$ selecting the S columns that correspond
6: to the selected singular values of $\boldsymbol{\Sigma}$
7: $\boldsymbol{A} = \hat{\boldsymbol{R}}^{-1}\boldsymbol{U}'$

Algorithm 1: Generalized QR-SVD Algorithm

$\boldsymbol{c} = \boldsymbol{A}\boldsymbol{\omega}(\theta, \rho)$, utilizing the value of $\boldsymbol{\omega}(\theta, \rho)$ corresponding to the given beam angle and input signal PAPR. The introduced SVD-based procedure solves the automatic selection of a reduced set of significant features ($S \ll K$) for the global BA behavior. Consequently, it significantly reduces the number of coefficients needed for effective beam adaptation. Instead of storing and interpolating across a total of $\Gamma \times K$ DPD coefficients obtained from pre-training at K different operating conditions, it is sufficient to store a much smaller $\boldsymbol{A}$ matrix ($\Gamma \times S$) and the $S \times 1$ interpolated functions $\boldsymbol{\omega}(\theta, \rho)$.

2.3 Over-the-Air Measurement Setup

The implemented over-the-air (OTA) configuration (Fig. 2.3) operates at 28 GHz. Up/down conversion from an intermediate frequency (IF) of 1.55 GHz is executed using a two-way mixer (TMYTEK UDBox) with a shared local oscillator. A Keysight M8190 arbitrary waveform generator is utilized for generating modulated signals at IF. The IF receiver comprises a Mini-Circuits ZRL-2150+ low-noise amplifier and a wideband oscilloscope (Keysight DSO9254A) with a 500-MHz acquisition bandwidth (BW).

The device-under-test (DUT) is a 1x4 active beamformer array (TMYTEK BBoard), equipped with signal splitting and individual power amplification,

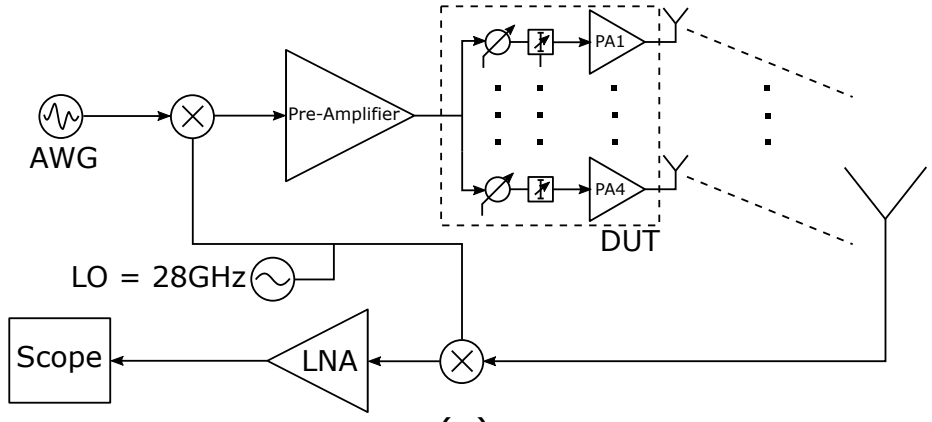

(a)

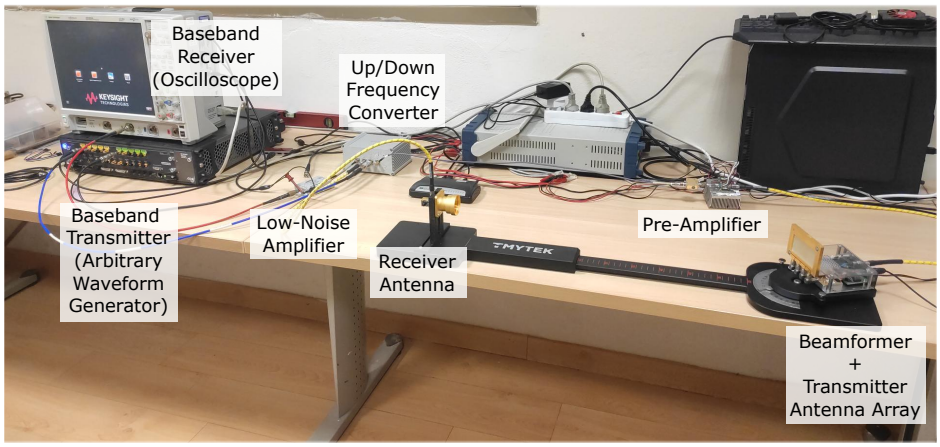

(b)

Figure 2.3: (a) Block diagram and (b) photo of the OTA measurement setup.

attenuation, and phase control in each signal path. The beamformer is powered by an Analog Devices HMC943 preamplifier, driving the four integrated PAs into their nonlinear region with up to 5-dB compression, resulting in a maximum available output power of 10 dBm for each path. The signal is OTA-transmitted by a 4-way patch antenna array and received in the far-field by a horn antenna. The excitation signals are random-phase multi-tone signals with BW = 100 MHz, with statistics matched to a Gaussian OFDM-like signal. The assessment of linearization performance involves measurements of the adjacent channel power ratio (ACPR) and error vector magnitude (EVM).

2.4 Experimental Results

2.4.1 DPD Identification

The selected pre-training set comprises a systematic sampling of $K = 50$ distinct operational points, uniformly chosen across the θ, ρ parameter space illustrated in Fig. 2.4 (depicted as blue circles). The beam angle is incrementally adjusted in 5° intervals, while the input power encompasses signals with varying PAPRs ranging from 7 dB to 11 dB, all possessing the same peak power. It is worth noting that this specific choice for the pre-training set is not exclusive, and alternative strategies, such as Latin hypercube sampling, can be adopted [58].

By employing Algorithm 1 and assessing the singular values obtained for $\boldsymbol{D}$ (Fig. 2.5a), a dimensionality of $S = 5$ for $\boldsymbol{\omega}(\theta, \rho)$ has been identified as suitable for the array-under-test. This determination is based on the residual error being below the targeted normalized mean square error (NMSE) threshold of -45 dB, as outlined in this study. As illustrated in Fig. 2.6, the interpolation results for the first complex component of $\boldsymbol{\omega}(\theta, \rho)$ across beam angle and PAPR, using both the adopted third-order polynomial model and the 2D cubic spline, exhibit favorable fitting characteristics. The chosen parametric structure for the predistorter is the generalized memory poly-

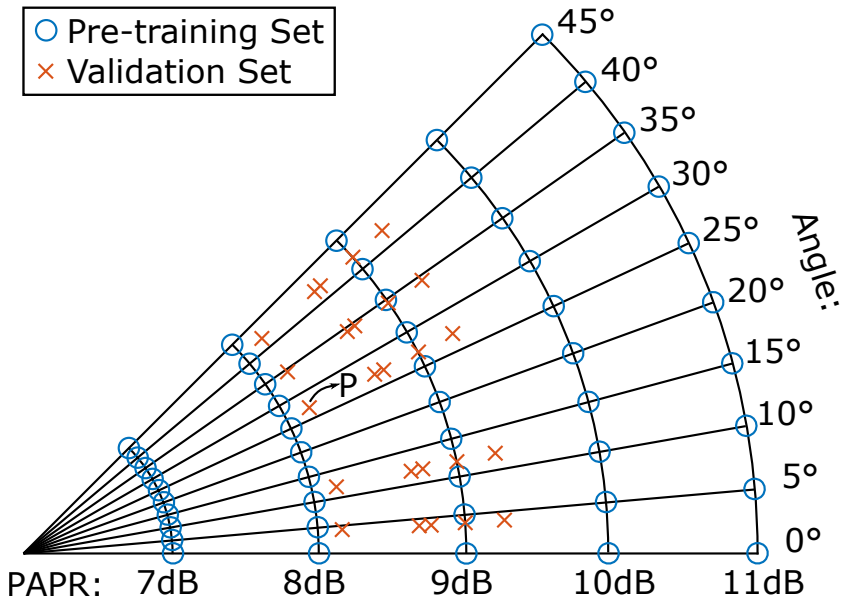

Figure 2.4: Array operating conditions used as a pre-training set (blue circles) and as a validation set (red crosses).

nomial (GMP) model [59]. Specifically, the GMP nonlinear, memory, and cross-memory orders are set to 7, 9, and 1 respectively, ensuring a NMSE of -49 dB between the non-parametric predistorted signal (obtained through ILC) and the signal modeled by the GMP-based predistorter (Fig. 2.5b).

2.4.2 DPD Validation

The validation of BD-DPD encompasses examination across 25 distinct operating conditions in different beam angles and PAPR values across the considered ranges, as illustrated in Fig. 2.4 (depicted as red crosses). The performance evaluation, presented in Fig. 2.7, compares the proposed BD-DPD against a fixed DPD strategy. The fixed DPD involves utilizing a constant set of coefficients derived from a single operational scenario ($\theta = 0°, \text{PAPR} = 11$ dB), maintained invariant across different beam directions and input signal PAPR. To provide context, Fig. 2.7 also includes cases without DPD and the scenario representing the optimal achievable DPD

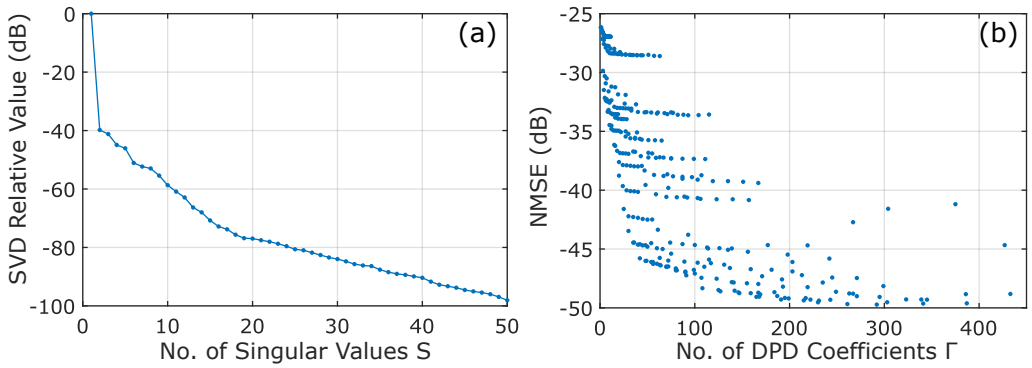

Figure 2.5: (a) Singular values of matrix $\boldsymbol{D}$ as from Algorithm 1. (b) Model fitting error (NMSE) of the GMP-based predistorter.

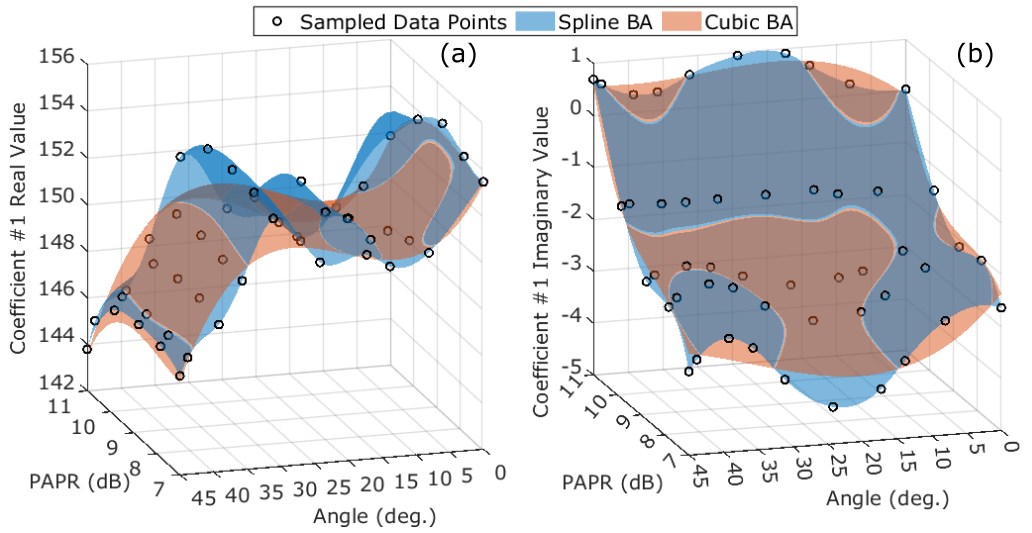

Figure 2.6: Cubic polynomial and spline interpolation of the first reduced feature across all tested conditions. (a) Real and (b) imaginary part.

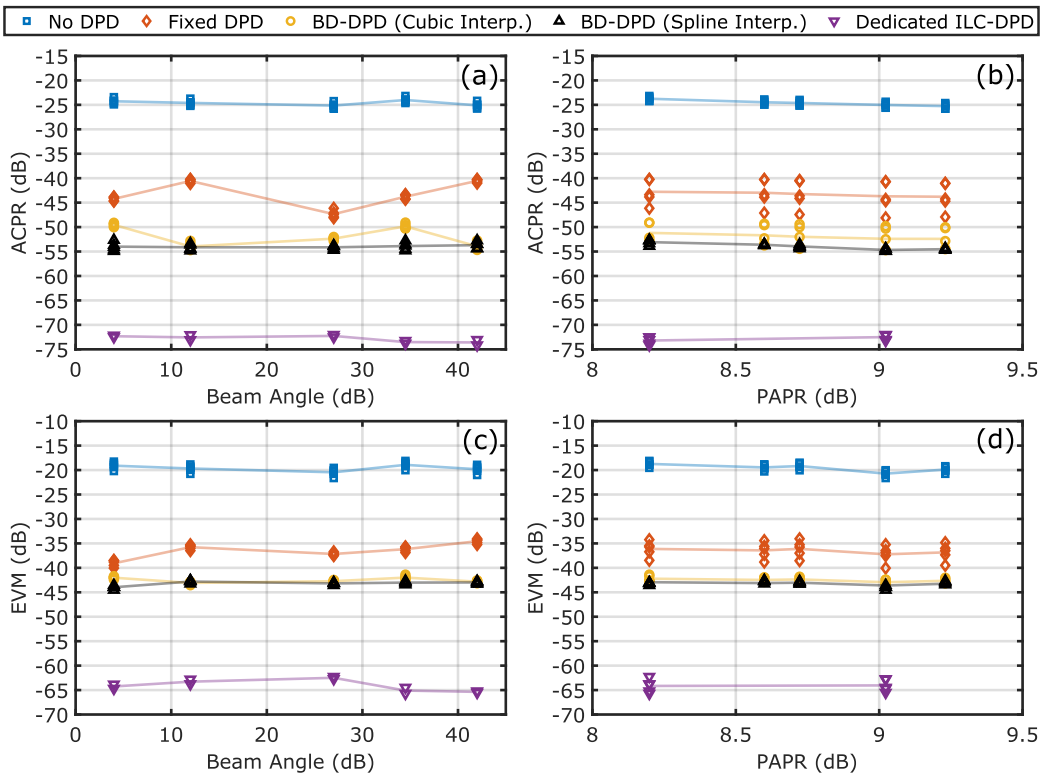

Figure 2.7: DPD performance comparison. (a) ACPR and (c) EVM in the validation points plotted across beam angle. (b) ACPR and (d) EVM in the validation points plotted across PAPR. The continuous line indicates the average value in a given DPD configuration across all tested operating conditions.

performance. The optimal performance is achieved through a dedicated non-parametric ILC-DPD approach, extracted individually for each operating condition.

Figure 2.7 distinctly reveals a consistent reduction in distortion attributed to variations in beam directions and PAPR for both implemented BA interpolations. In Figs. 2.7a-b, the BD-DPD demonstrates enhancements of approximately ~ 5 dB and ~ 10 dB in terms of ACPR for cubic and spline BAs, respectively. The corresponding improvements in EVM are approximately ~ 5 dB for both implemented methods, as depicted in Figs.2.7c-d. Figures2.8a-b illustrate the gain and AM/PM characteristics of the non-predistorted and predistorted array in a specific operating condition from the validation set ($\theta = 27°$, PAPR = 8.2 dB). Additionally, the corresponding output spectra are presented in Fig. 2.9.

2.5 Computational Complexity Analysis

In addition to improving the linearity of the beamforming system, the proposed technique allows for a reduction in computational complexity during the real-time operational phase, compared to similar techniques in literature. The BD/DPD complexity is compared to [37], where a power- and beam-dependent DPD with P_{DPD} basis functions (or DPD coefficients) is proposed. A model with a number of coefficients $P_{PA} = P_{DPD}$ is extracted for every PA of the array during pre-training phase. Then, a set of N_F reduced features is extracted from the PA models and linearly combined during the real-time coefficient update phase to obtain the reduced array model. Eventually, these features are further combined into a DPD generator with nonlinear order K obtaining the updated DPD coefficients.

Compared to [37], the proposed method does not require a separate modeling of every PA of the array during the pre-training procedure, since the pre-training procedure is performed by measuring the combined distorted output of the array. This allows for scaling up the technique to beamforming

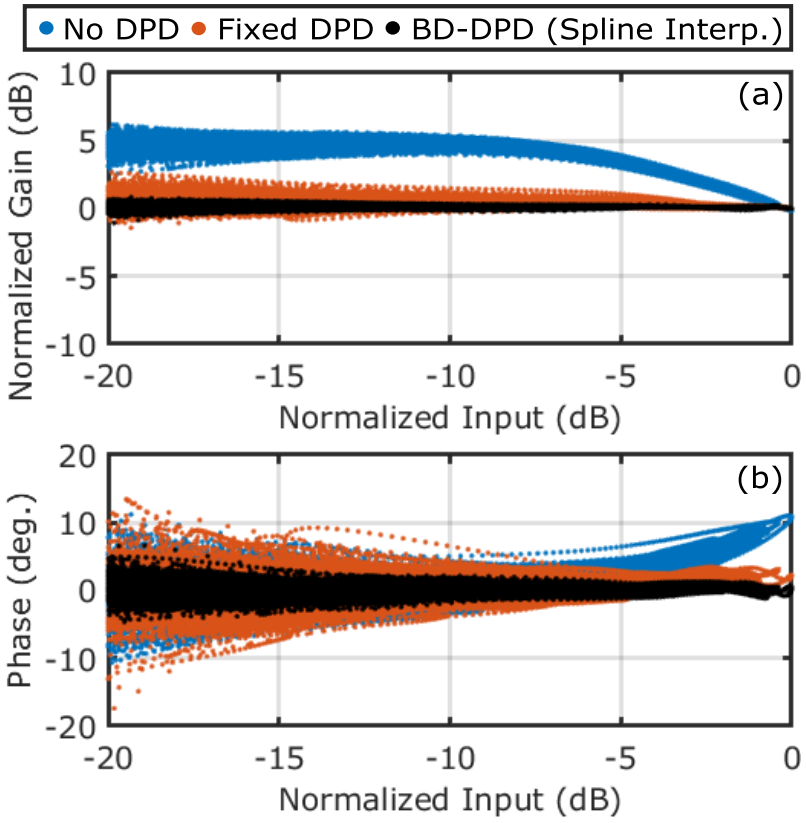

Figure 2.8: (a) Gain and (b) phase characteristics of the predistorted and non-predistorted array in the test condition P as from Fig. 2.4 ($\theta = 27°$, PAPR = 8.2 dB).

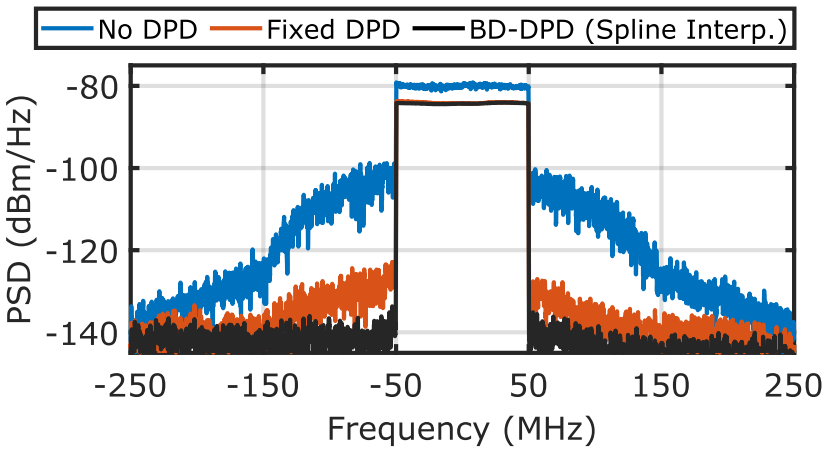

Figure 2.9: Spectrum of the predistorted and non-predistorted array in the condition P as from Fig. 2.4 ($\theta = 27°$, PAPR = 8.2 dB).

arrays with a high number of PAs. In addition, the proposed method does not depend on the number of PAs in the array, neither during the pre-training phase nor in the real-time DPD adaptation.

Moreover, Table 2.1 shows that the proposed method requires less complex multiplication if $K > 1$. This table compares the total number of complex multiplications required for the proposed method, the one in [37], and the basic case of a dedicated training for each way of the array (applicable numerical data has been provided and adapted to this work), showing the advantage of the proposed method.

2.6 Achievements

An architecture for BD-DPD leveraging feature-based model reduction tailored for beamformer arrays is introduced. The array-level application of feature-based reduction is independent from the number of PAs within the array. This feature-based approach implements a low-complexity update of the DPD for the array, adjusting it based on the beam direction and RF power level, without requiring extraction of a different DPD coefficient set for each operating scenario. The proposed BD-DPD is effective in significantly

	Dedicated Training	Wang [37]	Proposed Method
PA Model Generation	$N_S \bullet P_{PA}$	N/A	N/A
Array Model Generation	$N_{PAs} \bullet P_{PA}$	$N_{PAs} \bullet N_F$	N/A
DPD Coefficient Generation	$P_{DPD}^2 \bullet (N_S + P_{DPD} + 1) + + P_{DPD} \bullet N_S$	$N_F \bullet K \bullet P_{DPD}$	$N_F \bullet (P_{BA} + P_{DPD})$
Total Complex Multiplications	$\simeq 622 \bullet 10^9$	$20 + 920 \bullet K$	986

Table 2.1: Number of total complex multiplication needed during the real-time DPD coefficients update. Where $P_{PA} = P_{DPD} = 184$ and $N_F = 5$. $N_{PAs} = 4$ is the number of PAs in the beamforming array. $N_s = 10^5$ is number of samples in the tested signal. $P_{BA} = 14$ is the equivalent number of complex-valued multiplications that are required in the 2D cubic interpolation of the real and imaginary part of the function $\boldsymbol{\omega}(\theta, \rho)$. K is not provided since there is no analogous value in the method proposed in the manuscript that can be adapted.

reducing DUT in-band distortion and residual out-of-band regrowth across all tested beam directions and PAPR levels.

Chapter 3

Supply-Modulated Power Amplifier

3.1 Problem Statement and State of the Art

This Chapter explores a comprehensive digital predistortion (DPD) framework incorporating an optimal digital control strategy, intending to leverage the degrees of freedom provided by MIs to enhance power amplifier (PA) performance. Traditional DPD for PA linearization typically approaches the problem as an optimization task focused on minimizing the deviation between the actual PA output signal and the desired amplified signal. In contrast, this work introduces an additional concurrent maximization for other PA Figures-of-Merits (FoMs), implementing a multi-objective optimization (MOO) approach. When solely considering linearity, DPD may not lead to optimal operation in compromise with other FoMs. MOO or any constrained optimization (CO) has seldom been applied to DPD coefficient learning [42, 60, 61], and it has not been explored in the context of multiple-input single-output (MISO) PAs. Although MOO has been investigated recently, it has been mainly applied to set specific design parameters without including DPD coefficients as optimization variables, performing DPD in a separate step [45, 53, 62–66].

This Chapter focuses on the case of supply-modulated PAs (SM-PAs), utilizing the complex RF envelope and dynamic supply voltage as independent inputs (Fig. 3.1b). In envelope-tracking (ET) [7], a static shaping table (ST) maps the signal envelope to a proportional supply voltage control, typically shaped for maximum average power added efficiency (PAE), see Sec. 1.5.2. While such shaping is commonly envisioned at the design stage and extracted from CW measurements at different supply voltages [7, 67], the compensation of nonlinear distortion induced by supply modulation (SM) is often assumed to be handled by single-input single-output SISO DPD, as depicted in Fig. 3.1a [7]. In some cases, the dependency on the supply voltage has been included as an additional variable within the RF path predistorter (RF predistorter) [18, 68–71] or compensated separately [72], but without joint control of the controlled variables. In the proposed approach, no preliminary supply control waveform is extracted since both the low-frequency (LF) supply control and RF input control (i.e., the two predistorted signals) are entirely unknown at the start of the PA optimization. Both LF and RF signal are jointly identified, considering the mutual effect on the linearity and efficiency of the PA. This method is applicable to any type of SM-PA, such as ET or polar. Essentially, the two inputs are concurrently identified through an optimization-based DPD learning process, implementing a true joint optimal control.

This Chapter summarizes the results published in [73]. It is an extension of the preliminary work on where a dual-input single-output (DISO) DPD for SM-PAs [74], which employed a combination of gradient descent and linearization through indirect learning control (ILC) [75]. The gradient descent, relying on finite differences approximation for each DPD coefficient, was acquired through simulation-based evaluations of the device-under-test (DUT) and directed towards the maximum PAE point. The ILC-based step performed classical linearization of the PA, obtaining a second optimization direction to uphold the linearity constraint. The algorithm alternated between these two directions. As indicated in [74], it became evident that

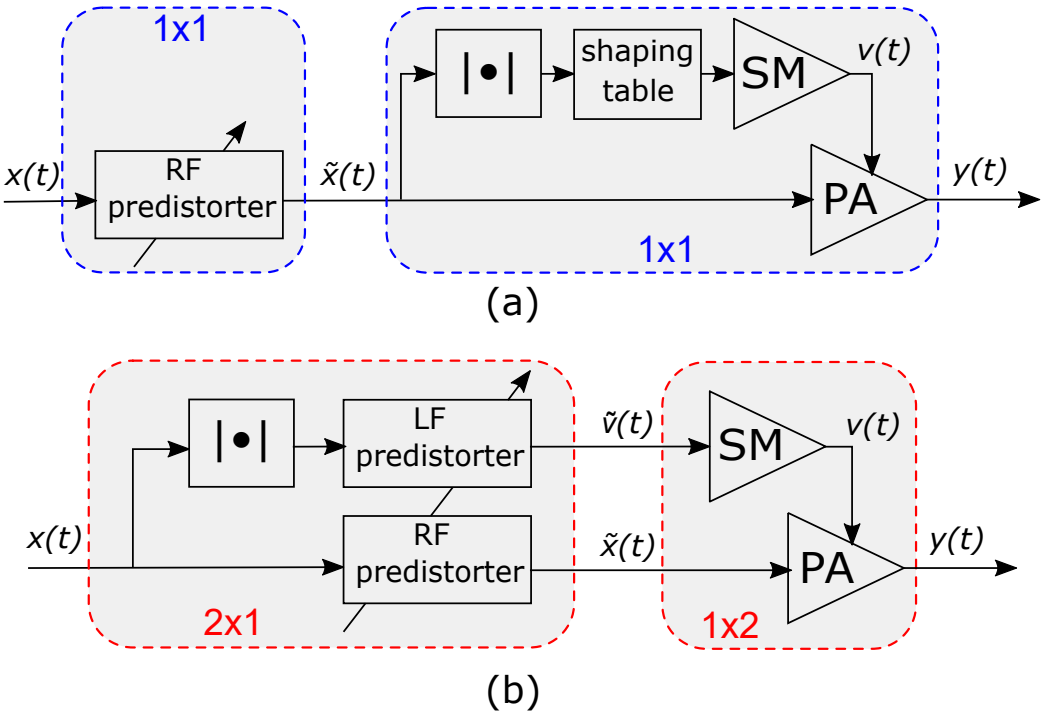

Figure 3.1: Block diagram for ET PA linerization with (a) SISO predistorter and (b) single-input dual-output predistorter with joint RF-LF coefficient learning.

practically any data-intensive optimization approach, where complex DPD coefficients are the variables to be optimized, would result in an impractical number of DUT evaluations (i.e., actual PA measurements in an experimental setting).

The adopted optimization employs an even more computationally demanding algorithm than in [74]. Yet, to make it experimentally feasible, a surrogate modeling approach [76] is adopted. Surrogate modeling (SuMo) is well-established in electromagnetic optimization [76–79] and has been explored for active devices in circuit design [80], transistor compact modeling [81], and adaptive optical amplifiers [82].

Section 3.3 provides details of the measurement setup employed for SM-PAs to demonstrate the proposed technique. In Sec. 3.4, a preliminary static analysis is conducted to assess the achievable PA performance when choosing

the two control signals solely from CW characterization. The performance evaluation of the DUT optimized using the SuMo-based MOO framework is presented in Section 3.6. Concluding remarks are presented in Section 3.8.

3.2 Joint Dual-Input Digital Predistortion

3.2.1 Multi-objective Optimization

Considering the general MOO problem described in Sec. 1.4.4, this Section describe the MOO problem definition in the case of SM-PAs performance enhancement. The SM-PA can be represented as a DISO 1×2 system block, illustrated in Fig. 3.1b. In this configuration, the joint predistorter/supply shaper takes the form of a 2×1 block, featuring two parallel paths for RF and LF signals. This design enables control at both RF (for the PA input) and LF (for SM), with the control policy expressed through two parallel predistortion blocks. These blocks can be parametrically represented, with each output serving as a nonlinear dynamic mapping of the input signal $x(t)$:

$$\begin{aligned} \tilde{x}(t) &= \mathcal{R}(x(t-\tau), \boldsymbol{\rho})\tau \in [0, T_m]; \\ \tilde{v}(t) &= \mathcal{L}(x(t-\tau), \boldsymbol{\lambda})\tau \in [0, T_m]. \end{aligned} \tag{3.1}$$

Here, $\tilde{x}$ and $\tilde{v}$ denote the RF and LF control signals, T_m is the maximum memory length, and $\boldsymbol{\rho}$ and $\boldsymbol{\lambda}$ are vectors of parameters for the functions $\mathcal{R}$ and $\mathcal{L}$, respectively. $\mathcal{R}$ and $\mathcal{L}$ are the functions that respectively identify the RF and LF predistorter of Fig. 3.1b. This parametrized structure accommodates a broad range of predistorters and STs, allowing the implementation of various joint supply modulation and DPD strategies based on the RF/LF coefficient values [17]. Notably, both LF and RF predistorters can incorporate a full nonlinear-dynamic structure to account for memory effects induced by the dynamic RF input and supply [17], extending the standard approach for ET PAs that typically implements a static function to realize the supply modulation.

To optimize the overall SM-PA performance with a fixed predistorter structure and a specified number of coefficients, a MOO problem is formulated. The goal is to identify coefficient values for the LF and RF branches $\boldsymbol{\rho}$ and $\boldsymbol{\lambda}$ that maximize or minimize multiple scalar figures of merit (FoMs). For instance, a typical objective for SM-PAs is to maximize PAE in modulated conditions while adhering to regulatory linearity constraints. This MOO problem can be equivalently expressed as a CO problem using the ϵ-constraint approach [83], where one FoM is optimized while the others are constrained by limit values ϵ. Different trade-off solutions can be obtained by varying the constraint values, allowing the identification of a Pareto front of non-dominated solutions.

Consider a simplified case where two FoMs f and g are involved, with f to be maximized and g to be constrained (e.g., PAE and NMSE, respectively). The corresponding CO problem, equivalent to an MOO task, is defined as follows:

$$\max_{\boldsymbol{\rho},\boldsymbol{\lambda}}; f(\boldsymbol{\rho},\boldsymbol{\lambda}) \quad \text{subject to}; g(\boldsymbol{\rho},\boldsymbol{\lambda}) < \epsilon. \tag{3.2}$$

Various algorithms from literature [83] are available for solving such problems, each offering different computational trade-offs and solution localities. Irrespective of the method chosen, multiple evaluations of f and g are required for iterative convergence toward an optimized solution.

While the functional relationships described by f and g are typically not known analytically due to their dependence on complex factors such as specific PA and SM devices, signals of interest, and predistorter model structures, their values for given coefficient sets $\boldsymbol{\rho}$ and $\boldsymbol{\lambda}$ can be experimentally evaluated. This involves generating LF/RF predistorter blocks using the coefficients, producing the correct RF/LF control signals, and collecting measured responses from the DUT to compute all FoMs. Depending on the number of coefficients, predistorter complexity, and algorithm employed, the optimization process may necessitate a substantial number of DUT measurements, potentially making it time-consuming for practical applications.

3.2.2 Surrogate Modeling

To mitigate the additional workload due to the iterative optimization algorithms, many SuMo strategies have been proposed in the literature [79] across various applications in diverse fields. SuMo methods entail an initial establishment of a simplified model for the DUT. The premise is that this SuMo can reasonably approximate the DUT behavior while being highly efficient in execution. Consequently, to arrive at a provisional iterative solution for optimization, the CO algorithm can invoke the SuMo multiple times instead of conducting DUT measurements.

For the SuMo, any model formulation can be employed, provided it is sufficiently accurate to characterize the DUT and suitable for the chosen CO, such as being continuous and differentiable for gradient-based optimizers. Additionally, the SuMo simulation time should be sufficiently short in comparison to the time required for measurement and data transfer. In the context of the configuration depicted in Fig. 3.1b, a dual-input PA behavioral model is utilized as the SuMo for the SM-PA, as elaborated in Sec. 3.2.4.

Due to the imperfect approximation properties, there will inevitably be a deviation between the performance predicted by the SuMo and the measured one. However, the SuMo can be iteratively refined to furnish an improved representation of the DUT behavior. These model refinement steps can be interleaved with CO steps, during which the refined SuMo is leveraged to determine the predistortion coefficients for optimizing performance.

3.2.3 SuMo-based MOO algorithm

This section describes the SuMo-based MOO algorithm by referring to the flow chart in Fig. 3.2, which summarizes the steps of the optimization process. The SuMo extraction is initialised with an initial set of excitations at both inputs, thereby collecting the measured PA response in an initial dataset $\mathcal{D}^{(0)}$, which contains the applied control inputs and the measured outputs. These initial excitations are designed to thoroughly explore the PA behavior,

identifying an initial coarse SuMo model $\mathcal{M}^{(0)}$ that best approximates the PA behavior with a minimal number of acquisitions (see Sec. 3.2.4). The preliminary verification ensures that the deviation between the measured PA response and the response predicted by $\mathcal{M}^{(0)}$ for the initial excitations is sufficiently small, ensuring proper implementation and faithful reproduction of the measured quantities.

In the first optimization step, the CO algorithm is launched, employing $\mathcal{M}^{(0)}$ to evaluate the objective f and constraint g, yielding a tentative DPD coefficient set $\boldsymbol{\rho}^{(0)}, \boldsymbol{\lambda}^{(0)}$ intended to jointly optimize the performance metrics. These identified coefficients generate the predistorted LF/RF inputs, which are then experimentally tested on the actual DUT. Generally, these coefficients may not be precise for the PA, as they are identified using the response of $\mathcal{M}^{(0)}$ as a proxy for real measurements.

The input-output measurements from this stage are assembled in a new dataset $\mathcal{D}^{(1)}$, reflecting the actual behavior of the SM-PA when the $\boldsymbol{\rho}^{(0)}, \boldsymbol{\lambda}^{(0)}$ values are employed in the predistorter. Subsequently, the algorithm checks the exit conditions, which could be determined by evaluating a maximum number of iterations, the incremental improvement [61], or by reaching a specified PA performance in terms of the analyzed FoMs.

If the exit conditions are not met, the procedure iterates. A new refined SuMo $\mathcal{M}^{(1)}$ is identified using the new $\mathcal{D}^{(1)}$ dataset, in conjunction with the previously available dataset $\mathcal{D}^{(0)}$. This refined SuMo is expected to more closely align with the observed PA behavior in the optimal operating point of interest, as $\mathcal{D}^{(1)}$ is measured under conditions more similar to the final ones. The $\mathcal{M}^{(1)}$ is then utilized for another CO step, in which a new set of coefficients $\boldsymbol{\rho}^{(1)}, \boldsymbol{\lambda}^{(1)}$ is determined. The procedure is repeated until the exit criteria are satisfied.

In general, at the ith iteration, the following steps are executed:

1. **SuMo identification**: a new SuMo $\mathcal{M}^{(i)}$ is identified using the measured datasets collected up to that point $\mathcal{D}^{(0)}, \ldots, \mathcal{D}^{(i)}$.

2. **Constrained Optimization**: $\mathcal{M}^{(i)}$ is employed to evaluate f and g

during a CO step, where the tentative optimal predistorter coefficients $\boldsymbol{\rho}^{(i)}, \boldsymbol{\lambda}^{(i)}$ are sought as maximizers of f, while adhering to $g(\boldsymbol{\rho}^{(i)}, \boldsymbol{\lambda}^{(i)}) < \epsilon$.

3. **LF/RF Predistortion Testing**: the LF/RF predistortion coefficients $\boldsymbol{\rho}^{(i)}, \boldsymbol{\lambda}^{(i)}$ are tested on the DUT, with the input and output waveforms of interest collected in the dataset $\mathcal{D}^{(i+1)}$..

4. **Exit Condition Check**: exit conditions, potentially dependent on the measured performance of the DUT during the measurement $\mathcal{D}^{(i+1)}$, are assessed.

These iterative steps of SuMo identification, CO of the SuMo, and DUT measurements should ensure that the SuMo predictions progressively converge to the actual DUT performance (at least in a neighborhood of the final solution) and that optimal coefficients for the two DPD branches are identified. Upon completing the last iteration, the identified coefficients should ideally maximize f while adhering to the constraint g in the actual measurements, even though they were identified using a SuMo for both FoMs at each step. Once a suitable solution is achieved, the algorithm can be restarted with different values for the ϵ constraint on g to identify different trade-offs between the two FoMs of interest.

3.2.4 Multi-Objective Optimization Implementation

In the context of the adopted SM solution (Fig. 3.1b), the SuMo needs to characterize the entire transmitter, encompassing both the supply modulator device and the PA. Specifically, it should establish a functional mapping between the control inputs $\tilde{x}$ and $\tilde{v}$ and the measured RF output $y(t)$, the actual supply voltage $v(t)$, and the supply current $i(t)$ (Fig. 3.1b). These quantities are then employed to compute the values of the relevant FoMs during the MOO procedure.

The SuMo should ideally encompass the overall transmitter efficiency, modeling the power consumed by the supply modulator driving the PA. How-

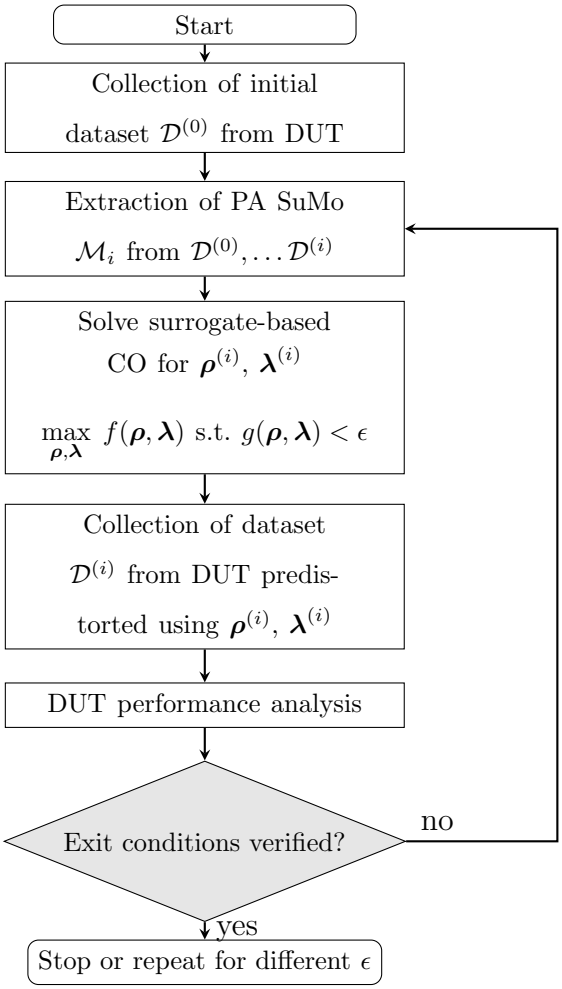

Figure 3.2: Flow chart of the surrogate-based MOO algorithm for joint RF input/supply DPD.

ever, in this specific study, a linear supply modulator topology is employed (see Sec. 3.3), which is characterized by low-efficiency performance. Typically, multi-level or bandwidth-limited switching converters are used for this purpose [67, 84]. Given this configuration, the global optimization of the supply modulator and PA is not suitable. Instead, the optimization focuses solely on the PAE of the RF PA, omitting the supply modulator efficiency in the calculations. Nevertheless, the framework can be theoretically extended to bandwidth-limited or switched cases using a suitable SuMo to describe

the behavior of the entire transmitter (SM+PA) and employing appropriate FoMs (e.g., global efficiency instead of PA efficiency).

As highlighted in the Introduction, PA behavioral modeling has been extensively explored in the literature, with some works considering the presence of MIs [11], such as the supply input in SM-PAs [17]. Among various approaches, the memory polynomial (MP) formulation stands out as one of the most common solution, offering a satisfactory description of the PA with a reasonably limited number of coefficients and, consequently, fast simulation time. Thus, in the adopted implementation, the SuMo for the PA is represented by the following dual-input MP model:

$$y(n) = \sum_{m=0}^{M_\delta} \sum_{k_1=1}^{K_\delta} \sum_{k_3=0}^{K_\delta+1-2k_1} \delta_{m,k_1,k_3} \tilde{x}(n-m)|\tilde{x}(n-m)|^{2(k_1-1)} \tilde{v}(n-m)^{k_3}, \quad (3.3)$$

where $\tilde{x}(n)$ and $\tilde{v}(n)$ are the sampled versions of the inputs (RF input envelope and baseband input to the supply modulator, respectively), and $y(n)$ is the sampled RF output envelope. K_δ and M_δ are the nonlinear and memory orders. Additionally, beyond the RF output, the baseband current $i(n)$ absorbed by the PA is modeled to obtain the PAE, as described by the following real-valued dual-input MP:

$$i(n) = \sum_{m=0}^{M_\sigma} \sum_{k_1=1}^{K_\sigma} \sum_{k_3=0}^{K_\sigma+1-2k_1} \sigma_{m,k_1,k_3} |\tilde{x}(n-m)|^{2(k_1-1)} \tilde{v}(n-m)^{k_3}. \quad (3.4)$$

Considering that the SM is never ideal in setting the prescribed supply voltage waveform $v(n)$ (sampled version of $v(t)$ in Fig. 3.1), the same formulation in (3.4) is adopted for modeling $v(n)$ as a function of the same two digital controls $\tilde{x}(n)$ and $\tilde{v}(n)$.

In the SuMO, the RF and LF DPD structures are chosen to match the same degree of description. The RF predistorter model within the 2×1 block in Fig. 3.1b is based on the classical MP:

$$\tilde{x}(n) = \sum_{m=0}^{M_\rho} \sum_{k=1}^{K_\rho} \rho_{m,k} x(n-m)|x(n-m)|^{2(k-1)}, \quad (3.5)$$

where $\rho_{m,k}$ are the RF DPD coefficients, K_ρ is the nonlinearity order, and M_ρ is the memory depth. Correspondingly, the adopted supply control, which generalizes the static ST approach, is processed by an MP-based LF predistorter:

$$\tilde{v}(n) = \sum_{m=0}^{M_\lambda} \sum_{k=1}^{K_\lambda} \lambda_{m,k} |x(n-m)|^{2(k-1)}, \tag{3.6}$$

where $\lambda_{m,k}$ are the LF DPD coefficients, K_λ is the nonlinearity order, and M_λ is the memory depth. These orders should be selected to achieve the linearity and efficiency targets dictated by the application. Simultaneously, an upper limit to the predistorters model order is indirectly imposed by the MOO algorithm, as excessively optimizing a large number of variables can significantly reduce the convergence speed and stability of the method.

The MP formulations in (3.3) and (3.4) are linear-in-the-parameters, allowing the SuMo to be straightforwardly extracted through linear regression across an experimental dataset. The initial dataset $\mathcal{D}^{(0)}$ in Fig. 3.2 needs to be carefully designed to offer a sufficiently comprehensive MP-based description, steering the MOO promptly in a suitable optimization direction. For this purpose, the applied controls should span the available variable space for $\tilde{x}$ and $\tilde{v}$ maximally. Simultaneously, the operating regime of the DUT should not deviate significantly from the target regime resulting from the modulation signal of interest, as large discrepancies might lead to slow convergence or oscillating behavior between the SuMo and the DUT.

The selected compromise for $\mathcal{D}^{(0)}$ involves applying, at the RF input, an amplitude-scaled version of the desired RF modulated output. The supply modulator input comprises a random-phase modulated excitation, interleaved in frequency with respect to the RF input, ensuring broad coverage of the dual-input variable space [85]. This approach dynamically repeats a given frame of the RF input at many supply voltage values within a single waveform record, resulting in an operating point similar to the target one, yet general enough to properly condition the MOO. Subsequently, the tentative optimum is experimentally tested, and new measurement data $\mathcal{D}^{(i)}$ is

collected. In the next iteration, the SuMo is extracted from a cumulative database of all previously collected data, progressively refining it toward the target regime while maintaining a degree of global description. Although other adaptive sampling methods could be considered, this approach has proven effective (see Sec. 3.6).

While various CO algorithms could be explored [83], this work utilizes the interior-point algorithm [86], implemented by the fmincon function in MATLAB®. It solves the CO by treating it as a sequence of approximate minimization problems, where the constraint is converted into a logarithmic barrier function. The algorithm employs a combination of second-order derivative or conjugate gradient methods to solve the approximate problem. For setting up the CO, the following definitions have been applied:

- The objective function (f) is related to the PAE of the PA, excluding consideration of the supply modulator performance in this context;
- The constraint function (g) is based on the Normalized Mean Square Error (NMSE), given by:

$$\text{NMSE (dB)} = 20\log_{10}\frac{||\mathbf{y} - G_{\text{lin}}\mathbf{x}||2}{||G\text{lin}\mathbf{x}||2}; \tag{3.7}$$

  where $\mathbf{y}$ and $\mathbf{x}$ represent the vectors for the RF output and input signals of the RF predistorter (see Fig. 3.1b). The linearity constraint can be aligned to the communication standard specifications, linking linearity to metrics like Adjacent-Channel Power Ratio (ACPR) or Error-Vector Magnitude (EVM). While these metrics could also be considered [61], the specific choice of NMSE addresses both in-band and out-of-band distortions, making it the most commonly used in DPD literature;
- The linearization gain (G_{lin}) in (3.7) is a fixed parameter selected for each optimization process, determining the average RF output power (P_{out});
- The constraint limit ϵ is translated into a maximum NMSE selected for each optimization process. A realistic constraint should consider

the deviation between the actual performance and the one predicted by SuMo. The constraint value varies across different CO runs to outline a specific segment of the Pareto front representing non-dominated solutions for the MOO problem.

3.3 Measurement Setup

A measurement configuration designed for SM-PAs is depicted in Fig. 3.3 to showcase the proposed technique. The DUT is a 10-W PA operating in class-AB at a central frequency $f_c = 3.5$ GHz, utilizing the CGH40010F Gallium Nitride HEMT from Wolfspeed for the PA and the ADA4870 driver amplifier from Analog Devices to realize the SM. To enable dynamic supply, the original PA evaluation board had its largest supply capacitors (33 μF, 1 μF, and 33 nF) removed.

The adopted supply modulator has a maximum 1-A output current, approximately 4.5 voltage gain, 50-MHz large-signal bandwidth, and a 2500-V/μs slew rate. It is biased for a supply voltage swing ranging from 8 V to 28 V. Despite the device stability ensured by a 5-Ω output resistance, it introduces non-idealities in applying the dynamic supply voltage due to an inherent interdependence between the current drawn by the PA and the actual supply voltage. Baseband voltage and current are sensed at the SM-PA node using a traditional 1:10 high-impedance probe and a 100-MHz clamp current sensor (Keysight N2893A), respectively. Although this supply terminal configuration may introduce additional distortion due to spurious dynamics of the baseband voltage, the proposed SuMo model is expected to describe and automatically compensate for these broadband SM nonidealities during the MOO routine [87].

The RF input is generated via direct RF synthesis using a Keysight M8190 arbitrary waveform generator (AWG) operating at 8 GSa/s, preamplified by the Mini-Circuits ZHL-42W+ amplifier. The dynamic supply voltage waveform provided to the supply modulator input (LF input) is generated

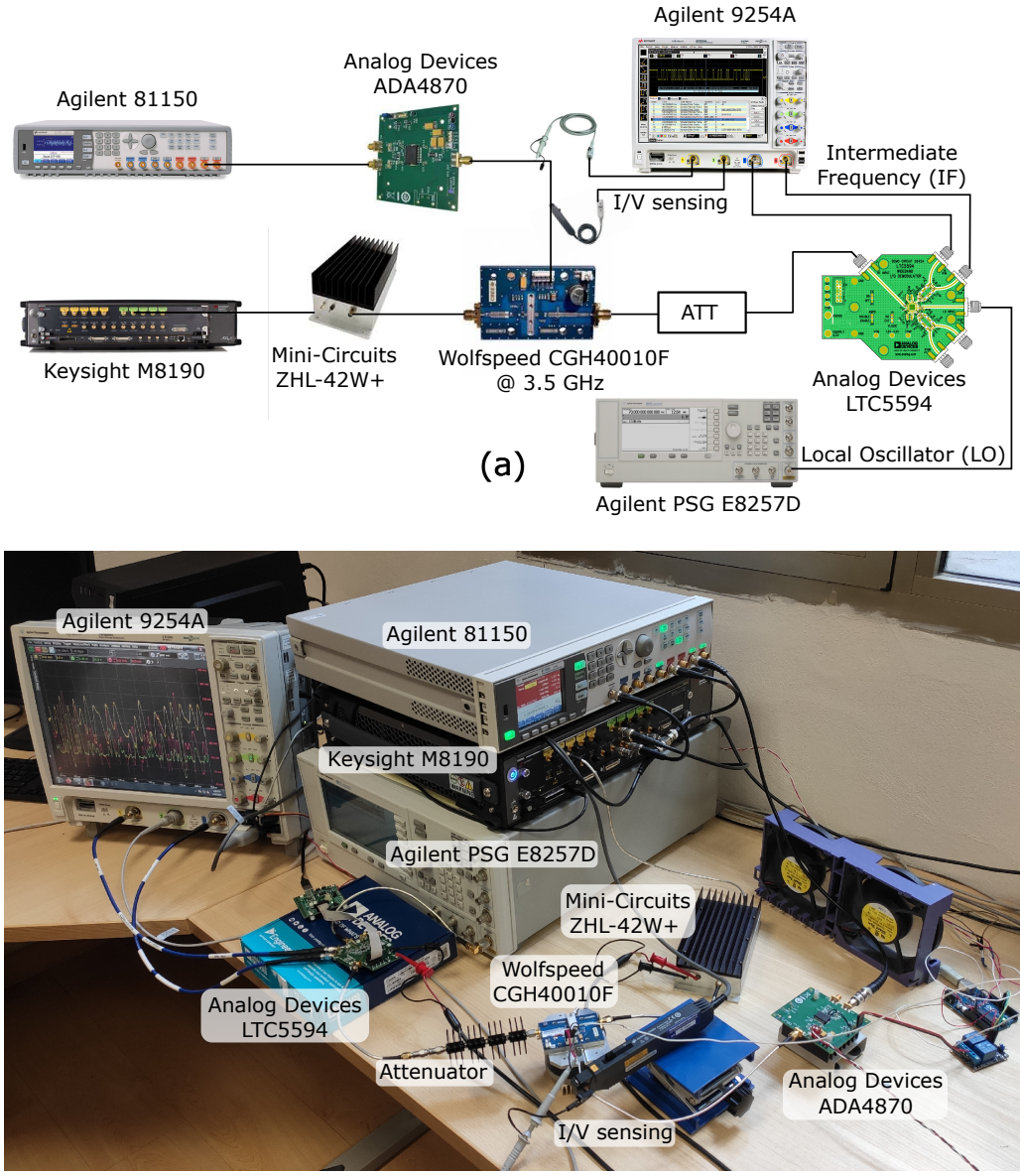

Figure 3.3: Block diagram (a) and photo (b) of the measurement setup for supply-modulated PAs used to perform the experiments.

using a 2 GSa/s Agilent 81150 AWG. Both RF and LF signal generators share a common 10-MHz reference, with synchronization achieved through a trigger signal from the 81150.

Given the a-priori unknown supply waveform, a procedure is implemented to characterize and compensate for the time-invariant delay between the RF and LF inputs. Initially, a random-phase multi-tone excitation is applied to the RF input while maintaining a DC voltage at the supply. This step allows retrieving the delay on the RF input - RF output envelope path ($\tau_{RF} \simeq 3.3$ ns). Subsequently, a random-phase multi-tone excitation is applied to the LF input while maintaining a CW excitation at the RF input, realizing a suitable up-conversion of the LF excitation to retrieve the delay between the LF input - RF output envelope ($\tau_{LF} \simeq 4.3381$ μs). The identified delays are then compensated in signal generation.

Following attenuation, the DUT output is down-converted by the LTC5594 I/Q mixer from Analog Devices, with its local oscillator (LO) synthesized by the Agilent E8257D. The outputs of the mixer are captured by a 4-channel oscilloscope (Agilent 9254A) featuring a bandwidth of up to 2.5 GHz and a sampling rate of up to 20 GSa/s. The two remaining oscilloscope channels are employed for supply-terminal voltage/current sensing.

3.3.1 Synchronism between LF and RF Branches

With this setup, given that no supply waveform is a-priori known, an initial identification and compensation of the delays (due to measurement triggering and hardware, e.g., preamplifier, baseband sensing, etc.) of the RF and LF branches should be performed. In particular, an approach similar to [88] has been followed:

1. a random-phase multi-tone excitation is applied to the RF input, while keeping a dc voltage at the supply. This step allows to retrieve the delay on the RF input - RF output envelope path (τ_{RF});

2. a random-phase multi-tone excitation is applied to the LF input, while keeping a CW excitation at the RF input. This step allows to realize a suitable up-conversion of the LF excitation, so to retrieve the delay on the LF input - RF output envelope (τ_{LF}).

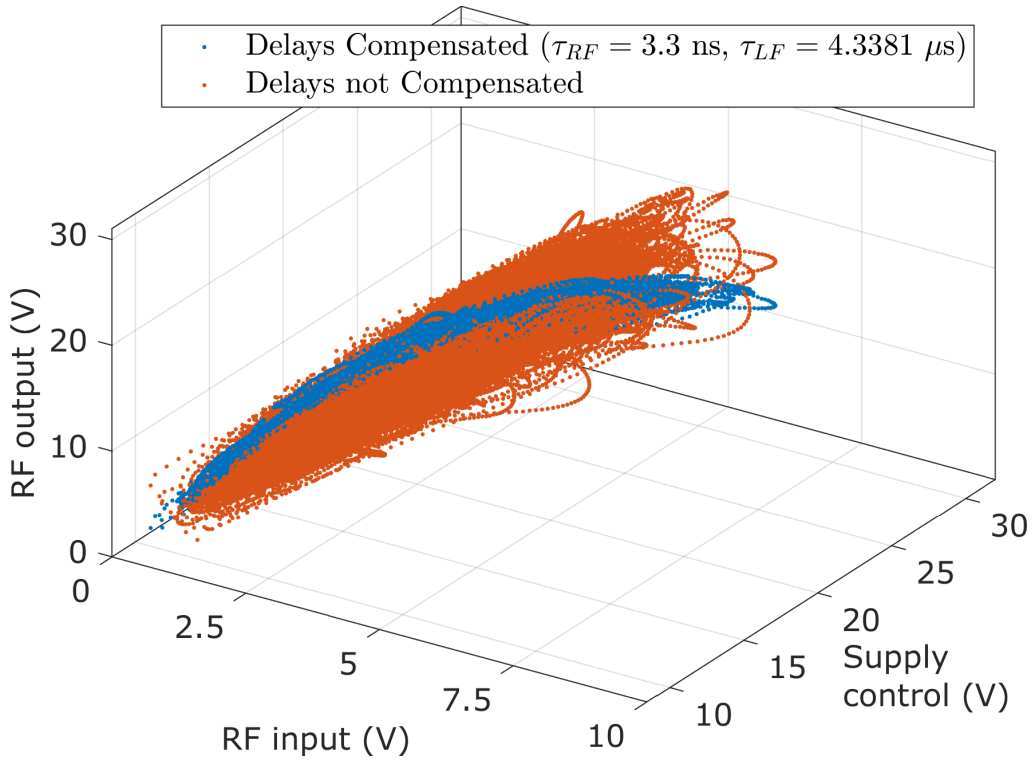

Figure 3.4: Result of the delay compensation. The reported values for the input controls are the ones realized at the PA ports, in linear scale (V).

As can be seen from Fig. 3.4, the RF output before compensation is characterized by a strong hysteresis with respect to the two inputs due to delay misalignment. After applying the compensation of $\tau_{RF} \simeq 3.3$ ns and $\tau_{LF} \simeq 4.3381$ μs, the trajectory of the RF output is reasonably approximated by a surface, which indicates that the dual-input PA can be roughly described by a 2D quasi-static relationship, demonstrating the effectiveness of the delay compensation procedure.

Clearly, beside the delay compensation, the SM-PA will still feature residual nonlinear dynamic effects, which have to be accounted for in the SuMo procedure and DPD formulation/learning process. Finally, as the SuMo accurately models the PA behavior and its dynamics due to both inputs, the joint MOO of the RF and LF paths is able to steer the input controls in an optimal way for both amplitude range and bandwidth. While a wrong

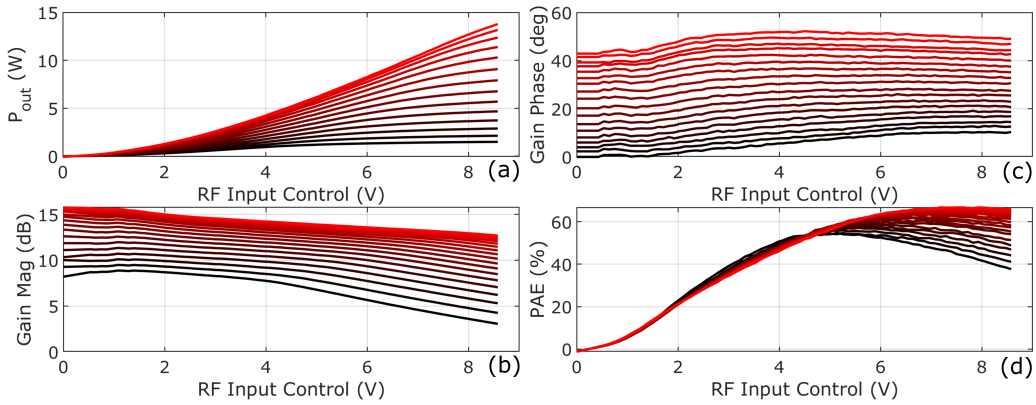

Figure 3.5: Output power (a), static gain (b)-(c) and PAE (d) characteristics of the SM-PA for different values of the RF and LF control voltages. The RF input power ranges from 2.6 dBm to 28.6 dBm (shown in linear scale on the x-axis). The LF control is swept in order to obtain measured the drain voltages in the 8 V (black) to 30 V (red) range. The Rayleigh probability density function for an input rms power of 19 dBm of interest is shown in (e).

solution could be realized across the iterative steps, this will result into a lower PA performance, hence the MOO algorithm will automatically adjust the controls at the subsequent iteration towards improved performance and proper supply modulation.

3.4 Preliminary Static Analysis

A static analysis of the PA represents the typical starting point for the design of SM and DPD strategies [7]. The AM/AM and AM/PM characteristics, as well as the dissipated power, are measured by concurrently sweeping the power of an input RF CW excitation and the dc supply voltage. The static output power, gain and PAE characteristics, measured at a fixed CW with $f_c = 3.5$ GHz, are reported in Figs. 3.5a-d. The maximum RF input control is selected in order to reach the 3-dB compression point with respect to the small signal gain (16 dB) at the nominal drain voltage of 28 V. At

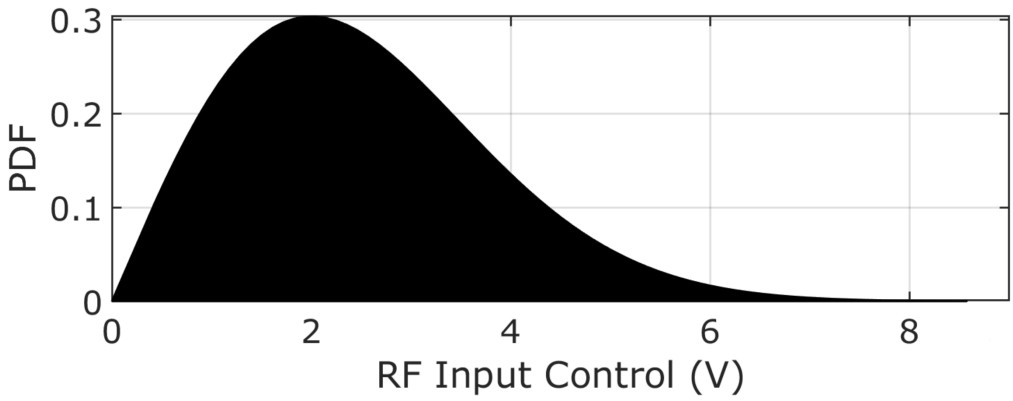

Figure 3.6: Rayleigh probability density function for an input rms power of 19 dBm of interest.

the same time, the LF control is swept in order to obtain measured drain voltages in the 8 V to 30 V range.

The selection of the static control law $\tilde{v}(n) = h(|\tilde{x}(n)|)$, derived from the memoryless relationship between the two control variables, can be approached in various ways. Three distinct strategies are considered for comparative analysis:

- Fixed Supply Voltage. This scenario reflects the PA behavior without the SM, maintaining the drain voltage at a specified level, considered as a baseline. In this particular case, $\tilde{v}$ needs a slight increment with $\tilde{x}$, proportional to the current absorbed by the PA, to compensate for the voltage drop across the 5-Ω output resistance of the supply modulator (refer to Sec. 3.3). The fixed supply voltages tested cover the range from 8 V to 28 V.

- Maximum PAE. For a constant RF input power, the DUT will exhibit varying PAE values based on the LF control $\tilde{v}$, as illustrated in Fig. 3.5d for the curves PAE$(|\tilde{x}|, \tilde{v})$. This strategy, for each RF input control value $\tilde{x}$, selects the LF input control $\tilde{v}$ that maximizes the PAE. Additional shaping can be applied to prevent undesirable irregularities in the resulting characteristics.

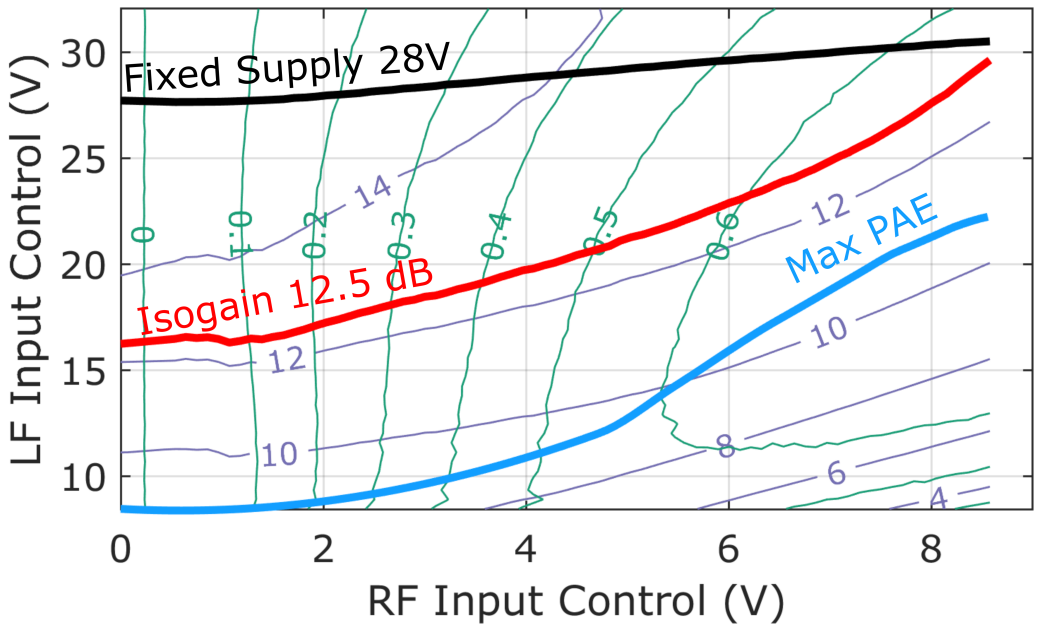

Figure 3.7: Static supply-shaping strategies for the SM-PA under test: fixed supply (28 V, black), iso-gain (12.5 dB, red) and maximum PAE (cyan). The RF input power ranges from 2.6 dBm to 28.6 dBm (shown in linear scale on the x-axis). Gain magnitude (purple) and PAE (green) contours with respect to the control variables are also reported.

- Iso-gain. The LF control $\tilde{v}$ is chosen to ensure that an identical gain magnitude is achieved for all RF input powers. This involves selecting a suitable iso-line of the gain $|G(|\tilde{x}|, \tilde{v})|$ response surface in Fig. 3.5b-c. While equalizing the gain of the DUT, this strategy still necessitates DPD to compensate for AM/PM distortion and any residual amplitude deviation. This characterization analyzes constant gains in the range of 9 dB to 12.5 dB.

For the PA under examination, Figure 3.7 illustrates the resulting supply STs along with the static gain and PAE contours. Although non-parametric look-up tables are a conceivable implementation for the static h functions, the prevalent approach involves utilizing a parametric representation [3], such as the one presented in (3.6). As emphasized in Sec. 3.2, the adoption of a

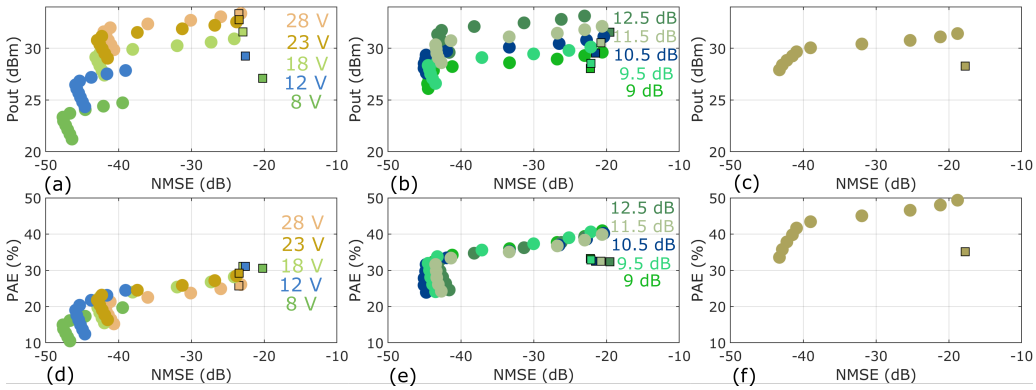

Figure 3.8: RF Output Power, NMSE and PAE trade-offs for fixed supply (a-d), iso-gain (b-e) and (c-f) maximum PAE shaping strategies. Squares indicate the non-linearized case, circles indicate the statically predistorted case using a 5-th order polynomial.

parametrized ST is crucial for the proposed MOO framework. Hence, to ensure an fair comparison (i.e., same model complexity) between classical supply-shaping methods and those derived from MOO (Sec. 3.6.1), the STs in Fig. 3.7 were implemented using a static polynomial ($M_\lambda = 0$) of order $K_\lambda = 5$ (6 real coefficients). A preliminary assessment of the SM-PA performance can be derived from the static characterization for each ST. Specifically, the average RF input power $P_{\text{in}}(|\tilde{x}|, \tilde{v})$, the average RF output power $P_{\text{out}}(|\tilde{x}|, \tilde{v})$, the DC dissipated power $P_{\text{dc}}(|\tilde{x}|, \tilde{v})$, and the complex gain $G(\tilde{x}, \tilde{v})$ are known static functions of the LF/RF control variables $\tilde{x}$ and $\tilde{v}$.

A comprehensive evaluation of the effectiveness of each shaping strategy becomes apparent only after applying predistortion to the SM-PA. Once h is determined, implementing DPD becomes feasible by adopting the SISO SM-PA configuration in Fig. 3.1a. DPD structures theoretically allow for dynamic terms to accommodate memory effects, practical implementation involves testing the PA under modulated excitations. The static CW characterization, on the other hand, provides information for a correspondingly static DPD. In practical terms, obtaining a static predistorter involves identifying a suitable mapping $\tilde{x}(n) = q(|x(n)|)x(n)$ between the ideal x and predistorted $\tilde{x}$ signals.

For this static case, we adopt an indirect learning architecture (ILA) DPD with a polynomial formulation for q, consistent with (3.5), where a fifth-order nonlinearity ($K_\rho = 5$) is selected, and no memory is considered ($M_\rho = 0$).

As stated in Sec. 1.2, To provide a accurate assessment of prospective performance under modulated conditions, the static PA characteristics can be appropriately weighted by the probability density function (PDF) of the stationary stochastic process representing the excitation signal class to which the ideal input x belongs [89]. For orthogonal-frequency-division-multiplexing (OFDM) waveforms, widely adopted in 5G and other telecommunications standards, the asymptotic envelope is complex-gaussian [90]. The amplitude then follows a Rayleigh distribution, as depicted in Fig. 3.5e for an input rms power of 19 dBm. Due to finite measurement time in the characterization stage, the amplitude distribution and spectral characteristics of the process of interest can be accurately emulated using various noise-like or random-phase multi-tone excitations [9].

For a given set of h and q, the statistical properties of the excitation signal need to be considered in the static prediction. To this end, let us define the statistical expectation values [89] for the considered FoMs:

$$\begin{aligned} P_{\text{out}} &= \int_0^{+\infty} \widehat{P}_{\text{out}}(u)\text{pdf}(u)du; \\ \text{PAE} &= \frac{\int_0^{+\infty} \left(\widehat{P}_{\text{out}}(u) - \widehat{P}_{\text{in}}(u)\right) \text{pdf}(u)du}{\int_0^{+\infty} \widehat{P}_{\text{dc}}(u)\text{pdf}(u)du}; \\ \text{NMSE} &= \frac{\int_0^{+\infty} |\widehat{G}(u)q(u) - G_{\text{lin}}|^2 u^2 \text{pdf}(u)du}{\int_0^{+\infty} |G_{\text{lin}}|^2 u^2 \text{pdf}(u)du}; \end{aligned} \tag{3.8}$$

where the variable $u = |x|$ is employed to represent the ideal envelope amplitude in a simplified notation:

$$\begin{aligned} \widehat{G}(u) &= G(|\tilde{x}|, \tilde{v}) = G\left(|q(|x|)x|, h(|q(|x|)x|)\right); \\ \widehat{P}_{\text{in}}(u) &= P_{\text{in}}(|\tilde{x}|, \tilde{v}) = P_{\text{in}}\left(|q(|x|)x|, h(|q(|x|)x|)\right); \\ \widehat{P}_{\text{out}}(u) &= P_{\text{out}}(|\tilde{x}|, \tilde{v}) = P_{\text{out}}\left(|q(|x|)x|, h(|q(|x|)x|)\right); \\ \widehat{P}_{\text{dc}}(u) &= P_{\text{dc}}(|\tilde{x}|, \tilde{v}) = P_{\text{dc}}\left(|q(|x|)x|, h(|q(|x|)x|)\right). \end{aligned} \tag{3.9}$$

The integrals in (3.8) can be computed using adaptive quadrature or Monte-Carlo methods, considering the measured static PA characteristics and the known signal distribution.

The Pareto sets depicting these metrics for the three examined SM strategies are illustrated in Fig. 3.8a-c. For each shaping technique (h), a set of q different DPD coefficient sets are evaluated, sharing the same model structure and complexity but differing in G_{lin}. This approach enables the exploration of conflicting requirements between P_{out} and NMSE in each case [61]. The fixed supply characteristics in Fig. 3.8a exhibit the lowest overall PAE for a given level of P_{out} and linearity. Conversely, the shaping technique for maximum PAE predictably displays the highest PAE values while exhibiting poor linearity for all tested DPDs. The iso-gain characteristics show an intermediate behavior, featuring a favorable trade-off between RF P_{out}, PAE, and NMSE after linearization.

A maximal (or non-dominated) point is defined as a point for which no other point in the set has all better metrics simultaneously (i.e., linearity, PAE, and P_{out} in this case). In the context of MOO, maximal points can be seen as exhibiting the best overall PA performance for the given constraints. The different shaping techniques and DPD strategies highlight that some points in the Pareto sets in Fig. 3.8 are not maximal. Indeed, the existence of dominated points demonstrates that certain SM and DPD techniques are, in this respect, suboptimal. As investigated in the following, this implies that one or more metrics can be improved without sacrificing the others by simply identifying proper DPD coefficients.

3.5 Choice of the DPD Model

The final linearity and the PA efficiency in the presented approach depend on both the SuMo used for the optimization and the model for the RF and LF predistortion/supply modulation branches.

In terms on the SuMo, if the model was not accurately reproducing the

PA behavior, the MOO algorithm would converge to a solution which might be optimal for it, but not for the actual PA. At the same time, the SuMo must be computationally efficient to evaluate as the MOO algorithm, which typically requires several thousands of evaluations of the cost functions in order to find a solution. The proposed framework is already fully compatible with other types of SuMo (e.g. artificial neaural networks), as long as they can fulfill these accuracy/computational load requirements.

In terms of the LF/RF DPD models, the use of a more complex formulation can indeed increase the overall linearity and efficiency performance of the PA. However, the number of coefficients in the model directly impacts the number of variables that have to be optimized by the MOO algorithm. Functions of a higher number of variables are typically more challenging to optimize, requiring a proportionally higher number of evaluations of the cost functions and presenting worse convergence properties.

Therefore, this work focuses on a memory-polynomial type of formulation for the RF DPD and LF supply modulation branches in order to test the novel proposed framework preliminary using a simple (i.e., relatively low number of coefficients) and well-known model. Moreover, this choice allows for a straightforward comparison with other common approaches for identifying the DPD/supply modulation controls of similar complexity. Indeed, the use of a more complex model or the same formulation with more terms can be a valuable future step in order to further optimize the PA performance and test the capabilities of the MOO algorithm to provide optimal solutions in more challenging cases.

3.6 Optimization Results

3.6.1 MOO-based Static Shaping Table

The MOO procedure outlined in Sec. 3.2 has been implemented for a specific target signal: a 10-MHz bandwidth random-phase 1k-tone modulated signal with a peak-to-average power ratio (PAPR) of 9.3 dB, adhering to the

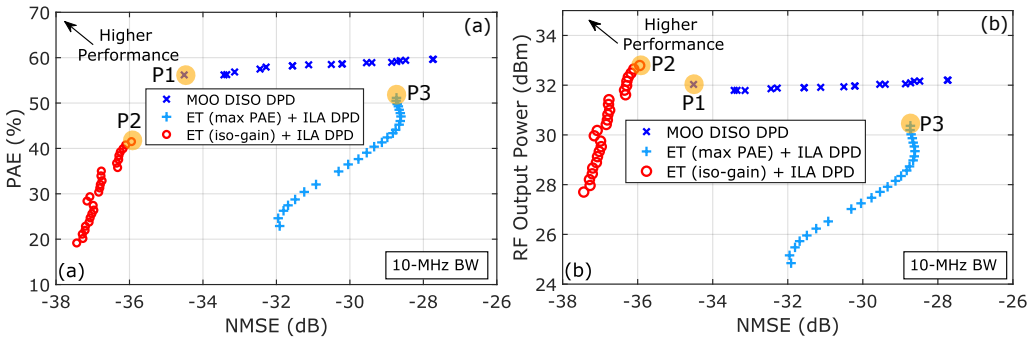

Figure 3.9: MOO-based Pareto front for maximum PAE and constrained NMSE using a static ST (dark blue x), compared with the standard iso-gain ST (@ 12.5 dB) with SISO DPD (red circles) and maximum PAE ST with SISO DPD (light blue +). The corresponding DPD complexity is reported in Table 3.1. The test signal is a 10-MHz random-phase 1k-tone with PAPR = 9.3 dB.

statistical properties discussed in Sec. 3.4. The dual-input SuMo, described by (3.3) and (3.4), is characterized by $M_\sigma = M_\delta = 3$ and $K_\sigma = K_\delta = 7$, parameters identified as suitable for describing the DUT under this specific operational condition. The DPD, specified by (3.5) and (3.6), has a configuration of $M_\rho = 2$ and $K_\rho = 5$ for the RF predistorter, and $M_\lambda = 0$ and $K_\lambda = 5$ for the LF predistorter. With $M_\lambda = 0$, the MOO is utilized to derive a static ST, allowing for a direct comparison with the conventional CW-based approaches. For the chosen nonlinear and memory orders, the total number of optimized real variables is 36, comprising 15 complex coefficients for the RF predistorter and 6 real coefficients for the LF predistorter.

The Pareto set of non-dominated points is derived systematically, maximizing the PAE at different Normalized Mean Square Error (NMSE) constraint values (indicated by blue x in Fig. 3.9a), while maintaining a constant G_{lin} in all instances. The chosen G_{lin} corresponds to the 3-dB gain compression level achieved at the fixed drain bias of 28 V, resulting in $P_{\text{out}} \simeq 32$ dBm (blue x in Fig. 3.9b), which equates to $\simeq 41.5$ dBm peak power. Each point on the resultant Pareto front corresponds to a specific set of LF/RF predistor-

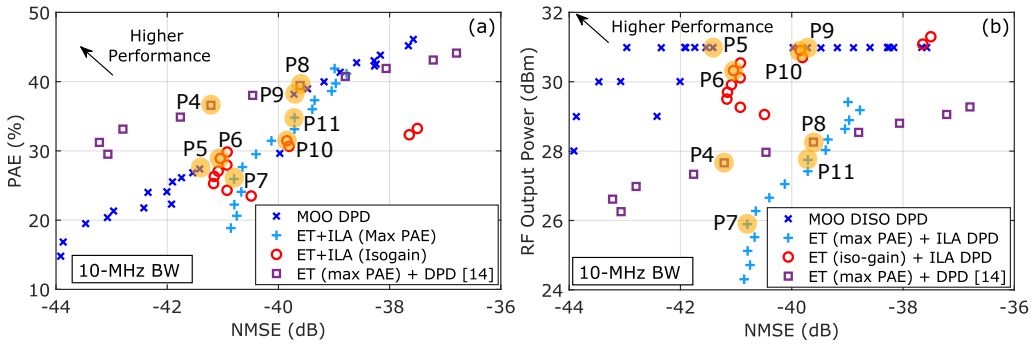

Figure 3.10: MOO-based Pareto front for maximum PAE and constrained NMSE using a static ST (dark blue x), compared with the standard iso-gain ST (@ 12.5 dB) with SISO DPD (red circles) and maximum PAE ST with SISO DPD (light blue +). The DPD complexity used is higher than the one in Fig. 3.9 (see Table 3.1). The test signal is a 10-MHz random-phase 1k-tone with PAPR = 9.3 dB.

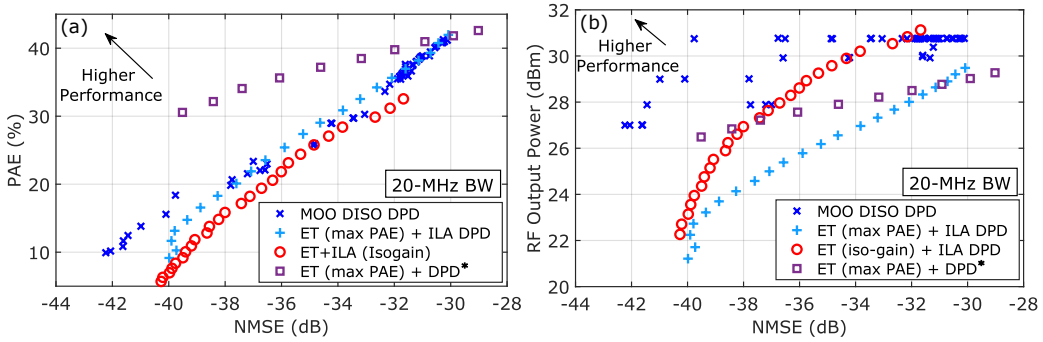

Figure 3.11: MOO-based Pareto front for maximum PAE and constrained NMSE using a static ST (dark blue x), compared with the approach in [3] (purple squares), the standard iso-gain ST (@ 12.5 dB) with SISO DPD (red circles), and maximum PAE ST with SISO DPD (light blue +). The test signal is a 20-MHz random-phase 2k-tone with PAPR = 10.11 dB.

tion coefficients, representing a distinctive optimal trade-off among various Figures of Merit (FoMs). This is achieved by varying the constrained NMSE from -40 dB to -30 dB for the SuMo. However, the SuMo inherently contains modeling errors, quantifiable in approximately 5 dB of difference between

the modeled and actual measured NMSE values (Fig. 3.9 underscore this difference). This discrepancy is as an intrinsic lower limit to the MOO linearization capabilities, and a maximum of 14 iterations is set as the stopping criterion for this work.

The performance of the MOO joint RF/LF DPD identification method is compared with those obtained by employing traditional shaping strategies coupled with standard SISO DPD, as introduced in Sec. 3.4. To ensure a fair comparison, the same DPD model orders as the MOO case are adopted. The LF/RF control laws for each of the compared methods are then tested using a different realization of the same random-phase multitone signal used in the identification phase. Specifically, we consider the ST for maximum PAE (light blue curve + in Fig. 3.9a) and for iso-gain (red circles in Fig. 3.9a) at different G_{lin}, resulting in distinct RF P_{out} levels as reported in Fig. 3.9b. Experimental results clearly demonstrate that the ST combined with the RF DPD, both automatically determined by MOO, enables the linearization of the PA in a more power-efficient operating point compared to the classical SISO DPD approach, resulting in up to approximately 56% PAE in combination with RF P_{out} of $\simeq 32$ dBm and NMSE of -34.5 dB (P1 in Fig. 3.9). Conversely, the traditional iso-gain (12.5 dB) configuration provides slightly superior linearity and P_{out} but significantly reduced PAE (P2 in Fig. 3.9), while the ST for maximum PAE achieves a maximum of approximately 51% PAE but at a much lower linearity and RF P_{out} (P3 in Fig. 3.9). The comprehensive performance metrics for these points of interest are reported in Table 3.1.

The superior performance of the proposed joint DPD-SM approach, outperforming traditional methods in terms of output power, PAE, or both, with the given DPD model complexity, can be attributed to the MOO algorithm ability to fully exploit the specified maximum NMSE level. It can automatically opt to sacrifice linearity (up to the imposed constraint) to enhance other metrics. In contrast, the iso-gain and maximum PAE approaches predefine the ST coefficients and subsequently identify suitable DPD coefficients to

Point	PAE (%)	RF out (dBm)	NMSE (dB)	ACPR (dB)	# RF coeff.	# LF coeff.
P1	**56.2**	**32.0**	**-34.5**	**-44.7**	**15**	**6**
P2	41.5	32.8	-35.9	-48.5	15	6
P3	51.1	30.3	-28.7	-38.8	15	6
P4	36.5	27.6	-41.2	-52.6	48	6
P5	**27.4**	**31.0**	**-41.4**	**-55.3**	**24**	**6**
P6	28.9	30.3	-41.0	-53.9	24	6
P7	25.9	25.9	-40.8	-53.4	24	6
P8	39.4	28.2	-39.6	-50.2	48	6
P9	**38.1**	**31.0**	**-39.7**	**-49.1**	**24**	**6**
P10	31.4	30.9	-39.8	-53.1	24	6
P11	34.8	27.7	-39.7	-52.3	24	6
P20	58.1	32.0	-34.1	-45.5	15	16
P21	52.5	30.5	-34.7	-47.3	15	16

Table 3.1: Operating points for a 10-MHz OFDM-like RF input (Figs. 3.9, 3.10, 3.12).

Point	PAE (%)	RF out (dBm)	NMSE (dB)	ACPR (dB)	# RF coeff.	# LF coeff.
P12	30.5	26.4	-39.5	-48.3	48	6
P13	**18.4**	**30.6**	**-39.8**	**-47.0**	**24**	**6**
P14	14.7	23.2	-39.3	-50.2	24	6
P15	10.9	25.1	-39.2	-49.6	24	6
P16	35.6	27.5	-36.1	-44.8	48	6
P17	**23.0**	**30.7**	**-36.5**	**-43.3**	**24**	**6**
P18	21.8	28.6	-36.0	-45.9	24	6
P19	25.4	25.7	-35.8	-45.8	24	6

Table 3.2: Operating points for a 20-MHz OFDM-like RF input (Fig. 3.11).

maximize linearity. For the considered DPD complexity level, the number of available RF DPD coefficients might be insufficient to effectively linearize

the maximum PAE and iso-gain cases.

To further investigate this behavior, the previous analysis was repeated under similar experimental conditions, with an increase in RF DPD MP orders to $M_\rho = 3$ and $K_\rho = 8$ (24 complex coefficients). In all cases, the LF STs were maintained with $M_\lambda = 0$ and $K_\lambda = 5$. Accordingly, the SuMo complexity for the MOO DPD case was slightly increased to $K_\sigma = K_\delta = 8$, while keeping $M_\sigma = M_\delta = 3$. When employing a higher-order DPD, the SuMo needs to offer correspondingly improved prediction capabilities. The results are depicted in Fig. 3.10. As anticipated, the resultant Pareto fronts generally show lower NMSE values. Unlike the lower DPD complexity case, the MOO DISO DPD exhibits PAE values similar to those seen for the maximum PAE and iso-gain cases, along with comparable NMSE values. This convergence among different strategies suggests that the increased RF DPD order is sufficient to ensure optimal linearity and efficiency in all cases. However, for similar NMSE and PAE values, the proposed MOO method achieves a significantly higher RF output power ($\sim 2-4$ dB) than classical STs, particularly in the high linearity region of the Pareto front.

Additionally, the model introduced in [3], already presented in Sec. 3.1, was included for comparison. To implement this method, the RF predistorter was enhanced by explicitly incorporating the dependency on the supply voltage modulated using the maximum PAE ST, as illustrated in Fig. 3.7. To accommodate the non-ideal supply and its interdependency with the PA, the model was fitted using the dynamic supply voltage measured at the PA terminal, not the supply control generated by the AWG on the LF path, as done for the other approaches. Moreover, the resulting DPD for the RF branch employs twice the number of coefficients compared to the other methods to achieve similar linearity. While this approach yields the highest PAE among all methods, it exhibits significantly lower output power than the MOO case for corresponding NMSE values, constrained by the use of the a-priori maximum PAE ST. Overall, the implementation requirement of a larger number of DPD coefficients and explicit knowledge of the measured supply voltage

prevents a straightforward comparison with the other examined methods.

In summary, eight landmark points (P4-P11 in Fig. 3.10), two for each of the four different DPD-SM strategies at NMSE levels of $\simeq -41$ and $\simeq -40$ dB, are reported for comparison in Table 3.1, along with the corresponding RF/LF DPD complexity orders.

The previous analysis was then replicated, maintaining the same DPD and ST orders, using a 20-MHz-wide random-phase multi-tone signal with PAPR = 10.1 dB. Similar trends were observed, albeit with lower average output power and PAE values. The PAE-NMSE Pareto front closely resembled that between the MOO, iso-gain, and maximum PAE cases. In contrast, the predistorted model from [3] with the maximum PAE ST exhibited significantly higher PAE. The MOO DPD, however, displayed significantly higher output power than all other cases. For this test, another eight landmark points (P12-P19), two for each of the four different RF/LF DPD strategies at NMSE levels of $\simeq -40$ and $\simeq -36$ dB, are reported in Table 3.2.

3.6.2 MOO-based joint LF/RF Digital Predistortion

In the case of a 10 MHz bandwidth, the MOO technique was evaluated by incorporating a memory depth of $M_\lambda = 2$ into the LF predistorter. It has been tested that no superior performance could be achieved with higher M_λ values. This configuration unlocks dynamic LF supply shaping, a design and identification approach that is not obtainable with standard SM techniques. The predistorter orders for the remaining LF/RF are maintained as shown in Fig. 3.9. Consequently, the total number of optimized variables increases to 46: 15 complex coefficients for the RF predistorter and 16 real coefficients for the LF predistorter.

The resulting maximal points on the Pareto plots for $P_{\text{out}} \simeq 32$ dBm are illustrated in Figure 3.12. Specifically, operating point P20 is identified as the optimal trade-off between linearity (NMSE < -34 dB) and PAE ($\simeq 58\%$), outperforming the P1 operating point described in Sec. 3.6.1 (also shown in Fig. 3.12). The MOO algorithm was also applied with a lower G_{lin},

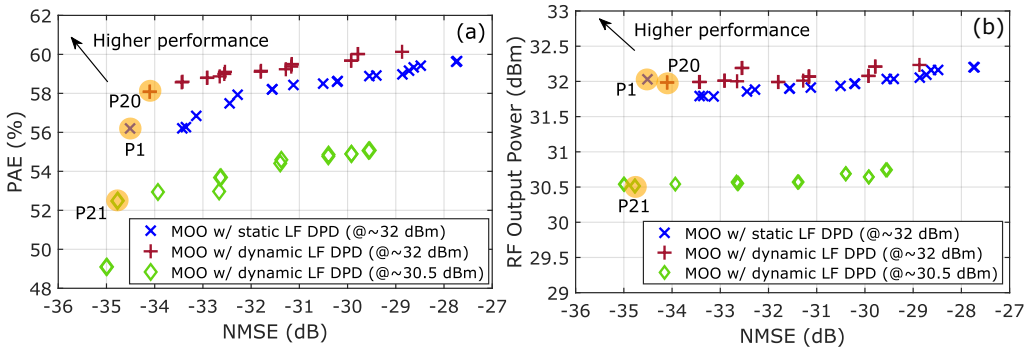

Figure 3.12: Comparison among the PAE/NMSE (a) and RF output power/NMSE (b) Pareto fronts obtained by the MOO algorithm by maximizing PAE under constrained NMSE and fixed linearization gain. Three cases are reported: static LF predistorter (blue crosses), LF predistorter with memory (red pluses), LF predistorter with memory at a lower RF output power level.

corresponding to $P_{\text{out}} \simeq 30.5$ dBm, to empirically test the achievability of higher linearity levels by reducing the average output power [61]. The resulting Pareto front and representative point P21 are depicted in Fig. 3.12. As expected, this case exhibits reduced P_{out} compared to the previous cases with higher G_{lin}. However, this reduction in performance is not proportionally matched by an increase in linearity, and the PAE is decreased by $\simeq$ 5%. This underscores the complex trade-off profile between the Figures of Merit (FoMs), which can be automatically explored using the proposed MOO framework.

The supply control functions obtained for the MOO-based analyzed cases are presented in Figure 3.13. The MOO procedure results at points P1 (MOO static supply shaping, P_{out}=32 dBm), P20 (MOO dynamic supply shaping, P_{out}=32 dBm), and P21 (MOO dynamic supply shaping, P_{out}=30.5 dBm) from Fig. 3.12 are compared with the traditional iso-gain (12.5 dB) and maximum PAE static supply STs introduced in Sec. 3.4. It is evident that the optimal static ST identified by MOO, offering significant global performance improvement over the classical cases of P2 and P3 (Table 3.1), is

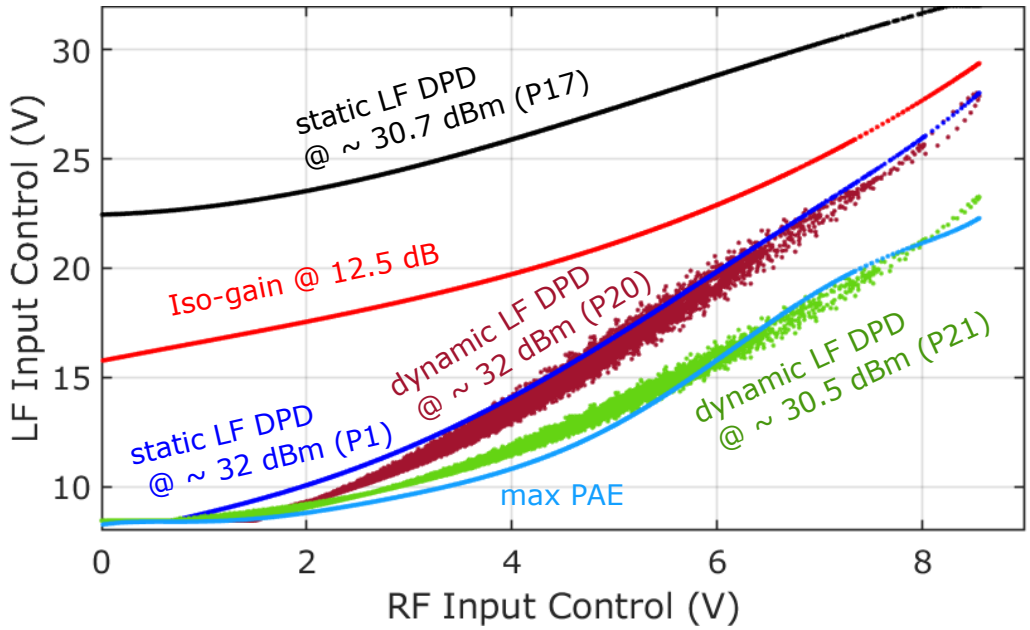

Figure 3.13: Different supply control functions obtained with the MOO (dark red, black, blue, and green curves) compared to the classical shaping tables from the static PA analysis (red and light blue lines). The RF input power ranges from 2.6 dBm to 28.6 dBm (shown in linear scale on the x-axis).

positioned below the iso-gain ST but above the maximum PAE one. Although the overall qualitative behavior is similar across different cases, the specific best operating point could not be deduced from the static characterizations in Sec. 3.4, demonstrating MOO unique capability in accounting for RF DPD. Importantly, MOO is not in principle restricted to classical ET or polar PA behavior and may result in a favorable hybrid form between the two, depending on the characteristic of the PA under study. The introduction of LF dynamics ($M_\lambda = 2$) introduces hysteresis in the characteristic, indicating that the relationship between RF input and supply control cannot be described using a simple look-up table in this case.

Figure 3.13 also presents the ST resulting from the operating point P17 previously shown in Fig. 3.11 and Table 3.2, which is substantially different from the previous ones. This emphasizes that, unlike classical a-priori

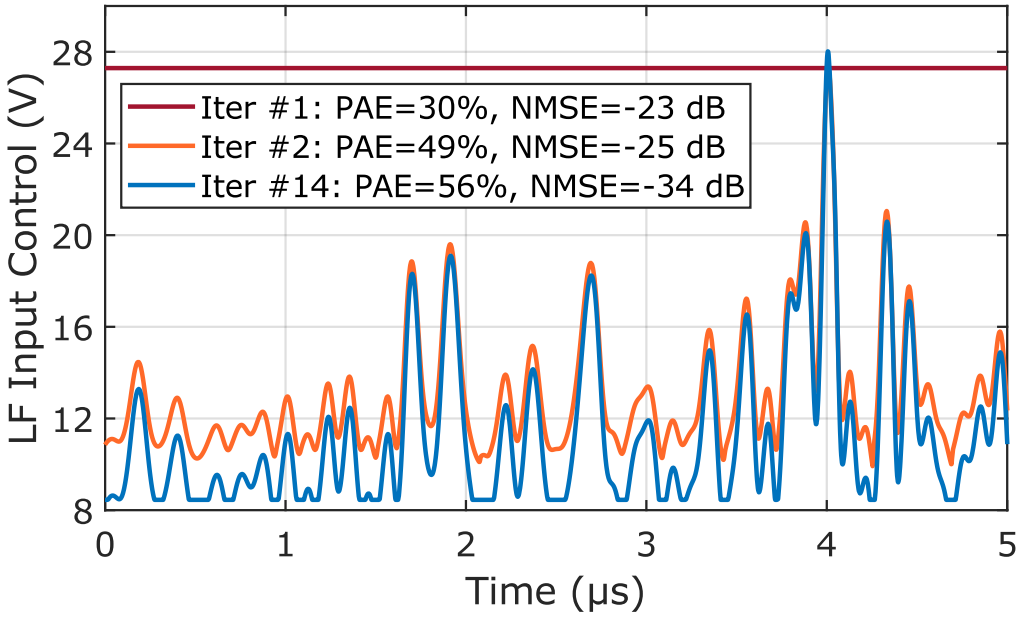

Figure 3.14: Time frame of the LF input control waveform at different iterations, corresponding to the operating point P1 in Fig. 3.9. The test signal is a 10-MHz random-phase 1k-tone with PAPR = 9.5 dB.

STs, the MOO-based technique automatically identifies the most suitable supply control based on the specific operating point at a different excitation bandwidth (BW).

3.6.3 Iterative behavior

Illustrated in Figs. 3.14- 3.15, an instance of the iterative behavior of the constrained MOO algorithm is provided for the P1 operating point (refer to Fig. 3.12 and Table 3.1). As it can be noticed, the method is able to steer towards a better linearity performance already from the very first iteration. Concurrently, the MOO algorithm automatically reaches an optimized SM starting from a fixed supply of 28 V (Fig. 3.14). Consequently, for the supply control, the optimizer imposes a significant reduction in drain voltage already in the initial iterations, thereby increasing the PAE.

The complete iterative values for PAE and NMSE are depicted in Fig. 3.15.

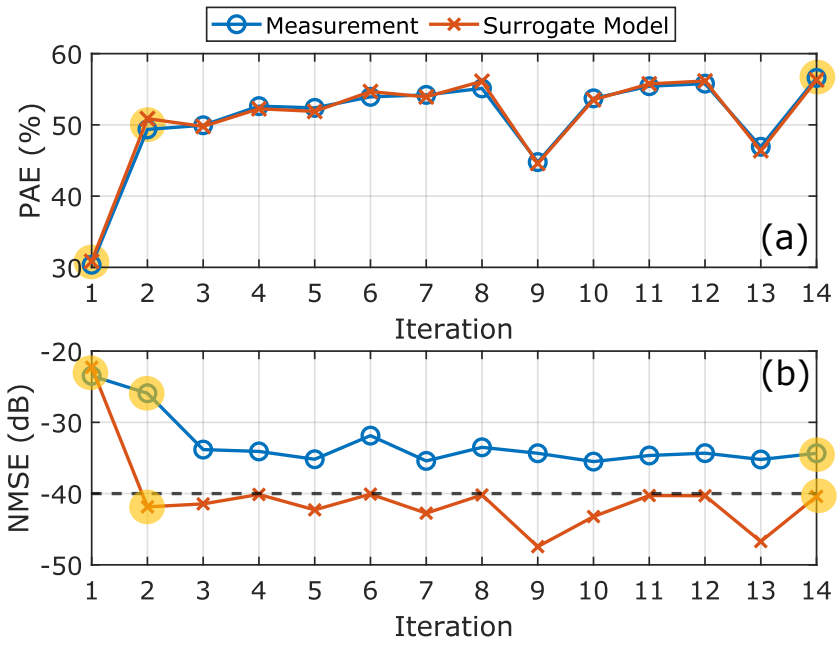

Figure 3.15: MOO iterative behaviour corresponding to the non-dominated solution P1 in Fig. 3.9. The values of (a) PAE and NMSE (b) at each iteration for the SuMo (red) and the measured PA (blue) are compared. Black dashed line in (b) identifies the level of the fixed linearity constraint.

As the successive iterations are computed, the performance exhibits minimal oscillations across the constraint, eventually stabilizing around the joint optimum. Fig. 3.15 also illustrates the actual discrepancy between the measurement and the adopted MP-based SuMo prediction. Specifically, for the adopted SuMO formulation and choice of iterative extraction dataset(s) $\mathcal{D}^{(i)}$, such a deviation in the prediction is already reached within very few iterations. This residual deviation constitutes a lower limit for the MOO linearization capabilities. However, depending on the actual application (e.g., different signal characteristics), more tailored modeling representations could indeed be adopted within the same MOO framework. Conversely, the PAE does not depend as strongly as the NMSE on the model, and an error of just a few percentage points for the PAE (as typically accepted) could be easily reached with the adopted SuMo, hence the good performance pre-

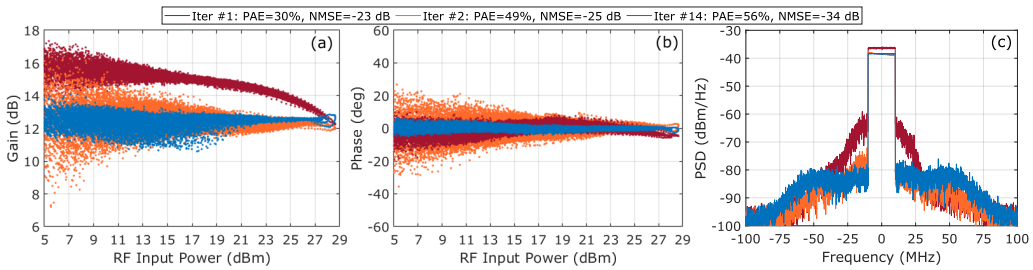

Figure 3.16: (a) AM/AM characteristics, (b) AM/PM characteristics, and (c) RF output spectra at different iterations. The test signal is a 10-MHz random-phase 1k-tone with PAPR = 9.5 dB.

diction throughout the iterations. In this context, Fig. 3.16 shows the dynamic AM/AM and AM/PM characteristics of the PA together with the (linearized) output spectra for three selected iteration points that are highlighted in Fig. 3.15.

Figs. 3.17a-c display the dynamic gain and AM/PM characteristics of the PA along with the power spectra at the first (non-predistorted conditions at fixed supply 28 V and 3-dB compression) and last iteration for the operating point P9 with BW=10 MHz (refer to Fig. 3.10 and Table 3.1). The same plots are also presented for operating point P13 with BW=20 MHz in Figs. 3.17d-f (refer to Fig. 3.11 and Table 3.2). It is important to emphasize that both operating regimes are suitable non-dominated trade-offs among PAE, RF output power, DPD complexity, and resulting linearity. Hence, they do not represent the maximum level of linearity that could be reached for this PA.

3.7 Comments on the Residual Distortion

Considering Fig. 3.16a, the AM/AM figure still show a lot of memory effects and the spectra plot also indicates there are some remaining distortions. With respect to this measured residual distortion of the SM-PA, it is worth highlighting the specific configuration of the GaN-based PA here here in use: the largest supply capacitors of 33 μF, 1 μF, and 33 nF have been

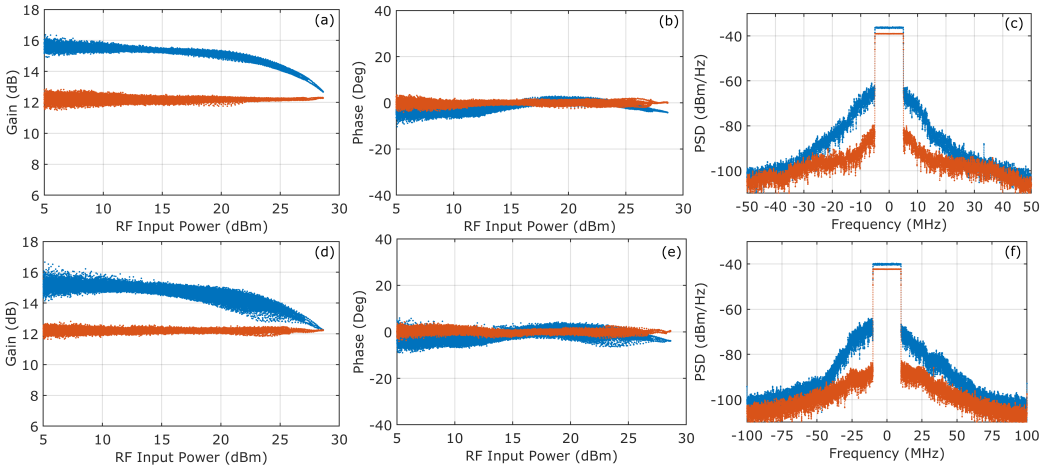

Figure 3.17: (a,d) Gain characteristics, (b,e) AM/PM characteristics, and (c,f) RF output spectra for two examples of non-dominated operating points (blue: initial conditions; red: last iteration). Operating point P9 in Table 3.1 (10-MHz OFDM-like signal with PAPR=9.5 dB: PAE=38.1%, RF P_{out}=31.0 dBm, NMSE=-39.7 dB) in top row; Operating point P13 in Table 3.2 (20-MHz OFDM-like signal with PAPR=10.1 dB: PAE=18.4%, RF P_{out}=30.6 dBm, NMSE=-39.8 dB) in bottom row.

removed from the original evaluation board. Additionally, ADA4870 supply modulator, which has a non-zero output resistor, and the sensing setup at the supply terminal with the current clamp probe, which introduces a non-negligible parasitic inductance, should be noted. This specific hardware setting implies different from the typical hardware implementation of the PA and, possibly, leads a lower absolute performance. For this reason, the actual behavior of the PA cannot be easily compared with the nominal performance from the datasheet.

In order to better compare the performance of the SM-PA, Figure 3.18a-f provides an example of gain and AM/PM, and spectrum in the case of fixed supply (28V supply). The blue curves represent the PA distorted output at $\simeq 3dB$ compression for a 10MHz-bandwidth (Figs. 3.18a-c) and for a 20MHz-bandwidth input signal (Figs. 3.18d-f). The red curves show the linearized

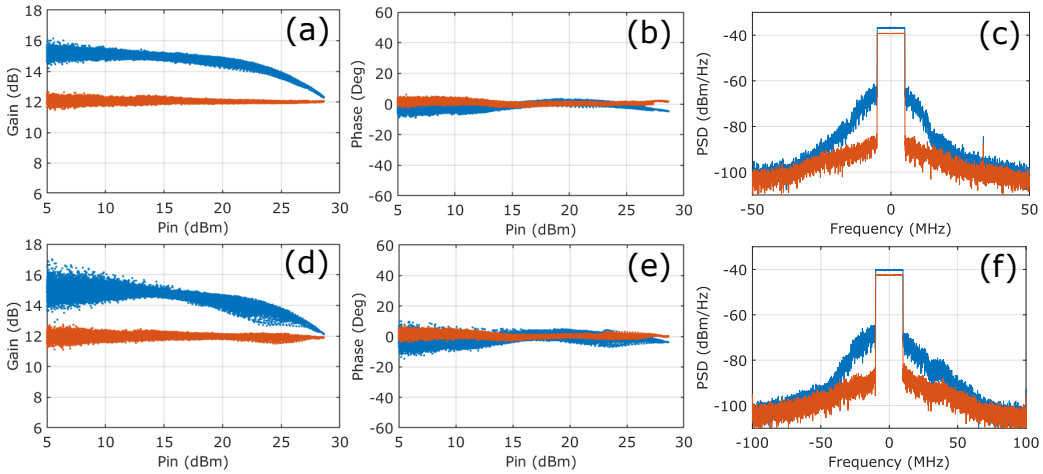

Figure 3.18: (a,d) Gain characteristics, (b,e) AM/PM characteristics, and (c,f) RF output spectra before and after ILA DPD at constant 28V supply. (10-MHz OFDM-like signal with PAPR=9.5 dB: PAE=18.0%, RF P_{out}=31.8 dBm, NMSE=-40.4 dB) in top row; (20-MHz OFDM-like signal with PAPR=10.1 dB: PAE=17.0%, RF P_{out}=30.9 dBm, NMSE=-38.4 dB) in bottom row.

output applying an ILA DPD to the fixed supply PA (28V supply). Finally, it is possible to note that in Figs. 3.17a-f the blue curves are the same of Figs. 3.18d-f), since the starting point of the MOO correspond to the non-predistorted condition at fixed supply.

3.8 Achievements

This work introduces a novel framework for the generalized DPD of MISO PA architectures, specifically demonstrated for SM-PAs. The proposed surrogate-based MOO technique automates the exploration of the trade-off between linearity and efficiency, enabling joint control of the RF input and SM.

Furthermore, the framework facilitates the implementation of a generalized dynamic DPD on the SM, as opposed to the static ST, and inherently

considers the input signal statistics. The resulting operating regimes outperform classical methods for STs not only in terms of the optimized FoM, i.e., PAE, but also in terms of linearity for a given RF output power (P_{out}).

The feasibility of the method and the actual optimum achieved are, however, constrained by the fidelity of the SuMo. While this work employs a dual-input MP formulation, more accurate modeling approaches could be chosen depending on the application, reducing the discrepancy between simulations and measurements and enhancing optimization reliability.

Chapter 4

Simulation-based optimization of the DIDPA

4.1 Introduction

This chapter summarizes the findings published in [91], which is a preliminary simulation-based work aimed at implementing and comparing optimization strategies to achieve optimal input splitting and biasing of a dual-input Doherty power amplifier (DIDPA) under high peak-to-average power ratio (PAPR) modulation. The DIDPA is designed using state-of-the-art 150 nm gallium nitride (GaN) on silicon carbide (SiC) Monolithic Microwave Integrated Circuit (MMIC) technology. The designed DIDPA operates at a center frequency of 24 GHz, targeting applications in the 5G Frequency Range 2 (FR2). Following the formulation of the DIDPA optimization problem in this Chapter, a series of simulation-based experiments will be employed for evaluating various optimization approaches.

Section 4.2 explores single-objective optimization utilizing the coordinate descent algorithm. This method iteratively considers pairs of input variables to maximize Power Added Efficiency (PAE). A second methodological strategy employs a *Bayesian* framework, implementing both a single-objective optimization (Section 4.3) and a comprehensive multi-objective optimization

(MOO) in Section 4.4. In the latter, both PAE and Radio Frequency (RF) output power serve as joint target figures of merit (FoMs), leading to the derivation of a Pareto frontier representing non-dominated solutions. These solutions correspond to sets of input variables where improvements in either PAE or RF output power are unattainable without compromising the other. Section 4.5 discusses and evaluates the performance of the PA optimal configurations derived from the distinct optimization frameworks under high-PAPR wideband-modulated signal excitation.

4.1.1 DIDPA Design

The DIDPA here under analysis was previously designed by the EDM-LAB research group at the University of Bologna. The adopted process was the Win Semiconductors NP15-00 150 nm GaN manufactured on 100 mm SiC wafers. This process is well suited for mm-wave high-power applications featuring $f_t = 34.5$ GHz. The breakdown voltage exceeds 100 V thanks to a source-coupled field plate. At 20 V operation, the maximum power density is 4 W/mm at 29 GHz. This work focus on the optimization of the device that followed the design phase, which is not part of the thesis. The DIDPA block diagram is shown in Fig. 4.1, while its layout is shown in Fig. 4.2. A two-stage amplification is used to target 25 dB of gain at 24 GHz. The devices of the driving stage are 2×75 μm HEMTs whereas, in the final stage, 6×75 μm HEMTs were used both for the main and the auxiliary PAs. The nominal drain voltage is $V_D = 20$ V for all the stages. In Fig. 4.2, it is possible to visualize the asymmetry of the output combiner that provides the required 90-degree phase shift in the combination of the output signals. The chip dimensions are 3.8 mm $\times$ 4.2 mm.

The performance of the DIDPA enforcing the nominal input split and bias by applying the values from Tab. 4.1 is shown in Fig. 4.3a,b, which respectively display the S-parameters and the continuous-wave (CW) large-signal characteristics. With a peak PAE of 40% and PAE of 30% at 6 dB of output backoff, the performance of the presented PA is in line with similar K-

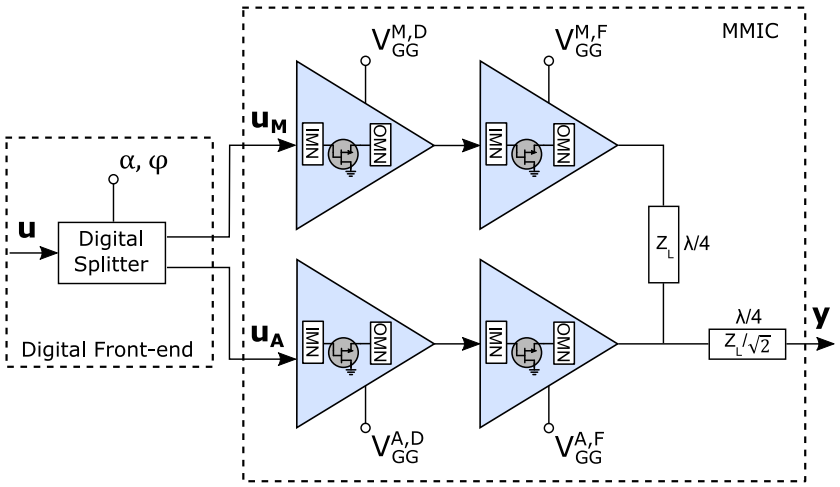

Figure 4.1: Block diagram of the DIDPA schematic with explicit labeling of the optimization variables (α, ϕ, $V_{GG}^{M,D}$, $V_{GG}^{M,F}$, $V_{GG}^{A,D}$, and $V_{GG}^{A,F}$), the main and auxiliary branch RF inputs (respectively, $\mathbf{u}_M$ and $\mathbf{u}_A$), and the RF output ($\mathbf{y}$). The block diagram highlights the two-stage DIDPA with the input and output matching networks of each stage, and the quarter-wave output combiner.

band high-gain (two-stage) DPAs found in the literature, e.g., [92–94]. The nominal input split and bias are extracted in the design phase in order to implement a classical single-input DPA: class C bias for the peaking amplifier, class AB for the main amplifier, and the optimal input split for this bias configuration.

4.1.2 Optimization Problem

The pursuit of an optimal set of input variables to achieve peak Power Amplifier (PA) performance can be characterized as a Multi-Objective Optimization (MOO) problem. Here, the control inputs form a set $\mathbf{x}$ of variables, while the PA performance is assessed by multiple scalar FoMs, such as output power, PAE, and gain. These FoMs represent the diverse objectives of the problem, with the goal of maximizing (or equivalently minimizing) them. The definition of the variables $\mathbf{x}$ is contingent upon the specific PA topol-

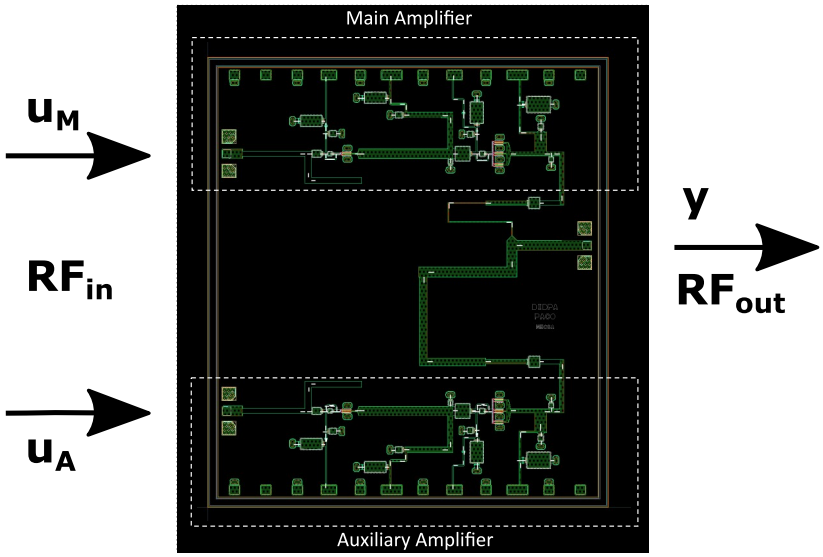

Figure 4.2: Layout of the simulated DIDPA MMIC with labeling of the main and auxiliary branch RF inputs (respectively, $\mathbf{u}_M$ and $\mathbf{u}_A$), and the RF output ($\mathbf{y}$).

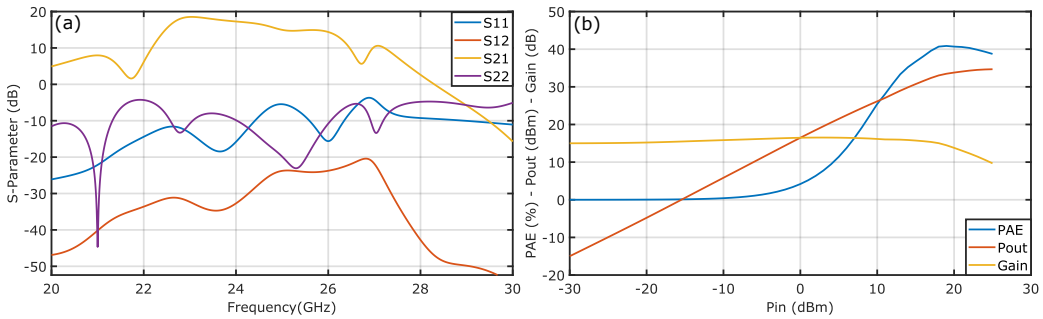

Figure 4.3: (**a**) *S*-parameters and (**b**) CW large-signal characteristic of the DIDPA when the nominal bias and input splitting are applied.

ogy being investigated. If considering to apply an optimization framework to outphasing PAs, it may involve the amplitude/phase split of the inputs, while in Load-Modulated Balanced Amplifiers (LMBAs), it may encompass parameters like injection ratio and input-referred phase displacement [95].

In the case of a Dual-Input Doherty Power Amplifier (DIDPA), as depicted in Fig. 4.1, effective optimization variables include the parameters

α	ϕ **(deg)**	$\mathbf{V_{GG}^{M,D}}$ **(V)**	$\mathbf{V_{GG}^{M,F}}$ **(V)**	$\mathbf{V_{GG}^{A,D}}$ **(V)**	$\mathbf{V_{GG}^{A,F}}$ **(V)**
0.5	-90	-1.7	-1.7	-2.3	-2.1

Table 4.1: Nominal values of the parameters considered for DIDPA optimization.

of the input splitter, specifically the amplitude ratio α and the phase displacement ϕ between the two split signals [44]. Additionally, the DIDPA behavior is significantly influenced by the biasing voltages across all stages, determining the amplitude level at which the peaking amplifier impacts the main amplifier and vice versa. Consequently, it is logical to consider all bias voltage values as optimization variables. In this Chapter, the focus is on gate bias voltages for the driver and the final PA of each DPA branch, namely for the main PA ($V_{GG}^{M,D}$ and $V_{GG}^{M,F}$, respectively) and for the auxiliary PA ($V_{GG}^{A,D}$ and $V_{GG}^{A,F}$, respectively). The six real variables considered, along with their nominal values established in the design phase (before any optimization), are detailed in Tab. 4.1.

The performance of the DIDPA can be evaluated through different FOMs, depending on the final application. The DIDPA here under analysis is designed targeting wideband communication signals, so it should be assessed in terms of the compromise among PAE, RF output power, and linearity when excited with suitable modulated signals. More precisely, the FoMs to be optimized are here embodied by the following performance quantities:

$$\begin{aligned} \text{PAE}\ (\%) &= \frac{P_{out}^{RF} - P_{in}^{RF}}{P_{dc}}; \qquad P_{out}^{RF}\ (\text{W}) = \frac{1}{2NR_{out}} \sum_{n=0}^{N-1} |y_n|^2; \\ \text{NMSE}\ (\text{dB}) &= 10 \log_{10} \frac{\sum_{n=0}^{N-1} |y_n - G_{\text{lin}} u_n|^2}{\sum_{n=0}^{N-1} |G_{\text{lin}} u_n|^2}; \end{aligned} \tag{4.1}$$

where P_{dc} is the total power absorbed from the DC supply, P_{in}^{RF} is the sum of the RMS injected power at RF at the two inputs, $R_{out} = 50\ \Omega$ is the output resistance, u_n and y_n are, respectively, the complex envelope samples of the input (before digital split) and output signals, N is the number of time-domain signal samples, and G_{lin} is the desired linear gain for the device. It is

crucial to acknowledge that the functional relationships underlying the FoMs in (4.1) are typically not explicitly known in a mathematical formulation, as they rely on complex nonlinear interactions within the Power Amplifier (PA). Consequently, solving the optimization problem in a closed form is usually impractical. Conversely, the FoMs in (4.1) can be obtained through direct evaluation of the PA response for a given set of input parameters, facilitated by simulation- or measurement-based experiments.

An intuitive approach for identifying the maximum (or minimum) of an objective function $g(\mathbf{x})$, describing a specific FoM without making assumptions about the function characteristics (e.g., convexity), involves sweeping all variables (factorial sweep) across appropriate value ranges. These ranges can be defined for the DIDPA variables in Tab. 4.1, specifically $\alpha \in [0, 1]$, $\phi \in [-180, 180]$ (deg), with the remaining four bias voltage variables having limited ranges to adhere to the safe operating area of the transistors. However, the need for suitable resolution and the high dimensionality of the problem makes a full factorial sweep impractical. For instance, a uniform factorial sweep would demand r^6 FoM evaluations, with r representing the a fixed number of evaluation points for each dimension. This easily leads to several hundred-thousand FoM evaluations, which are clearly impractical in simulation- or measurement-based experiments.

Although there are suitable experimental designs for efficient exploration of the space of the variables [58], they would still require an excessively large number of evaluations for the specific application under consideration, without guaranteeing the detection of actual optima. Other optimization approaches available in the literature [96] rely on iterative algorithms, such as calculating numerical gradients of objectives and constraints at each iteration. Gradient-based optimizers may be more efficient in determining the optimal direction and might be considered as an effective tool for DIDPA optimization [74], but are considered impractical due to the number of evaluations needed, proportional to the number of optimization variables (six in this case).

4.1.3 Quasi-Static Surrogate Modeling

Beyond the considerations above, the evaluation of a PA FoM, i.e., of the objective function $g(\mathbf{x})$ can be particularly time consuming for orthogonal-frequency-division-multiplexing (OFDM) modulations involving a large number of carriers and long signal frames, as adopted in modern high-data-rate telecommunication standards. In order to make optimization feasible, in [73] it was proposed to exploit surrogate models (SuMos) of the FoMs in (4.1), namely models that are fast in terms of extraction and evaluation, while also accurate enough to enhance convergence and steer the iterations towards the global optimum. Here, the same approach is followed by using multi-variable quasi-static AM/AM–AM/PM characteristics as the basis for DIDPA surrogate modeling. Such a surrogate description can jointly handle the six considered variables, and can be straightforwardly and efficiently evaluated by standard CW single-tone experiments.

To calculate FoM prediction in the presence of modulated signals from the quasi-static model (QSM), the DIDPA quasi-static CW characteristics should be weighted by the probability density function (PDF) of the stationary stochastic process corresponding to the excitation signal class of interest [89, 97]. In the case under consideration, the class of OFDM-modulated signals asymptotically corresponds to a Gaussian complex envelope [27], thus to a signal amplitude matching a Rayleigh distribution, as discussed in Sec.1.2. Therefore, the RF output power (P_{out}^{RF}) and the PAE can be written as follows:

$$P_{out}^{RF} = \int_0^{+\infty} P_{out}^{pdf}(p)dp; \quad \text{PAE} = \frac{\int_0^{+\infty} P_{out}^{pdf}(p)dp - \int_0^{+\infty} \widehat{P}_{in}(p)P_{out}^{pdf}(p)dp}{\int_0^{+\infty} \widehat{P}_{dc}(p)P_{out}^{pdf}(p)dp}; \tag{4.2}$$

where $P_{out}^{pdf}(p)$ is the probability density function of the desired output-modulated signal, $\widehat{P}_{in}(p)$ is the static relationship between the output p and the input $\widehat{P}_{in}$ power of the DIDPA, and $\widehat{P}_{dc}(p)$ is the static relationship between the output p and the absorbed power at DC. Calculating FoMs with Eq. 4.2 is conceptually equivalent to exciting the QSM with a modulated

signal. While such a QSM representation might be suboptimal for wideband signals, it will be shown that for the case under examination it provides sufficient ability to sort out the main interdependencies among the input variables and it proves effective for the optimization. The actual DIDPA broadband behavior can always be checked with a final experimental assessment under a wideband signal excitation. In this context, the aim is to see the FoMs calculated with the PDF-based SuMo in Eq. 4.2 converge to the values calculated under a wideband signal excitation in (4.1).

The choice of the optimization algorithm is critical as it determines the number of iterations and FoM evaluations needed to reach a solution, and the complexity involved becomes particularly high when considering multiple objectives. In this context, the RF output power and the PAE as defined in (4.2) will be used as the key FoMs to evaluate PA performance. Regarding linearity, let us exploit the adopted QSM representation considering that the typical AM/AM–AM/PM characteristics of a well-designed PA are monotonic and thus biunivocal, and hence analytically invertible [70, 73]. In other words, given a theoretically infinite complexity for the predistorter, the AM/AM–AM/PM characteristics can be exactly linearized, and hence always respect any required NMSE constraint.

Although the hypothesis of exact linearization (i.e., resulting in infinite DPD complexity) is clearly unrealistic, non-parametric DPD methods like Iterative Learning Control (ILC) [75] allow to find the ideal predistorted waveform (up to the numeric precision) for a given PA regime. While the actual parametric predistorter implementation (with a finite set of DPD coefficients) will clearly entail higher NMSEs, DPD complexity nowadays available in hardware for communications applications can typically accommodate sufficient linearization performance. Therefore, the NMSE constraint will not be explicitly accounted for in the optimization methods described in Sections 4.2 and 4.3 to be applied to the quasi-static AM/AM–AM/PM model. The optima found with these methods will then be tested in Section 4.5 under wideband modulated excitation in order to validate this assumption.

α	ϕ (deg)	$\mathbf{V_{GG}^{M,D}}$ (V)	$\mathbf{V_{GG}^{M,F}}$ (V)	$\mathbf{V_{GG}^{A,D}}$ (V)	$\mathbf{V_{GG}^{A,F}}$ (V)
0.01	1	0.1	0.1	0.1	0.1

Table 4.2: Resolutions of the variables employed in the 2D factorial sweeps.

4.2 Coordinate Descent Optimization

The coordinate descent (CD) algorithm finds the local optimum of the target objective function $g(\mathbf{x})$ by successively solving a maximization (or minimization) problem along a limited set of coordinate directions. In practice, a subset of the six control variables $\mathbf{x}$ of the DIDPA is selected, and the optimum is searched across this subset while blocking the other variables to fixed values. The procedure is then repeated by cycling through the other subsets of variables, optimizing one subset at a time. This method allows for a reduction of FoM evaluations, as each of the iterations deals with a problem of lower dimensionality.

In particular, the six variables in Tab. 4.1 are divided into three subsets of two variables each, namely the splitting variables (α,ϕ), the biasing of the main PA ($V_{GG}^{M,D}$,$V_{GG}^{M,F}$), and the biasing of the auxiliary PA ($V_{GG}^{A,D}$,$V_{GG}^{A,F}$). This configuration makes it feasible to find the optimum across a 2D space by means of 2D factorial sweep with sufficient resolution (Tab. 4.2). Figure 4.4 reports an example of the 2D sweeps for each iteration, showing that the dependency of PAE on the variables is sufficiently regular in the application domain, allowing to easily select the maximum point at each cycle.

Figure 5.5 displays the flow chart for the CD algorithm applied to the quasi-static AM/AM–AM/PM model and aimed at the maximization of the PAE metric as defined in (4.2). In the depicted flow chart, the sequence and selection of variables for optimization is fixed in the order (α,ϕ) $\rightarrow$ ($V_{GG}^{A,D}$,$V_{GG}^{A,F}$) $\rightarrow$ ($V_{GG}^{M,D}$,$V_{GG}^{M,F}$). However, any other different permutation could be adopted (Tab. 4.3).

Firstly, the splitter parameters (α, ϕ) are swept while keeping the biasing parameters fixed at nominal values (Tab. 4.1) so as to identify a point

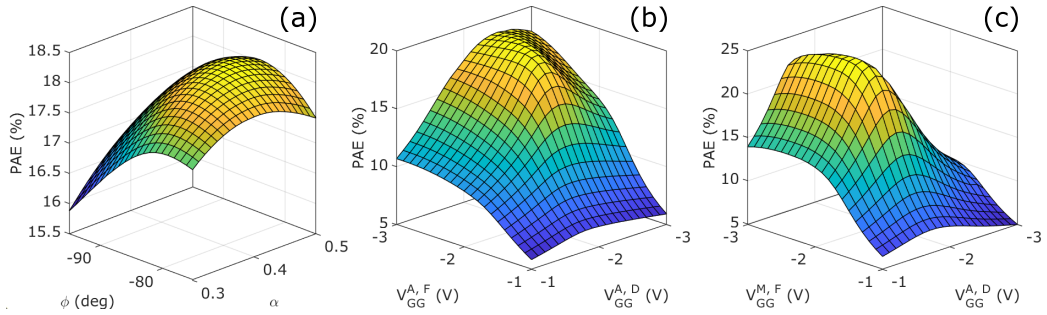

Figure 4.4: Example of 2D sweeps cyclically realized by the coordinate descent optimization of PAE for the DIDPA under study versus (**a**) input splitter parameters (α, ϕ), (**b**) auxiliary amplifier bias voltages ($V_{GG}^{A,D}$, $V_{GG}^{A,F}$), and (**c**) main amplifier bias voltages ($V_{GG}^{M,D}$, $V_{GG}^{M,F}$).

$(\alpha, \phi)_{\max}$ corresponding to the maximum PAE across the 2D domain defined by the splitter. Then, the same procedure is applied to the bias voltages of the auxiliary amplifier ($V_{GG}^{A,D}$, $V_{GG}^{A,F}$), while the splitter parameters are fixed at $(\alpha, \phi)_{\max}$. Once the point $(V_{GG}^{A,D}, V_{GG}^{A,F})_{\max}$ corresponding to the maximum PAE among the swept values has been identified, the same procedure is eventually repeated for the main amplifier bias voltages ($V_{GG}^{M,D}$, $V_{GG}^{M,F}$).

The adopted descent order may clearly have an impact on the optimum found by the algorithm. Thus, all the permutations have been tested, and the results after one iteration of the flow chart in Fig. 4.5 are reported in Tab. 4.3. The relatively small differences suggest that all orders identify a similar optimum, making CD a reliable solution for this optimization problem.

In addition, the same flow chart can also be iterated. Thus, as further tested, The order achieving the best PAE in the first iteration has been considered, namely ($V_{GG}^{M,D}$,$V_{GG}^{M,F}$) $\rightarrow$ ($V_{GG}^{A,D}$,$V_{GG}^{A,F}$) $\rightarrow$ (α,ϕ), and left it iterating until no incremental improvement could be seen between two successive iterations. Table 4.4 compares the results between the case with only one iteration and the iterative case (six iterations in total, with a proportional number of PAE evaluations involved), reporting only a small increment in

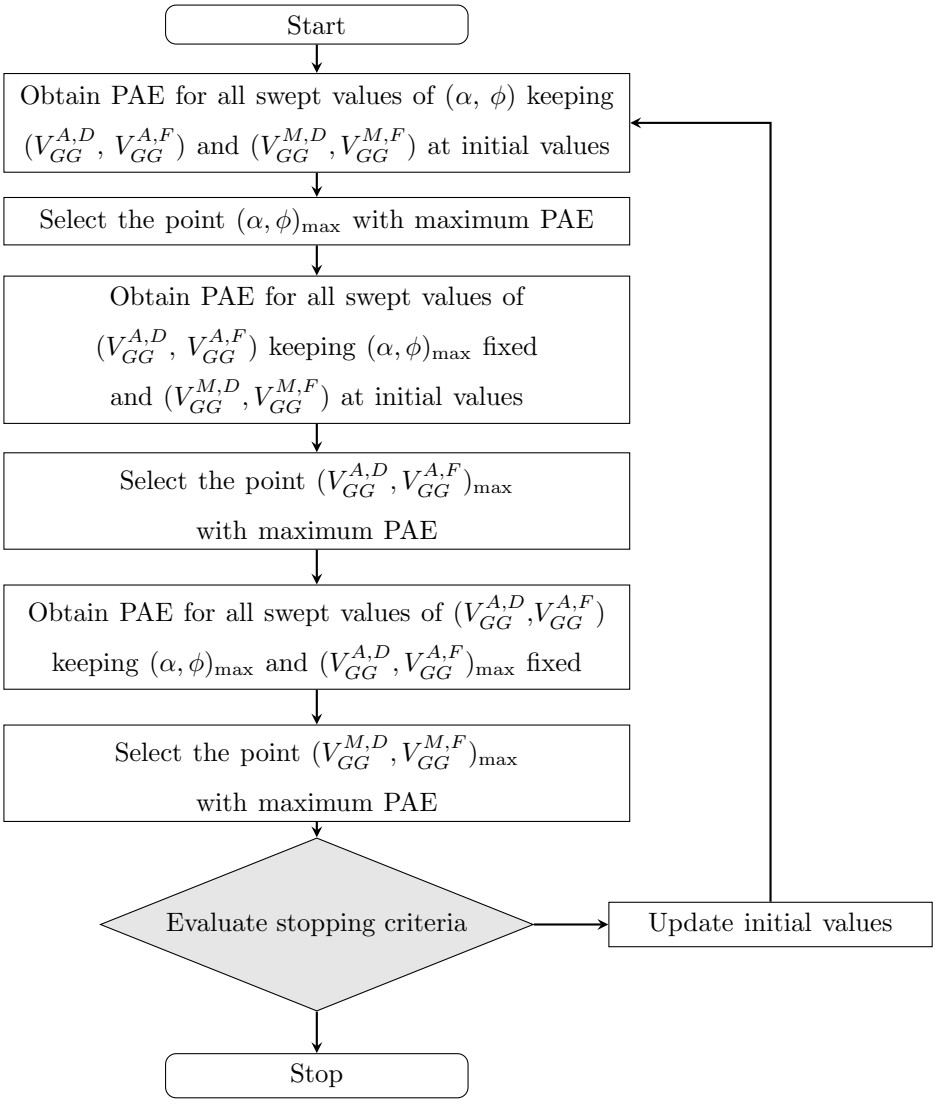

Figure 4.5: Flow chart for the coordinate descent optimization algorithm for the case of descent order $(\alpha,\phi) \rightarrow (V_{GG}^{A,D},V_{GG}^{A,F}) \rightarrow (V_{GG}^{M,D},V_{GG}^{M,F})$.

PAE. It is worth highlighting that the retrieval of the PAE value for a given set of input variables corresponds to the evaluation of the quasi-static PAE expression in (4.2), which is very quick in a classical PC simulation environment (in the order of a few seconds), thus making it feasible to realize the high number of PAE evaluations as the ones reported in Tab. 4.4.

Coordinate Descent Order	$\mathbf{P_{out}^{RF}}$ (dBm)	PAE (%)
$(\alpha,\phi) \rightarrow (V_{GG}^{A,D},V_{GG}^{A,F}) \rightarrow (V_{GG}^{M,D},V_{GG}^{M,F})$	24.0	24.5
$(\alpha,\phi) \rightarrow (V_{GG}^{M,D},V_{GG}^{M,F}) \rightarrow (V_{GG}^{A,D},V_{GG}^{A,F})$	23.9	24.1
$(V_{GG}^{M,D},V_{GG}^{M,F}) \rightarrow (\alpha,\phi) \rightarrow (V_{GG}^{A,D},V_{GG}^{A,F})$	24.2	24.3
$(V_{GG}^{A,D},V_{GG}^{A,F}) \rightarrow (V_{GG}^{M,D},V_{GG}^{M,F}) \rightarrow (\alpha,\phi)$	24.0	25.2
$(V_{GG}^{M,D},V_{GG}^{M,F}) \rightarrow (\alpha,\phi) \rightarrow (V_{GG}^{A,D},V_{GG}^{A,F})$	23.8	25.0
$(V_{GG}^{M,D},V_{GG}^{M,F}) \rightarrow (V_{GG}^{A,D},V_{GG}^{A,F}) \rightarrow (\alpha,\phi)$	23.9	25.3

Table 4.3: Comparison among optimum DIDPA performance obtained by applying the coordinate descent algorithm to the QSM for PAE maximization. All optimized performances involve the ILC-based analytical linearization of the QSM during the optimization.

Algorithm	$\mathbf{P_{out}^{RF}}$ (dBm)	PAE (%)	PAE Evals
Nominal (no optim)	24.2	18.2	–
Coordinate descent $(V_{GG}^{M,D},V_{GG}^{M,F}) \rightarrow (V_{GG}^{A,D},V_{GG}^{A,F}) \rightarrow (\alpha,\phi)$	23.9	25.3	1730
Coordinate descent (iterated) $(V_{GG}^{M,D},V_{GG}^{M,F}) \rightarrow (V_{GG}^{A,D},V_{GG}^{A,F}) \rightarrow (\alpha,\phi)$	23.4	26.2	10,380
Bayesian	23.6	26.1	100

Table 4.4: Comparison among nominal and optimum DIDPA performance obtained by applying the various single-objective optimization algorithms to the QSM for PAE maximization. All optimized performances involve the ILC-based analytical linearization of the QSM during the optimization.

4.3 Bayesian Optimization

The Bayesian optimization (BO) algorithm aims at minimizing an unknown scalar objective function that is expensive to evaluate (e.g., the evaluation is expensive in terms of time or resources, or the number of times the objective function can be evaluated is otherwise limited). The approach itself may be placed in the general class of surrogate methods as it exploits a SuMo to find the expected minimum at every iteration. The SuMo is extracted from a dataset $\mathcal{D}$ composed by the previous evaluations exploiting a regression algorithm and updated with new samples at every iteration.

The peculiar aspect of BO consists of using a stochastic model $\tilde{g}(\mathbf{x})$ as SuMo [98]. In this context, $\tilde{g}(\mathbf{x})$ does not directly provide a deterministic prediction of the value of $g(\mathbf{x})$ in the evaluated point, but it represent a stochastic process. Therefore, $\tilde{g}(\mathbf{x})$ assigns to every possible $\mathbf{x}$ a random variable whose distribution represents the probability of $g(\mathbf{x})$ assuming a given value. The typical SuMo for Bayesian optimization is the Gaussian Regression Model (RGM) which, in this work, is extracted on top of the baseline QSM made of AM/AM–AM/PM characteristics of the DIDPA, as discussed in Section 4.1. The RGM is based on Gaussian processes, characterized by their covariance function [99].

Two key elements must be defined for implementing BO:

1. A parametric model for the Gaussian process covariance function. The parameters of this model represent the hyperparameters of the RGM, which are updated at every iteration using the samples of $g(\mathbf{x})$. The basis functions that are typically used in these applications are the radial basis functions or squared exponential functions. In this work, the covariance model is based on the Matern functions (the Matern functions are the default basis functions adopted by the MATLAB bayesopt routine used in this work) [99].

2. The acquisition function (AF) is used to estimate the location of the minimum/maximum of interest. Since the RGM does not provide a

deterministic value for the RGM estimation, it is necessary to choose a function that selects the predicted value among all possible ones. Therefore, the AF takes the stochastic process as the input, and it provides a deterministic function, whose minimum/maximum is the point that will be evaluated by the objective function. One possible strategy is to choose the AF that calculates the expected improvement or the probability of improvement in the evaluated point [100]. The AF used in this work is called lower confidence bound:

$$a(\mathbf{x}) = \mu(\mathbf{x}) - w\sigma(\mathbf{x}), \tag{4.3}$$

where $\mu(\mathbf{x})$ and $\sigma(\mathbf{x})$ are, respectively, the mean and the variance of the Gaussian process in the evaluated point $\mathbf{x}$, while w is a scalar parameter used to select the tradeoff between exploring unknown points or searching new optima close to the previously expected ones.

Figure 4.6 outlines the basic steps of the adopted algorithm. At every iteration n, the method extracts the RGM from the dataset $\mathcal{D}_n$, which is the collection of all the evaluations of the objective function $g(\mathbf{x})$ at that iteration. Then, it selects the point $\mathbf{x}_n$ that should be evaluated next by minimizing the AF. At the end of every iteration, the method evaluates the exit conditions, which in this case are set as a maximum number of iterations without an improvement of the objective function.

The result of applying this algorithm to maximize the PAE of (4.2) as calculated using the QSM (AM/AM–AM/PM characteristics) of the DIDPA is shown in Tab. 4.4. The BO results in a similar optimal point as the iterative version of CD, but it requires much less evaluations of the objective function.

4.4 Multi-Objective Bayesian Optimization

It is of clear interest for PA application to optimize not only the PAE (single-objective optimization), but the compromise between PAE and RF

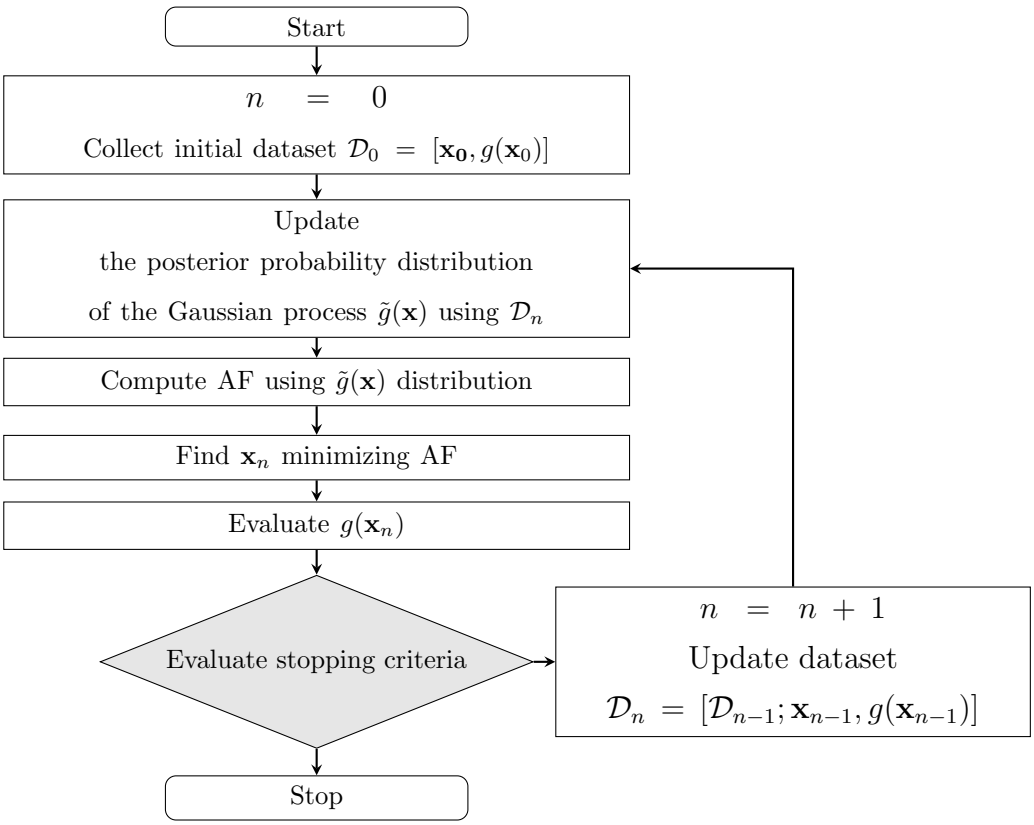

Figure 4.6: Flow chart for single-objective Bayesian optimization.

output power. Table 4.4 highlights a trade-off between PAE and P_{out}^{RF}, since the points found optimizing the PAE show a lower level of P_{out}^{RF}. In order to preliminarily visualize such a trade-off for the DIDPA under study, Figure 4.7 reports an extensive sampling of the space of the variables from a high number of evaluations of the QSM, reporting the ILC-based linearized performance on the 2D plane of the objectives. The solution points highlighted with red circles identify the non-dominated points (Pareto frontier) representing best PAE–RF output power trade-offs.

Rather than performing an unfeasible high amount of function evaluations, an efficient way to identify the Pareto frontier consists of combining the FoMs to be optimized in a single scalar objective function $g(\mathbf{x})$ and thus adopt a single-objective optimization algorithm such as in the previously de-

scribed CD or BO cases. In particular, the BO was chosen for this test given that it compared favorably with respect to CD. A polynomial combination among two different FoMs is considered:

$$g(\mathbf{x}) = \lambda f_1(\mathbf{x})^k + (1-\lambda) f_2(\mathbf{x})^k; \qquad \text{with } \lambda \in [0,1]; \tag{4.4}$$

where k is the polynomial order, λ is the combination parameter, while $f_1(\mathbf{x})$ and $f_2(\mathbf{x})$ are normalized scalar FoMs.

Considering the DIDPA, the scalar FoMs to be used in the problem in (4.4) are obtained from the PAE and P_{out}^{RF} in (4.2) by means of the following normalization:

$$f_1(\mathbf{x}) = 1 - \frac{PAE(\mathbf{x}) - PAE_{min}}{PAE_{max} - PAE_{min}}; \qquad f_2(\mathbf{x}) = 1 - \frac{P_{out}^{RF}(\mathbf{x}) - P_{\text{out, min}}^{RF}}{P_{\text{out, max}}^{RF} - P_{out,min}^{RF}}; \tag{4.5}$$

where PAE_{max} is the result of single-objective PAE maximization, while PAE_{min} is the PAE value in the point that maximizes P_{out}^{RF}. $P_{\text{out, max}}^{RF}$ is the result of the single objective P_{out}^{RF} maximization, while $P_{\text{out, min}}^{RF}$ is the P_{out}^{RF} value in the point that maximizes PAE. The set of optimal points have then been obtained by sweeping λ from 0 to 1 with the aim to identify the non-dominated points of the Pareto frontier. Each of the points is obtained through one iterative single-objective optimization of the QSM of the DIDPA as depicted in Fig. 4.6, where $\lambda = 0$ corresponds to P_{out}^{RF} maximization (f_2 minimization), while $\lambda = 1$ corresponds to PAE maximization (f_1 minimization).

Clearly, the way the FoMs are summed influences the results [101]. Figure 4.8 reports the optimal points against the normalized FoMs, showing the effects of changing the order k of the polynomial combination within the optimization. In particular, Figure 4.8a, reports the use of a linear combination ($k = 1$), showing that, in this case, it is not possible to identify optimal points laying in the non-convex region of the normalized Pareto front. Indeed, the algorithm provides those optima best favoring either f_1 or f_2, but not their concurrent combination, given that the points in the non-convex region do

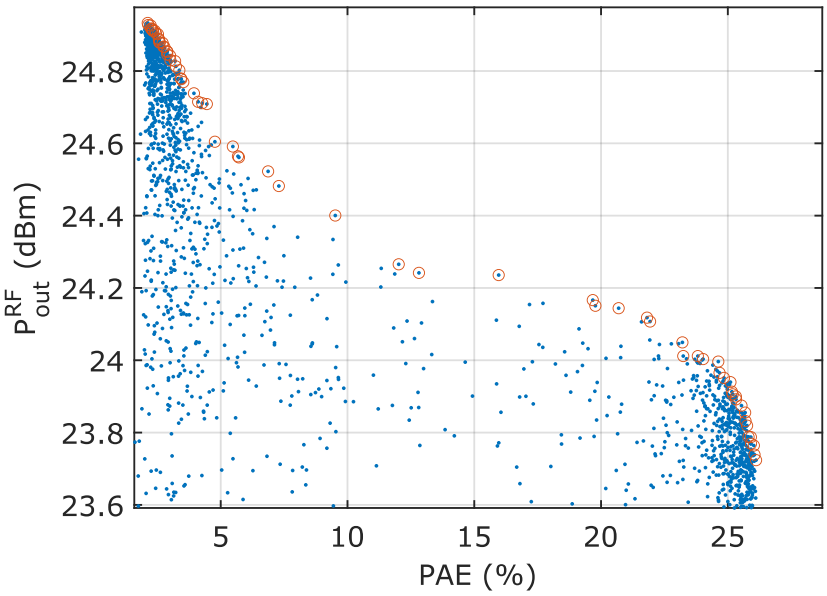

Figure 4.7: Sampling of the six-dimensional variable space showing many possible trade-off points between RMS RF output power and PAE, highlighting the profile of non-dominated points (Pareto frontier).

not actually represent a minimum for the combined objective function. Conversely, Figure 4.8b shows the estimated Pareto frontier with $k = 3$, allowing to identify the non-dominated trade-off points in the non-convex region.

Figure 4.9 displays the same results as Fig. 4.8, yet de-normalized to the actual P_{out}^{RF} and PAE values. Figure 4.9a shows the trade-off points obtained by performing the MOO based on a linear combination of the objectives ($k = 1$), which is not able to converge to the optimal trade-off points in the non-convex region of the Pareto frontier previously reported in Fig. 4.7. The case using the non-linear combination ($k = 3$) is instead able to identify the non-convex region of the Pareto front. The latter thus demonstrates the possibility of extracting the Pareto frontier in an efficient way by BO.

In Fig. 4.9b, P1 and P4 are the values for maximum P_{out}^{RF} and PAE, identified by optimizing the combined objective function with $\lambda = 0$ and $\lambda = 1$, respectively. P2 and P3 represent two possible compromises between P_{out}^{RF}

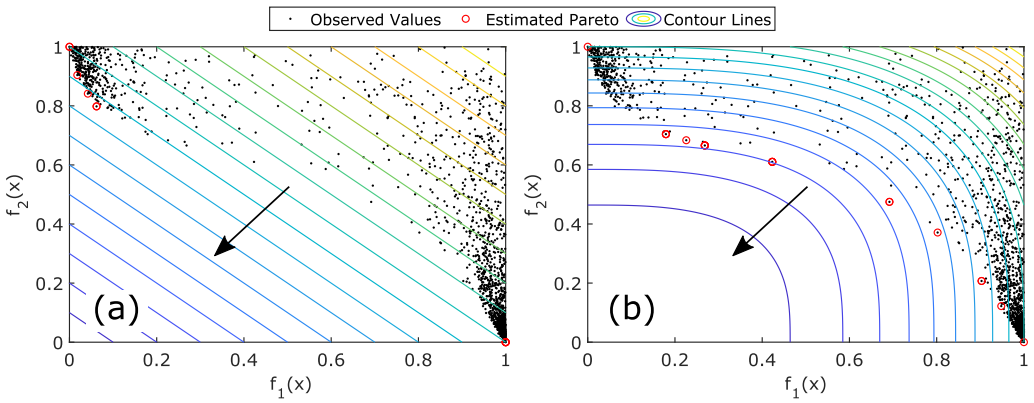

Figure 4.8: Estimated optimal points (red circles) in a non-convex Pareto frontier with different FoM combinations with contour lines of the combined objective function for $\lambda = 0.5$. (**a**) Linear combination ($k = 1$), (**b**) non-linear combination ($k = 3$). The arrows indicate the combined minimization of the two scaled FoMs.

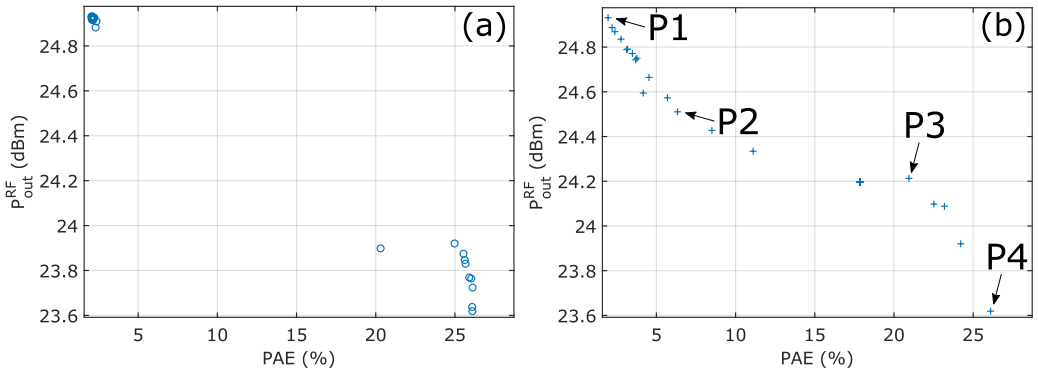

Figure 4.9: Estimated Pareto frontier between RMS RF output power and PAE obtained with a (**a**) linear combination ($k = 1$) and (**b**) non-linear combination ($k = 3$), while sweeping the combination factor λ.

and PAE, and they are, respectively, obtained with $\lambda = 0.16$ and $\lambda = 0.84$. The results related to these points are summarized in Tab. 4.4, where they are compared with the values previously obtained with the CD algorithm.

Algorithm	λ	P_{out}^{RF} (dBm)	PAE (%)	Nr of Function Evaluations
Nominal (no optim)	–	24.2	18.2	–
Coordinate descent (iterated)	–	23.4	26.2	10,380
Bayesian P1	0	24.9	2.0	100
Bayesian P2	0.16	24.5	6.3	100
Bayesian P3	0.84	24.2	20.0	100
Bayesian P4	1	23.6	26.1	100

Table 4.5: Comparison of PA performances obtained by means of PDF-based SuMo simulation at the optimal points.

4.5 DIDPA Performance under Wideband Modulation

The optimal points based on the QSM (Tab. 4.4) must be validated under actual wideband-modulated signals, thus accounting for the DIDPA dynamic effects. This validation is here performed by circuit envelope (CE) simulations with a random phase multitone as input test signal, whose statistics can be setup to faithfully reproduce modern 5G signals [28] (See Sec. 1.2.1). The adopted signal BW and tone spacing are 100 MHz and 10 kHz, respectively, resulting in a 10k-tone signal with PAPR = 10.4 dB. Coherently with the considerations in Section 4.1, the non-parametric ILC algorithm was applied in order to linearize the DIDPA.

The test results of the single-objective optimization for PAE maximization by CD (Section 4.2) and BO (Section 4.3) are reported in Tab. 4.6. First of all, it should be noted that the nominal DIDPA configuration without optimization displays a reduction of more than 2% in terms of PAE and 0.4 dB of RMS RF output power with respect to the PDF-based evaluation of the QSM in Tab. 4.4. This difference is expected, due to the dynamics accounted for by the multitone CE simulation.

Also under actual high-PAPR-modulated excitation, the optimized performance obtained provides a substantial improvement with respect to the nominal conditions (up to $\sim 8\%$ of absolute PAE increase), although slightly worse than the one predicted by the PDF-based QSM in Tab. 4.4. The results are similar between CD and BO, although BO takes much fewer evaluations.

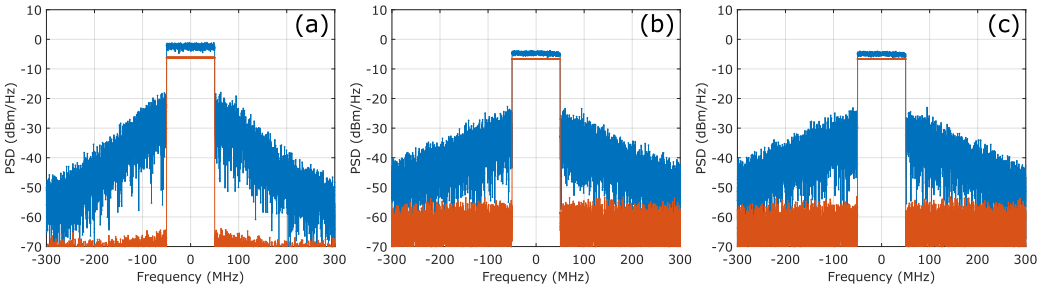

Figure 4.10: Spectra of the output RF signal before (blue lines) and after linearization (red lines) with PA parameters at (**a**) nominal values, (**b**) after coordinate descent (iterated) optimization, and (**c**) after Bayesian optimization (P4).

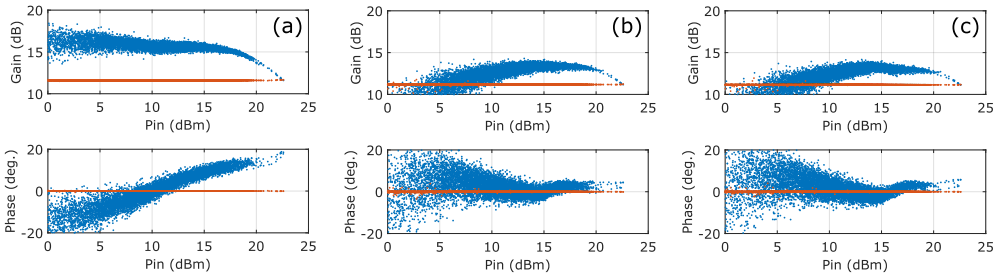

Figure 4.11: PA gain and AM/PM characteristics before (blue lines) and after linearization (red lines) with PA parameters at (**a**) nominal values, (**b**) after coordinate descent (iterated) optimization, and (**c**) after Bayesian optimization (P4).

The hypothesis of sufficient linearization is demonstrated by the fact that both the adjacent-channel power ratio (ACPR) and NMSE are low enough with respect to the typical specifications of telecom standards.

Figure 4.10 shows the spectra before and after the ILC-based linearization of the DIDPA with nominal parameters, and for the optimal points identified by the CD and the BO, corresponding to the performance FoMs reported in Tab. 4.6. The same data are depicted in Fig. 4.11 in terms of dynamic gain and AM/PM characteristics.

Those optimal trade-off points identified by the MOO described in Sec-

Algorithm	λ	P_{out}^{RF} (dBm)	PAE (%)	ACPR (dB)	NMSE (dB)
Nominal	–	23.8	16.7	−65.6	−59.0
Coordinate descent (best permutation)	–	23.5	24.0	−56.7	−50.1
Coordinate descent (iterated)	–	23.4	24.6	−54.5	−47.8
Bayesian P1	0	25.0	2.0	−52.8	−46.1
Bayesian P2	0.16	24.1	6.0	−56.2	−47.8
Bayesian P3	0.84	23.7	20.0	−60.2	−53.6
Bayesian P4	1	23.4	24.6	−52.2	−45.7

Table 4.6: Comparison of PA performances obtained by means of envelope simulation with modulated signals at the optimal points found running the coordinate descent or Bayesian optimizations on the PDF-based SuMo.

Algorithm	α	ϕ (deg)	$V_{GG}^{M,D}$ (V)	$V_{GG}^{M,F}$ (V)	$V_{GG}^{A,D}$ (V)	$V_{GG}^{A,F}$ (V)
Nominal	0.5	−90	−1.7	−1.7	−2.3	−2.1
Coordinate descent (best permutation)	0.5	−80	−1.8	−2.3	−2.5	−2.7
Coordinate descent (iterated)	0.6	−75	−1.9	−2.5	−2.4	−2.9
Bayesian P1	0.49	−87	−0.6	−0.3	−0.5	−0.1
Bayesian P2	0.21	−69	−1.1	−2.0	−1.0	−1.4
Bayesian P3	0.43	−81	−1.7	−2.2	−2.2	−2.2
Bayesian P4	0.61	−75	−1.9	−2.6	−2.4	−2.9

Table 4.7: Nominal values of the parameters considered for DIDPA optimization.

tion 4.4 were also validated under the same modulated excitation. In particular, optimal points P1-P4 are reported in Tab. 4.6, demonstrating a very good alignment with Tab. 4.4 and the effectiveness of the SuMo-based optimization, despite the slightly reduced overall performance. Also in these cases, the linearity performance is satisfactory with respect to the specifications by telecom standards. Table 4.7 reports the values of the optimization variables corresponding to the FoMs shown in Tab. 4.6. In the case of single-objective PAE maximization (i.e., in the CD method and Bayesian P4 point), Tab. 4.7 highlights that BO and iterated CD deliver almost the same operating point, although many fewer function evaluations are needed for BO (see Tab. 4.4). This relatively fast convergence property allows the efficient exploration of the Pareto frontier by means of a series of single-objective optimization. In order to show the linearization performance achieved in the optimal point P3 by BO, Figs. 4.12 and 4.13, respectively, show the spectra, gain and AM/PM characteristics of the DIDPA before (blue curves) and after (red curves) the ILC-based linearization.

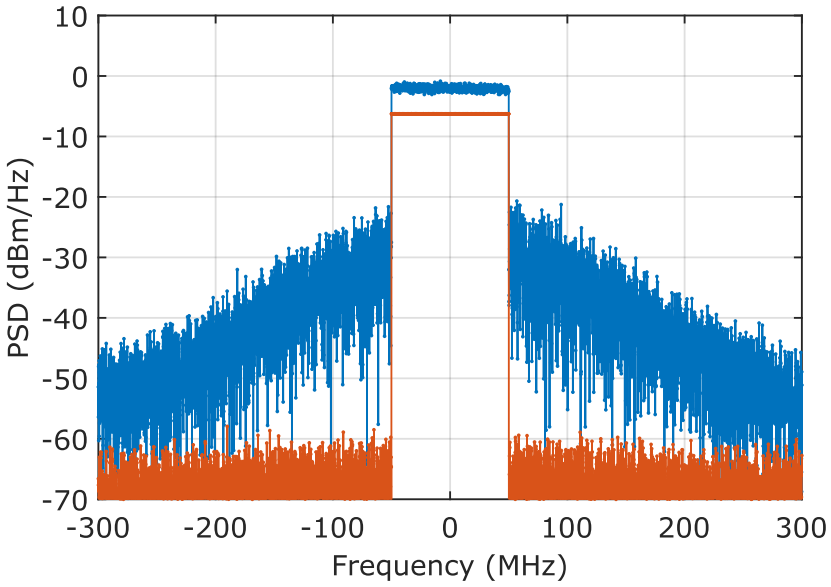

Figure 4.12: RF output spectrum before (blue lines) and after linearization (red lines) at optimal point P3.

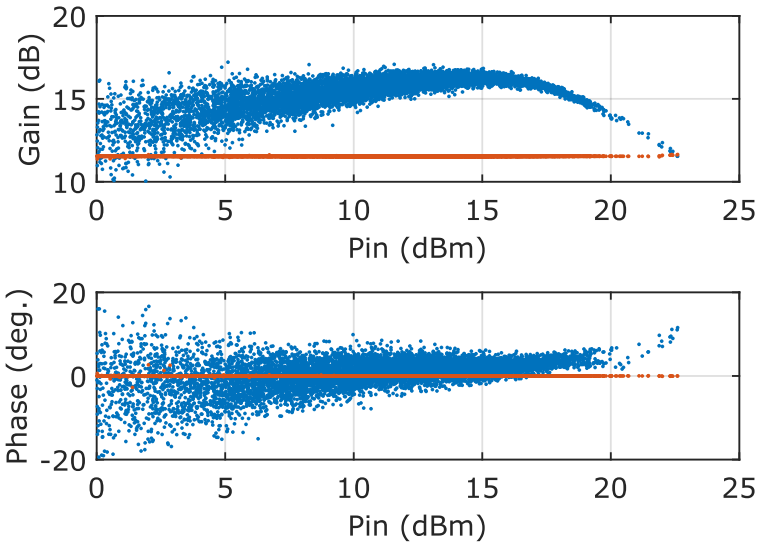

Figure 4.13: PA gain and AM/PM characteristics before (blue lines) and after linearization (red lines) at optimal point P3.

4.6 Conclusion

This chapter offers a preliminary analysis of the MOO applied to the DIDPA. The tests were performed using a simulation environment. The main achievements can be summarized as follows:

- the BO has been found suitable to be used as an algorithm to optimize time-consuming functions. Table 4.4 demonstrates that the BO results in a similar optimal point as the iterative version of CD, but it requires much less evaluations of the objective function.

- The QSM can be used as a surrogate model to avoid using direct modulated simulations or measurements. The optimal points obtained using the QSM has been successfully linearized and the efficiency performance obtained after the linearization is comparable to the QSM predictions.

Chapter 5

DIDPA Optimization on Direct Measurements

5.1 Problem Statement

In order to assess nonlinear devices, such as radio-frequency (RF) PAs, network analysis is employed to extract FoMs like input/output match, available power gain, and load-pull contours, along with signal analysis FoMs like error vector magnitude (EVM) [102]. Modern multi-input PA topologies like DIDPA need complex modules with multiple ports and input signals [91]. These complexities, including non-50-Ω interfaces, are now addressed through microwave monolithic integrated circuits (MMICs), requiring on-wafer measurements before integration into multi-chip modules [103–105].

Various receiver options exist for capturing wideband (WB) signals at millimeter-wave frequencies, each with its advantages and disadvantages. Direct measurement of the time-domain RF signal using high-frequency oscilloscopes in the 70-GHz to 110-GHz range is a straightforward approach but may lack resolution and prove costly for multi-channel high-frequency measurements [106–108]. Alternatively, spectrum analyzers in the frequency domain remain a conventional method for characterizing WB signals, measuring figures-of-merit based on spectral regrowth. However, the trend to-

wards complex modulation schemes necessitates vector signal analysis tools for millimeter-wave component testing, introducing challenges in cost and impedance mismatch handling [109,110].

Legacy vector network analyzers (VNAs) primarily focus on measuring scattering parameters, yet recent advancements have expanded their functionalities for large-signal measurements, multi-port setups, and WB signal analysis [8,9,28,111–120]. Techniques have been proposed for characterizing complex devices such as power amplifiers, frequency converters, and two-port devices using spectral correlations and absolute power measurements. However, the inherent narrow bandwidth of VNAs poses challenges for modern modulation bandwidths, leading to proposed solutions involving separate measurement and stitching for full-BW response [118,121].

This Chapter introduces an alternative VNA-based wideband multiple-input multiple-output (MIMO) system, which has been extendly described in [122,123]. The setup utilizes a mixer-based VNA architecture with wideband intermediate frequency (IF) outputs. This design allows external digitizers to capture the full modulation bandwidth, with coherent averaging for dynamic range and vector error correction for non-50-Ω measurements. Building on prior research [124], this study provides a more detailed description of the measurement system and investigates limiting effects on overall performance. It explores mixer switch and local oscillator isolation during calibration, addressing discrepancies between continuous-wave (CW) and WB calibrations. Additionally, the study delves into the effects and limitations of intermodulation distortion (IMD), interleaving, and quantization in the WB IF acquisition using an external oscilloscope.

The system capabilities are demonstrated in characterizing an on-wafer DIDPA at 24 GHz. The tuning of DIDPA inputs allows for adaptability and improved efficiency. The setup is able to perform the wideband characterization and linearization of a dual input Doherty PA at millimeter-wave frequencies. By leveraging on the setup capabilities, a dual-input control (DIC) algorithm is proposed in order to set an user-defined relationship con-

trol across a 600-MHz bandwidth at the DUT on-wafer plane.

The BO measurement validation follows two different approaches: the first relies on a quasi-static model (QSM) obtained from continuous-wave measurements, while the second relies on direct modulated measurements. The optimization toolbox focuses on PAE improvement, while ensuring sustained linearity levels with DPD linearization. The approach involves a joint optimization process for both efficiency and linearity, considering the mutual effect between DPD linearization and PAE-maximization throughout. The methodology is validated with an on-wafer multiport measurement system based on a VNA. The application of the DIC procedure, in conjunction with BO, increase in PAE while maintaining the same level of linearity as the nominal device. The efficacy of the QSM approach is verified through optimization using a BO approach based on direct modulated measurements. Comparative analysis between the two approaches, demonstrates no significant differences between the performance of QSM-BO and results obtained through direct modulated measurements and linearization.

5.2 Millimeter-wave MIMO VNA Setup

5.2.1 Measurement system

The block diagram and photograph illustrating the on-wafer three-port measurement setup, as provided by the FBH institute, can be observed in Fig. 5.1a-b [123] [122]. To couple the three incident and three reflected waves, external directional couplers and pad-attenuators are employed, strategically configured to optimize the dynamic range of the acquisition process. The measurement of the coupled waves is conducted using a specialized 4-port Keysight N5247BC PNA-X vector network analyzer (VNA). A notable customization in comparison to a conventional narrowband VNA involves the incorporation of a wideband downconversion hardware, facilitating an intermediate IF exceeding 2 GHz, and cable re-routing for IF signal measurement through external hardware. In this particular setup, the six IF signals un-

dergo coherent digitization employing a 6-GHz digital sampling oscilloscope (DSO - Keysight MXR608A).

Calibration of the setup is performed across a 600 MHz band at the on-wafer DUT reference plane, employing a tailored calibration procedure based on a short-open-load-thru (SOLT) method and absolute-amplitude steps with an external power meter. The magnitude and phase of the waves are computed utilizing identified error terms and the power coefficient, assuming favorable output matching conditions. The DUT is stimulated at port 1 and port 3 through two external IQ mixers, which are driven by a common local oscillator generated internally by the VNA. Complex-baseband IQ signals are generated utilizing a Tabor WX2184C arbitrary waveform generator. The input power levels to the DUT input ports are augmented through high-gain, high-power pre-amplifiers. All instruments in the setup synchronize through a shared 10 MHz reference and are triggered by a single common trigger signal.

5.2.2 Dual Input Signal Control

While the measurement system enables full network analysis, this study focuses solely on forward measurements with signals injected at P1 and P3. DUT is nominally matched at the inputs and output, with anticipated low reflections. Additionally, system reflections within the measured band are negligible. To address multiport wave correction, a preliminary approach involves calculating each wave at the reference plane as described in [125]. This computation utilizes the raw data for all waves and their respective error terms, excluding cross contributions from other ports. This method can be viewed as a 1-path, 3-port approach, deemed sufficiently accurate for the current setup and DUT. However, future implementations will incorporate more comprehensive error models. After correcting the waves to the reference planes, power meter data, along with the corrected thru-line waves, is utilized to calculate power factors for each port, thereby correcting the waves to absolute power.

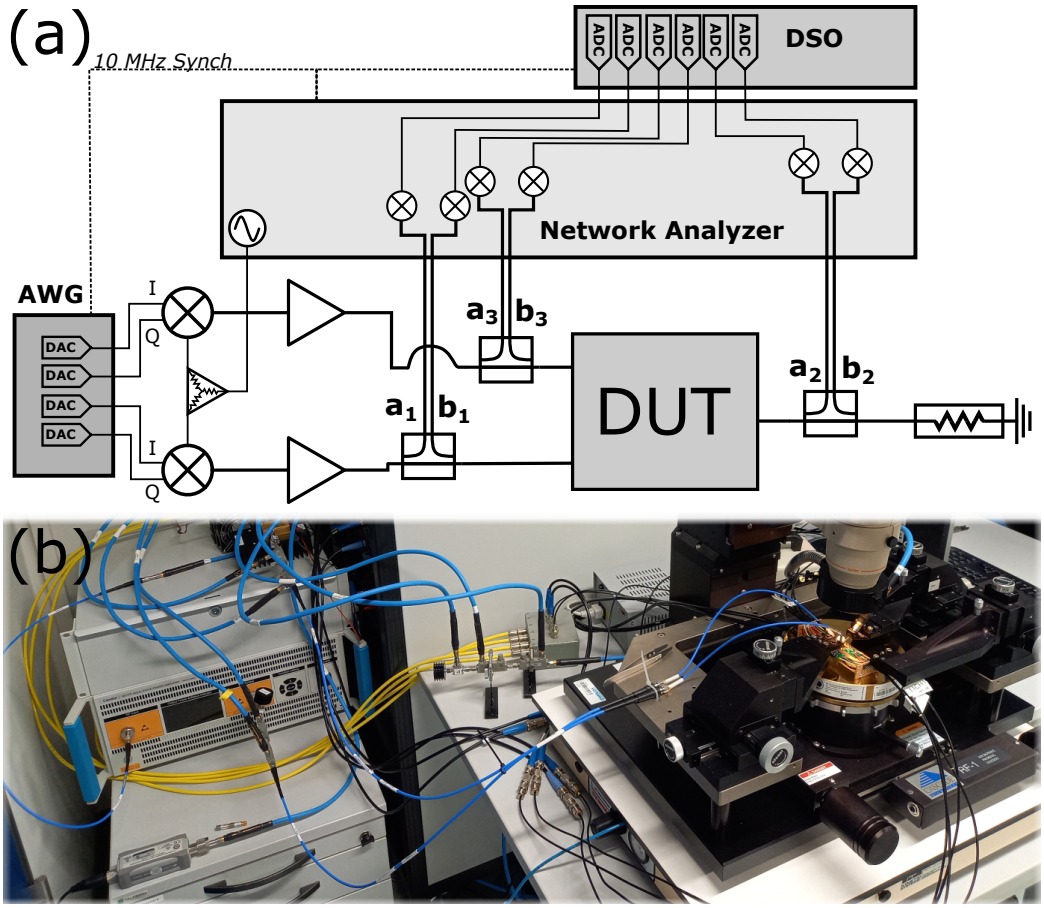

Figure 5.1: (a) Measurement system block diagram and (b) picture.

The nonlinear characterization of multi-port devices in the proposed environment necessitates tailored control of the excitations applied to the DUT [126]. In the already published works [122] and [124], the quadrature hybrid is represented by the condition $a_3 = \alpha e^{j\phi} a_1$, where α and ϕ denote the splitting ratio and phase, respectively, across the entire bandwidth of interest. These works focused on the hybrid synthesis capabilities, various non-idealities in the hardware signal path of each port may hinder precise control of the actual waveforms at the DUT input reference planes. Therefore, even when specific α or ϕ values are imposed on the digital waveforms, different and potentially non-physical conditions might be realized at the DUT analog inputs. Simi-

lar to active load-pull [9], the customized control of the two wideband input signals allows for testing the impact of various hybrid parameters on PA performance without the need for a physical realization of the actual circuit.

Conversely, this work focuses on digitally synthesizing an arbitrary relationship $a_3 = f(a_1)$ between incident waves of the two digitally controlled inputs. To realize this a DIC procedure based on an iterative-learning-control (ILC) [32] scheme is proposed, Fig. 5.2. For each iteration of the loop, the fitting errors e_1^n and e_3^n of the incident waves of the two branches of the DUT are calculated as follows:

$$\begin{aligned} e_1^n &= 20\log_{10}\left(\frac{||\mathbf{a}_1^n - \mathbf{a}_{1,t}^n||}{||\mathbf{a}_{1,t}^n||}\right), \\ e_3^n &= 20\log_{10}\left(\frac{||\mathbf{a}_3^n - f(\mathbf{a}_1^n)||}{||f(\mathbf{a}_1^n)||}\right), \end{aligned} \tag{5.1}$$

where $\mathbf{a}_{1,t}^n$ is the target incident wave for the first branch. As the iteration do not satisfy the arbitrary relationship at the DUT reference plane, iterative corrections are subsequently applied using measurements from the multiport setup to reach the condition $a_3 =^n= f(a_1^n)$. For the inner loop, the ILC algorithm is run (using the learning gains Γ_1^k and Γ_3^k) as follows:

$$\begin{aligned} \mathbf{x}_1^{(n+1)} &= \mathbf{x}_1^n - \Gamma_1(\mathbf{a}_1^n - \mathbf{a}_{1,t}), \\ \mathbf{x}_3^{(n+1)} &= \mathbf{x}_3^n - \Gamma_3(\mathbf{a}_3^n - f(\mathbf{a}_1^n)). \end{aligned} \tag{5.2}$$

The procedure is summarized in the flow chart in Fig. 5.5. Figure 5.3a qualitatively shows how the DIC converges to the target relationship in case of a hardware power splitter emulation, that is, a constant relationship between a_2 and a_3. Figure 5.3b shows the same iterative behavior while setting a static nonlinear relationship. The quantitative results in terms of fitting errors e_1 and a_3 reached by the DIC after convergence in the two case are summarized in Fig. 5.4. It is worth noting that the error e_3 reached while setting a static nonlinear function is higher that the one reached for a constant relationship. This can be explained by the higher BW necessary to set a nonlinear relationship, while the available BW for measuring the incident

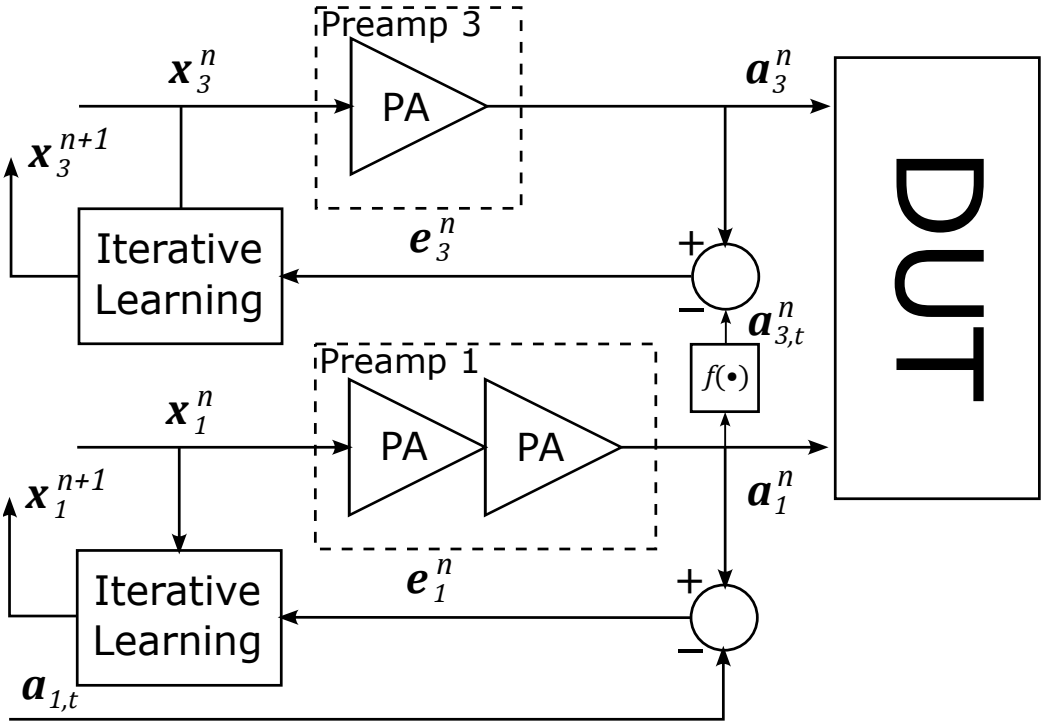

Figure 5.2: Dual-input control block diagram.

waves and setting the corrected digital input is fixed at 600 MHz (Sec. 5.2.1).

5.3 Optimization Problem Statement

5.3.1 Dual Input - Single Output Device-Under-Test

The DUT refers to an on-wafer Microwave Monolithic Integrated Circuit (MMIC) DIDPA crafted in the NP15-00 150-nm GaN-on-SiC process by WIN Semiconductors, specifically designed for operation at 24 GHz. The circuit configuration is depicted in Fig. 5.6a-b. Both the primary and auxiliary amplifiers comprise two amplification stages each. The driver stage employs 2×75 μm High Electron Mobility Transistors (HEMTs), and the final stage utilizes 6×75 μm HEMTs. As depicted in Fig. 5.6a, gate biases and drain voltages are free to be accessed for the setup and can be individually tuned by

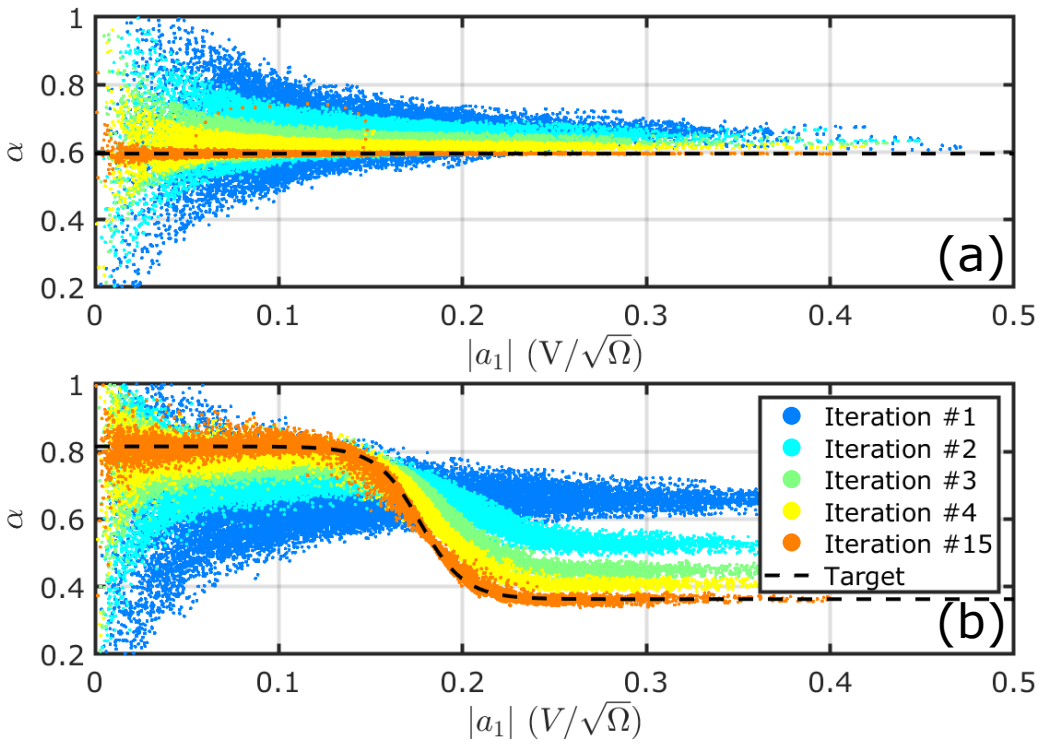

Figure 5.3: Iterative behavior of the dual-input control while setting (a) a constant power splitting ratio and (b) a static shaping between a_1 and a_3.

the optimization algorithm. Thus, the gate bias and drain voltage values for all four HEMTs, along with the input splitting (both amplitude and phase) between the two inputs, are considered as optimization variables, as detailed in Tab. 5.1.

5.3.2 Digital Splitter Parametrization

Referring to the Fig. 5.6, the so called digital splitter is the complex function f, which identifies the relationship between the input waves a_1 and a_3 that must be satisfied by the dual-input control. In order to associate tuning variables with f it is necessary to adopt a parametrization. The first tested parametrization for the digital splitter consists of a constant relationship

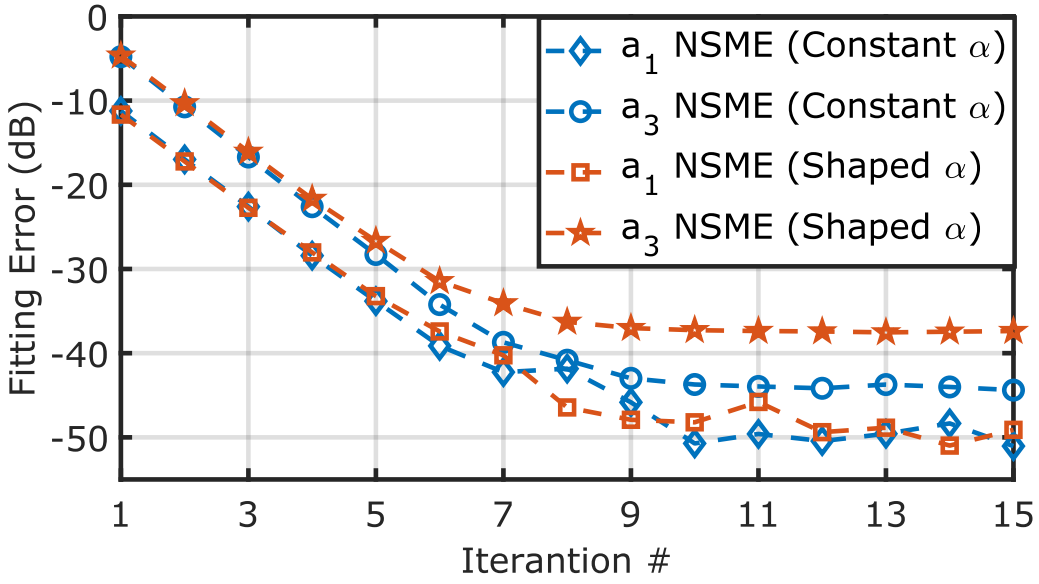

Figure 5.4: fitting error in terms of NMSE among a_1, a_3 and their respective targets. The different markers highlight the case in which a constant relationship or a static shape is set between the two branches.

between a_1 and a_3:

$$a_3(n) = f_{\alpha,\phi}(a_1(n)) = \alpha_r e^{-i\phi} a_1(n) = \sqrt{\frac{1-\alpha}{\alpha}} e^{-i\phi} a_1(n), \tag{5.3}$$

where α is the fixed power splitting ratio and ϕ is the outphasing term. The second parametrization consists on a shaped function based on the logistic regression (also indicated as sigmoid) function:

$$\begin{aligned} a_3(n) &= f_{r_i,r_f,x_0,d,\phi}(a_1(n)) = \\ &= (r_i + \frac{r_f - r_i}{1 + e^{-\frac{4d(|a_1(n)|-x_0)}{r_f - r_i}}}) e^{-i\phi} a_1(n), \end{aligned} \tag{5.4}$$

where r_i and r_f are the initial and final ratio between a_3 and a_1, x_0 is the turning point, and d is the value of $f'_{r_i,r_f,x_0,d,\phi}(x_0)$, as depicted in Fig. 5.7.

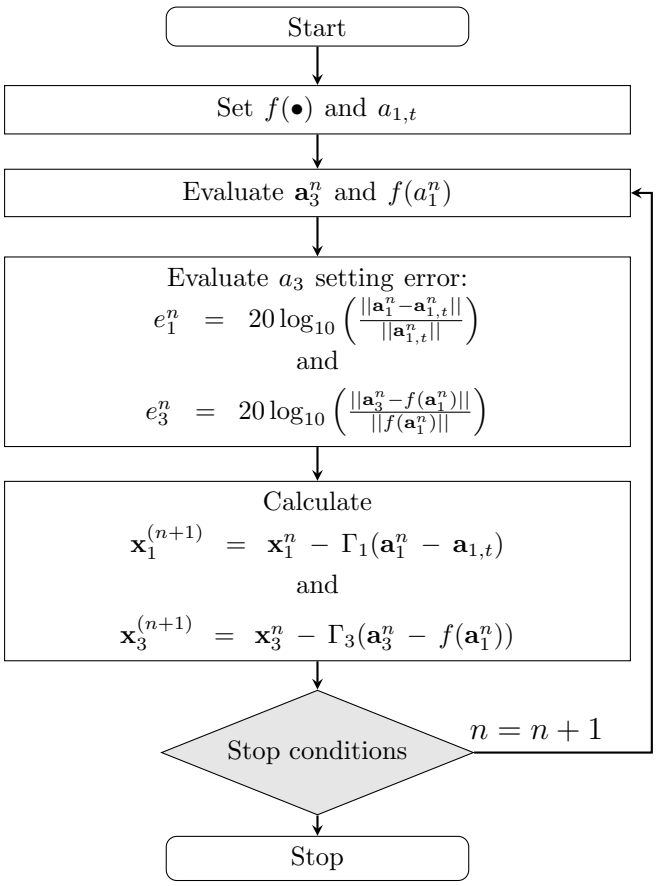

Figure 5.5: Simplified flow chart of the ILC-based algorithm for dual input control.

5.3.3 Digital Predistortion Architecture

Although the DUT is a dual-input device, the DIDPA can be linearized by adopting a single-input single-output DPD architecture [49,50] by placing the DPD block before the digital splitter. In this context, DIC block needs a single input signal $\mathbf{a}_{1,t}$ impose the user-defined relation between $\mathbf{a}_1$ and $\mathbf{a}_3$, as depicted in Fig. 5.2. Thus, the adopted DPD architecture is based on ILC [32], which provides the predistorted input signal $\mathbf{a}_{1,t}$ to the DIC block, as state in Fig. 5.8. Figure 5.8 illustrates the ILC-based DPD (ILC-DPD) architecture, whose iterations can be summarized by the following Equation:

$$\mathbf{a}_{1,t}^{(k+1)} = \mathbf{a}_{1,t}^k - \Gamma(\mathbf{b}_2^k - \mathbf{b}_{2,t}^k), \tag{5.5}$$

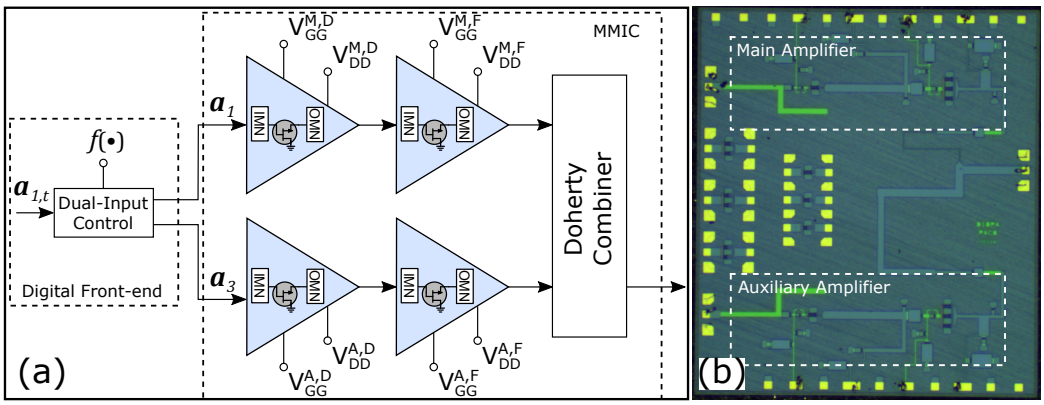

Figure 5.6: (a) dual-input tested device block diagram and (b) picture.

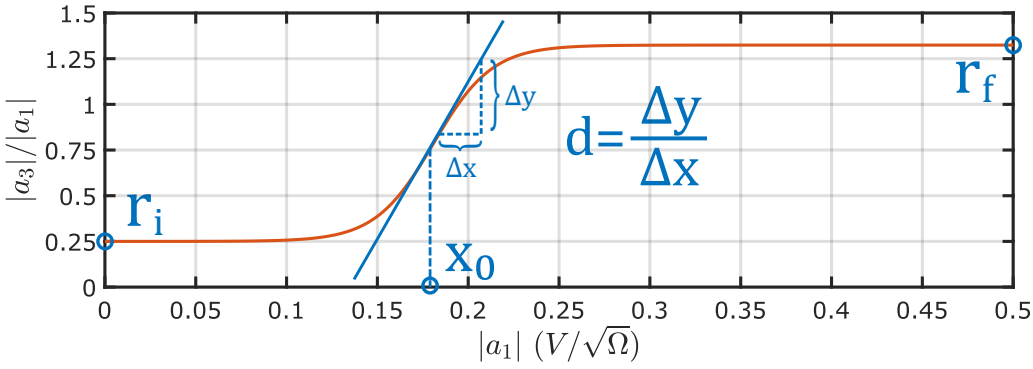

Figure 5.7: Logistic regression shaping function with its defining parameters.

where $\mathbf{a}_{1,t}^{k}$ is the predistorted input signale for the DIC block at the ILC-DPD k^{th} iteration, $\mathbf{b}_{2}^{k}$ is the output signal to be linearized, and $\mathbf{b}_{2,t}^{k}$ is the linearized target output signal. It is worth highlighting that the results of this implementation is a combination of two nested ILC loops. The inner loop implemented in the DIC and the outer loop that realizes the ILC-DPD.

5.3.4 Optimization Algorithm

One of the key elements of the methodology is the adopted optimization algorithm. Considering the DIDPA as a black box function to be optimized,

Variable	Min Value	Max Value
$^{*}V_{GG}^{A,D}$ (V)	-3	-1.5
$^{*}V_{GG}^{A,F}$ (V)	-3	-1.5
$^{*}V_{GG}^{M,D}$ (V)	-3	-1.5
$^{*}V_{GG}^{M,F}$ (V)	-3	-1.5
$^{*}V_{DD}^{A,D}$ (V)	5	20
$^{*}V_{DD}^{A,F}$ (V)	5	20
$^{*}V_{DD}^{M,D}$ (V)	5	20
$^{*}V_{DD}^{M,F}$ (V)	5	20
$^{\dagger}\alpha$	0	1
$^{\dagger\ddagger}\phi$ (deg.)	-180	180
$^{\ddagger}r_i$	0	∞
$^{\ddagger}r_f$	0	∞
$^{\ddagger}x_0$ $(\frac{V}{\sqrt{\Omega}})$	0	0.5
$^{\ddagger}d$ $(\frac{\sqrt{\Omega}}{V})$	0	∞

* DIDPA bias-related tuning variables.

† Constant-power-splitter-related tuning variables.

‡ Shaped-power-splitter-related tuning variables.

Table 5.1: Range of the DUT tuning variables.

the problem can be summarized as:

$$\max_{\mathbf{v}} FoM(\mathbf{v}), \tag{5.6}$$

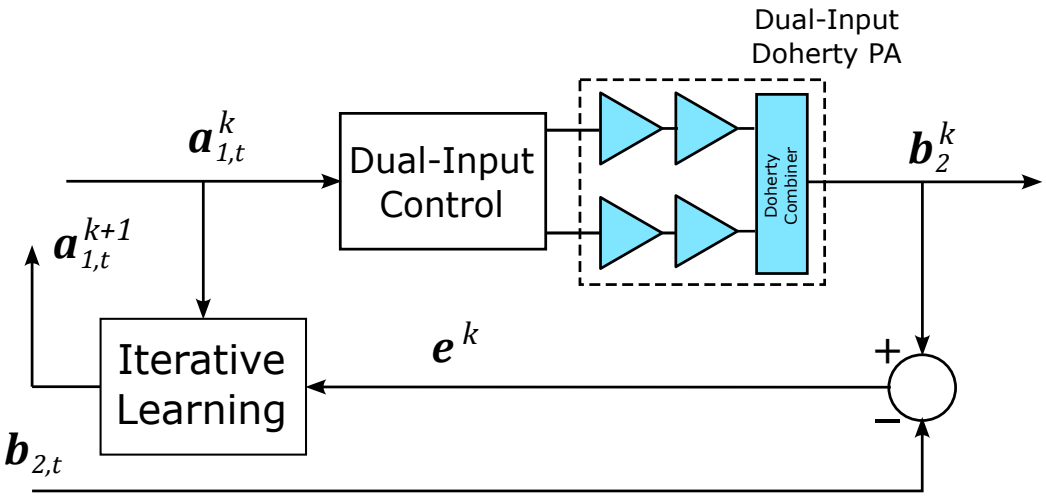

Figure 5.8: ILC-DPD block diagram, which the k^{th} iteration of the ILD-DPD.

where $\mathbf{v}$ is the set of variables (Tab. 5.1) from which the FoM to be optimized depends. In this case, the FoM can be a hard-to-be-evaluated function, since it relies on device measurement. In this context, the BO is an excellent candidate, as it is capable of achieving a robust heuristic by exploring the solution space and converging to the optimal solution with a minimal number of evaluations [91].

5.4 Bayesian Optimization

5.4.1 Quasi-Static Model Optimization

To predict the FoM in the presence of modulated signals using a QSM, the quasi-static CW characteristics of the DIDPA must be weighted by the PDF of the stationary stochastic process corresponding to the relevant excitation signal class. The QSM prediction replicates the approach described in Sec. 4.1.3, but using CW swept measurement instead of simulations. Consequently, the RF output power (P_{out}^{RF}) and PAE are expressed as follows:

$$P_{out}^{RF} = \int_0^{+\infty} P_{out}^{pdf}(p)dp,$$
$$\text{PAE} = \frac{\int_0^{+\infty} P_{out}^{pdf}(p)dp - \int_0^{+\infty} \widehat{P}_{in}(p)P_{out}^{pdf}(p)dp}{\int_0^{+\infty} \widehat{P}_{dc}(p)P_{out}^{pdf}(p)dp}. \tag{5.7}$$

Here, $P_{out}^{pdf}(p)$ is the PDF of the desired output-modulated signal, $\widehat{P}_{in}(p)$ represents the static relationship between the output p and the input $\widehat{P}_{in}$ power of the DIDPA, and $\widehat{P}_{dc}(p)$ represents the static relationship between the output p and the DC absorbed power, Fig. 5.9. Utilizing Eq. (5.7) to calculate FoMs is conceptually equivalent to exciting the QSM with a linearized modulated signal. While this representation may be suboptimal for wideband signals, the method has been demonstrated to be sufficient for identifying key interdependencies among input variables and effective for optimization in the examined case [73]. The actual broadband behavior of the DIDPA can be verified through a final experimental assessment under wideband signal excitation. In this context, the goal is to observe convergence of the FoMs calculated with the PDF-based QSM in (5.7) to the values obtained under wideband signal excitation.

5.4.2 Optimization Applied to Modulated Acquisitions

By employing a quasi-static surrogate model one inherently introduces a model prediction error, especially when considering the DUT behavior under wideband modulated excitation. This discrepancy may lead to variations in PAE or actual linearization performance, potentially causing a misalignment between the optimal tuning values achieved by QSM-based BO and the true optimum.

In contrast, the direct BO approach involves executing the BO algorithm through broadband measurements of the actual DUT, bypassing any intermediate model. For each $\mathbf{x}_n$, the DIDPA undergoes linearization and testing under a fixed modulated excitation. The FoMs are directly derived from wideband acquisitions, albeit at a higher cost in terms of time and resource

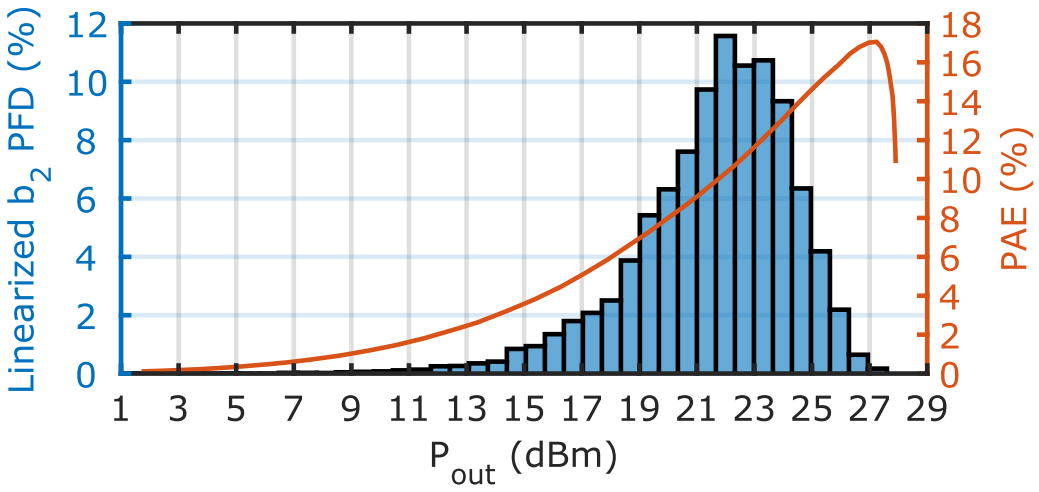

Figure 5.9: Relationship between the PAE of the DDPA and the output power distribution of the linearized DUT.

utilization compared to the QSM-based evaluation in Sec. 5.4.1. As the BO tends to drive the DIDPA into strong nonlinear operation for high PAE, and the DPD in this case cannot be represented as a *perfect* inverse static LUT, a minimum linearity constraint in terms of normalized mean square error (NMSE) after DPD is imposed to determine the optimal set of tuning variables.

5.5 Circuit Test with WB Measurement

5.5.1 DIDPA Linearization

Similarly to [118], a preliminary sweep of α_r and ϕ under CW excitation allowed to identify the specific input splitting values for obtaining the maximum power-added efficiency (PAE) at the given RF available input power of $P_{\mathrm{AVS}} = 16$ dBm. This sweep resulted in the input splitting values ($\alpha_r = 1, \phi = -30°$), referred as **P0** in the following. In order to emulate this splitting behavior across the BW, these conditions are imposed by implementing the inner loop in (5.2). For this test, the DUT is excited by a

random-phase multi-tone input test signal, whose statistics can be shaped to match 5G signals [28]. In particular, the excitation signal consists of 1k tones, covering a BW of 100 MHz and having a peak-to-average power ratio (PAPR) of 9.2 dB.

The red line in Fig. 5.10a corresponds to the injected wave $\mathbf{a}_1$ to the main branch of the DIDPA, while the blue line corresponds to the $\mathbf{b}_2$ wave after imposing the input splitting conditions **P0** without applying any linearization. The peak output power is $P_{\text{OUT}}^{\max} = 29.3$ dBm, corresponding to more than 5 dB of compression. Figure 5.10b shows the iterative behavior of the inner loop for setting the selected input split. Figure 5.11 reports the same plots as Fig. 5.10 when applying DIDPA linearization, i.e., running both the outer loop in (5.5) and the inner loop in (5.2). The performance results in terms of ACPR, EVM, PAE, and average output power are reported in Table 5.2 for both cases (with and without linearization).

Figure 5.12 displays the corresponding behavior of the iterative normalized mean square error (NMSE) between $\mathbf{a}_3$ and $\alpha_r e^{j\phi}\mathbf{a}_1$ (inner loop) across up to 11 iterations of the outer loop. It can be seen that, in all cases, the convergence (and hence, the user-imposed input signal splitting) can be achieved with an NMSE lower than -30 dB within four ILC iterations.

5.5.2 Selection of Input Splitting under Wideband Modulation

The dual input signal control and linearization techniques described in Section 5.2.2 allow to identify the optimum α_r and ϕ values directly under modulated conditions. Under a modulated regime, the resulting PAE is a weighted average across the instantaneous values of the output signal $\mathbf{b}_2$ i.e., the PDF of $\mathbf{b}_2$ acts as the weighting function, in general resulting in different PAE behavior and correspondingly different optimum values for α_r and ϕ. The resulting PAE under modulated conditions is shown in Fig. 5.13 for swept values of the splitting conditions, leading to the selection of two particular configurations for the digital splitter parameters, namely, **P1** ($\alpha_r = 0.5$ and

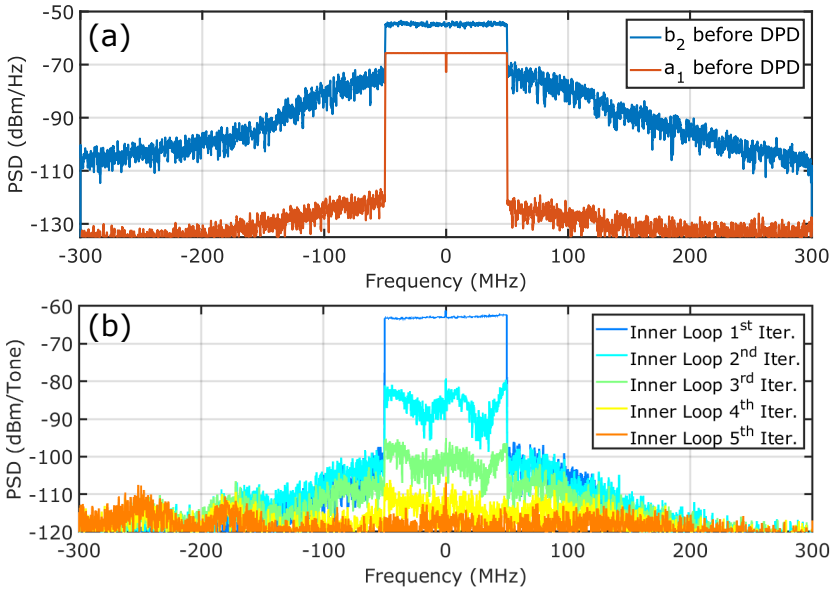

Figure 5.10: DIDPA waves before linearization. (a) Spectra of $\mathbf{b}_2$ and $\mathbf{a}_1$. (b) Spectrum of iterative error $\mathbf{a}_3 - \alpha_r e^{j\phi}\mathbf{a}_1$ across the ILC-based inner loop.

$\phi = -30°$), found when the outer loop in (5.5) is not executed (i.e., without applying DIDPA linearization), and **P2** ($\alpha_r = 0.8$ and $\phi = -30°$), found when both the outer and inner loops are executed (i.e., applying DIDPA linearization).

Then, regardless of how they were found, the input split settings as per **P1** and **P2** are imposed, with and without linearization, to evaluate the global performance of the DIDPA. The extracted FoMs are summarized in Table 5.2, reporting the highest PAE in **P1** if no linearization is applied. On the other hand, when linearization is applied, a slightly higher PAE is obtained for **P2**. The measured dynamic gain and phase characteristics for the two operating points are reported in Figs. 5.14-5.15, while the spectra are shown in Fig. 5.16.

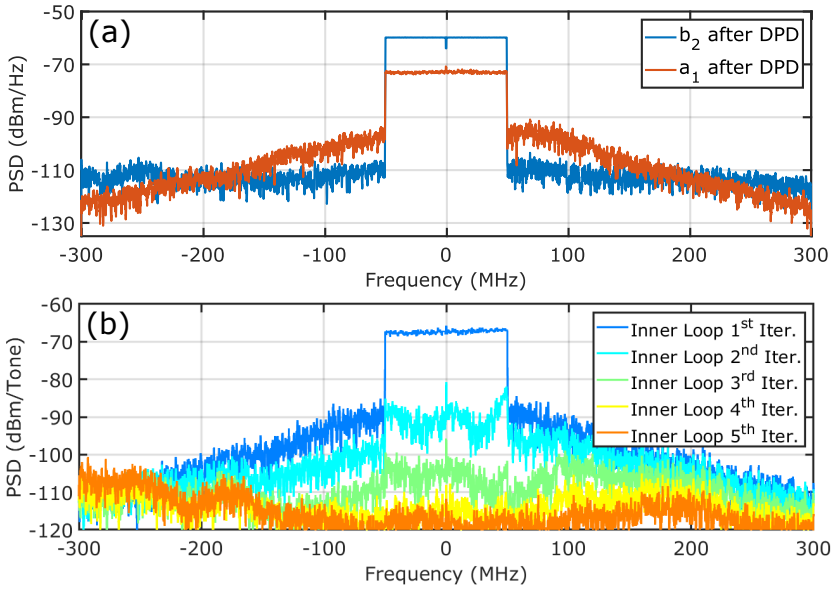

Figure 5.11: DIDPA waves after linearization. (a) Spectra of $\mathbf{b}_2$ and $\mathbf{a}_1$ spectra. (b) Spectrum of iterative error $\mathbf{a}_3 - \alpha_r e^{j\phi}\mathbf{a}_1$ across the ILC-based inner loop.

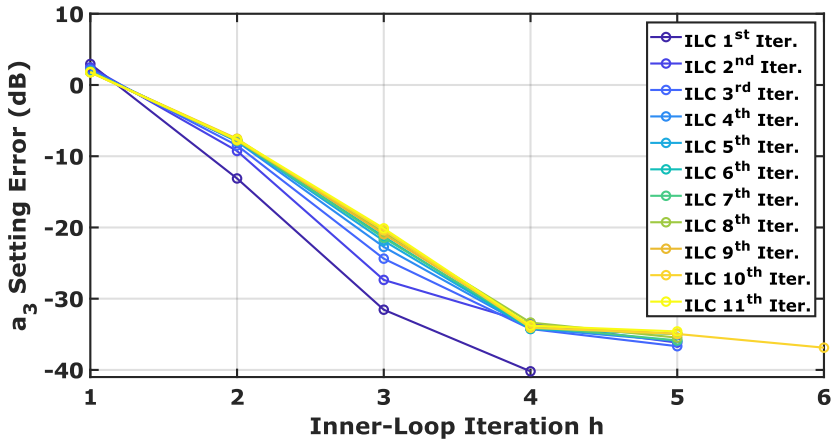

Figure 5.12: Iterative behavior of the NMSE between $\mathbf{a}_3^{(k,h)}$ and $\alpha_r e^{j\phi}\mathbf{a}_1^{(k,h)}$ for dual input emulation (inner loop) and PA linearization (outer loop, color coding in the legend).

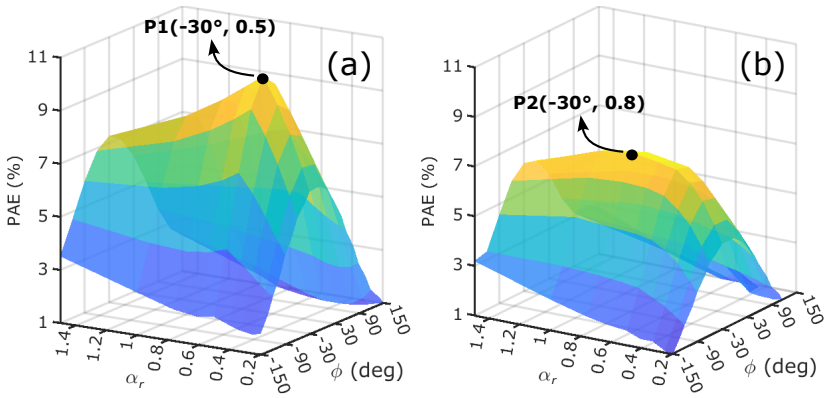

Figure 5.13: PAE under modulated excitation for swept values of the input splitting conditions. (a) Without DIDPA linearization. (b) After DIDPA linearization.

5.6 Quasi-Static Model Optimization Results

5.6.1 Constant Digital Splitter

The first experiment tests the quasi-static-model-based Bayesian optimization (QSM-BO) applied to the total amount of tuning variables offered by the device which implements the constant power splitting ratio version of the digital splitter described in Eq. 5.3 of Sec. 5.3.2 (see also Tab. 5.1). The Iterative behavior of the QSM-BO applied to this 10 tuning variable (10D QSM-BO) is shown in Fig. 5.17. Table 5.3 compares the results of the 10D QSM-BO to a continous-wave-based-BO (CW-BO) on the same variables that maximizes the peak PAE (PAE_{Peak}) of the DIDPA. The PAE estimated using the QSM (PAE_{QSM}) clearly shows that the QSM-BO leads to a better results in terms of estimated efficiency under modulated signal excitation, even if it reaches a minor PAE_{Peak} if compared to the CW-BO. The 10D QSM-BO is then compared to the results of the BO applied to a reduced set of variables: α and ϕ (2D QSM-BO); α, ϕ, $V_{GG}^{A,D}$, $V_{GG}^{A,F}$, $V_{GG}^{M,D}$ and $V_{GG}^{M,F}$ (6D QSM-BO) [127]. The static gain and PAE characteristics extracted in the optimal parameters that are results of the QSM-BOs and the CW-BO are described in Fig. 5.18. The optimal points are tested using mod-

FoM	**P0**	**P1**	**P2**
w/o linearization			
$P_{\mathrm{OUT}}^{\mathrm{rms}}$ (dBm)	25.4	23.2	21.7
PAE (%)	8.5	10.4	9.3
ACPR (dB)	-21.2	-26.3	-29.5
EVM (dB)	-15.7	-19.5	-20.4
w/ linearization			
$P_{\mathrm{OUT}}^{\mathrm{rms}}$ (dBm)	20.1	20.5	20.5
PAE (%)	7.2	7.1	7.4
ACPR (dB)	-48.8	-48.7	-50.7
EVM (dB)	-43.7	-39.2	-43.9

Table 5.2: DIDPA performance under modulated excitation at different input splitting conditions.

	PAE_{QSM} (%)	PAE_{Peak} (%)	P_{max}^{out} (dBm)	P_{RMS}^{out} (dBm)
10D CW-BO (Max Peak PAE)	9.8	23.5	27.9	18.7
10D QSM-BO	11.5	17.5	28.4	19.1

Table 5.3: Comparison between the quasi-static pdf-based estimation for the PAE of the optimized PA targeting maximum peak PAE and targeting the quasi-static pdf-based PAE.

ulated input signal excitation and linearized with the procedure described in Sec. 5.3.3. The linearized dynamic gain and AM-PM characteristics for the tuning parameters found with the QSM-BOs are shown in Fig. 5.19. Tab. 5.4 compares the PAE and linearity FoMs (NMSE and ACPR) of the optimal points described before. It shows an improvement up to 6% with the 10D QSM-BO with respect to the 2D QSM-BO (that correspond to the nominal bias for the Doherty implementation, see Tab. 5.7). The major drawback is represented here by the $\simeq$ 0.3 dB loss in terms of $P_{\mathrm{OUT}}^{\mathrm{rms}}$, since it is not controlled by the QSM-BO.

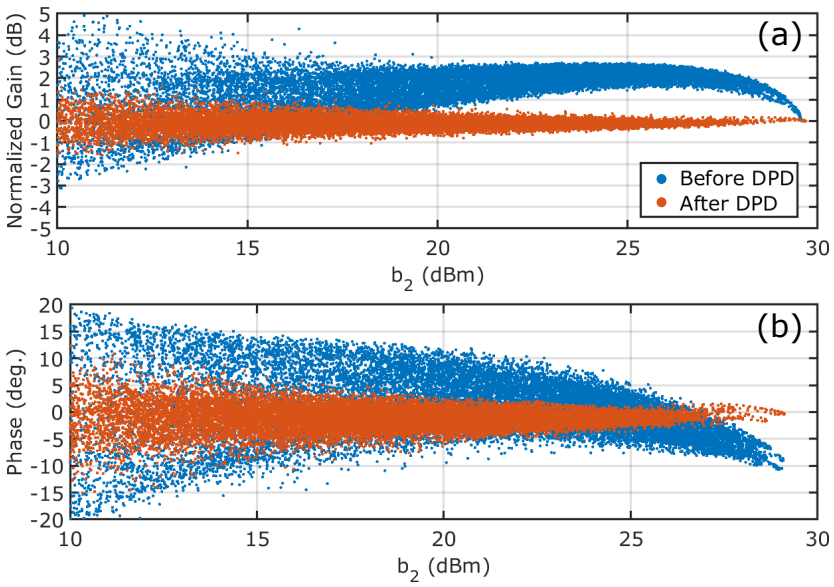

Figure 5.14: Distorted and linearized (a) gain and (b) phase characteristics of the DUT in the optimal point obtained without considering the effect of DPD on PAE (**P1**).

Tuning Method	PAE (%)	P^{out}_{max} (dBm)	P^{out}_{RMS} (dBm)	EVM (dB)	ACPR (dB)
2D QSM-BO (Nominal Bias)	6.8	29.3	20.0	-44.9	-50.1
6D QSM-BO	9.9	29.7	19.9	-37.7	-39.2
10D QSM-BO	12.8	29.0	20.0	-45.7	-50.3
10D CW-BO (Max Peak PAE)	10.9	28.2	18.9	-47.3	-50.3
10D QSM-BO w/ Max-PAE Input Shaping	13.4	29.0	19.7	-48.3	-51.1

Table 5.4: Optimized PA efficiency, power and linearity FoMs evaluated using WB modulated measurements after DPD at the optimal points found running the QSM-BOs and CW-BO.

5.6.2 Static Nonlinear Digital Splitter

The blue dots in Fig. 5.20a represent the P_{out}-PAE data while sweeping the value of α and the magnitude of a_1. To extract the maximum-PAE shaping, the α values have been selected in order to have the maximum PAE for every value of P_{out} (purple crosses in Fig. 5.20a-b). The black line in Fig. 5.20b represents the adopted shaping for the power splitting ratio, based on the logistic function fitting (Eq. 5.4) of the optimal α-$|a_1|$ points. The DIDPA with extracted shaping is tested and linearized using

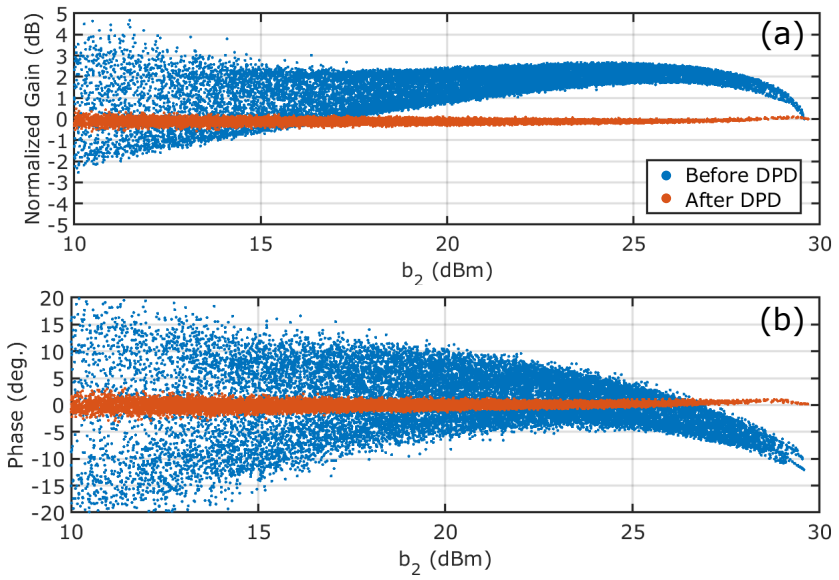

Figure 5.15: Distorted and linearized (a) gain and (b) phase characteristics of the DUT in the optimal point obtained considering the effect of DPD on PAE (P_2).

modulated input signal excitation, Fig.5.21 shows the dynamic gain and AM-PM characteristics of this shaping under this conditions. The last row in Tab. 5.4 highlights the improvement of $\simeq$ 0.8% in terms of overall PAE while compared to the constant input splitter (corresponding to the 10D QSM-BO optimal point), without scarifying any other of the tested FoM. Figure 5.22a shows the relationship among PAE, α and P_{out}, highlighting the adopted shaping (purple dots), the constant power splitting ratio given by the 10D QSM-BO (yellow dots) and for maximum peak PAE (red dots). As shown in Fig. 5.22b, the relationship that has been set by the DIC applying modulated input excitation shows memory effects that distance it from the desired static P_{out}-α relationship, which realizes the maximum PAE. This can be explained by the fact that in this experiment DIC procedure actually set a static relationship between the two inputs a_1 and a_3, which realize the purple curve in Fig. 5.22b only neglecting the DUT dynamic effects. It is conceivable that the performance of the DUT could be improved by setting a dynamic

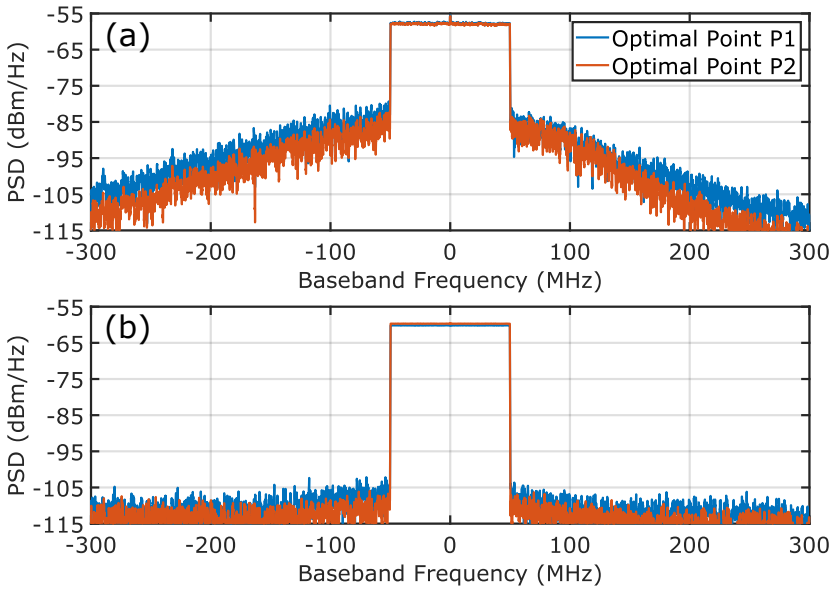

Figure 5.16: Measured spectra of $\mathbf{b}_2$ at input splitting conditions **P1** and **P2** before (a) and after linearization (b).

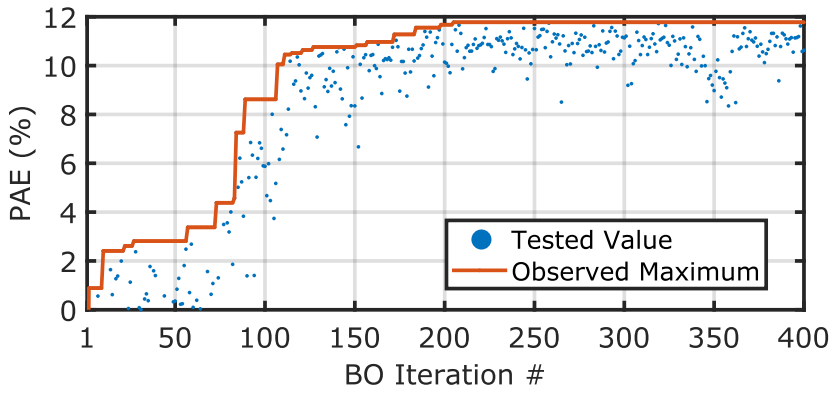

Figure 5.17: Value of the objective function through the iteration of the 10D QSM-BO.

relation between a_1 and a_3, which compensate DUT memory effects and set the desired static α-$P_o ut$ curve. This can be theoretically achieved with the experimental setup and is subject for future works. Figure 5.23 collects and compares the linearized spectra of the cases optimized using QSM-BO with the case shaped to maximize the PAE. With the exception of the 6D QSM-

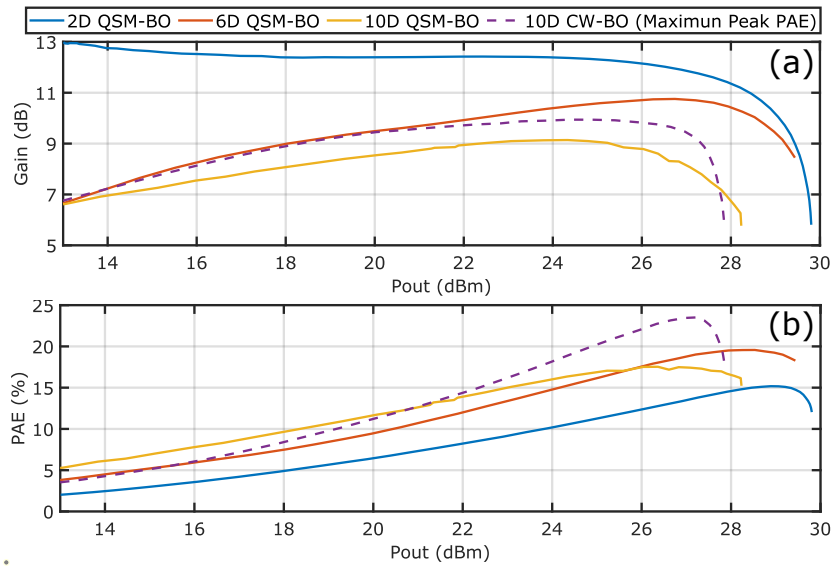

Figure 5.18: Static (a) gain and (b) efficiency characteristics of the optimized PA, while changing the number of tuning variables and optimization type.

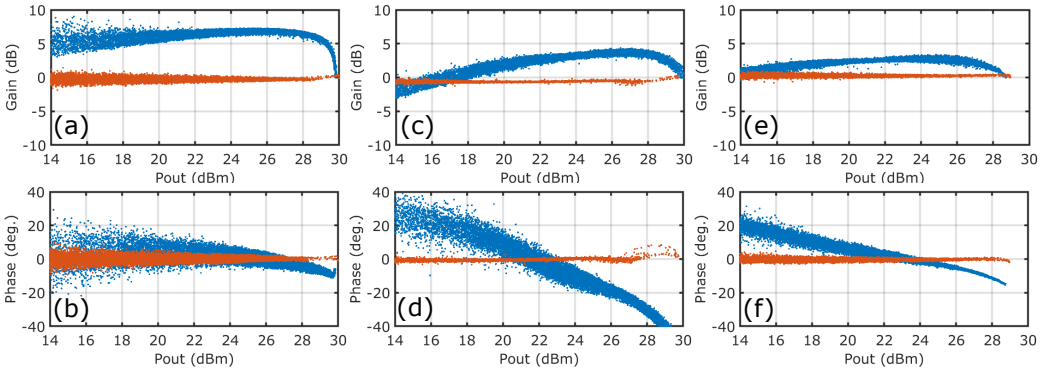

Figure 5.19: Gain and phase characteristics of the before and after linearization (the blue and red lines, respectively) of the DDPA after (a-b) 2 QSM-BO, (c-d) 6 QSM-BO, (e-f) 10 QSM-BO.

BO, which shows a less linearizable PA compared to the other cases, the level of linearity achieved after the DPD is substantially comparable (as assessed in Tab. 5.4).

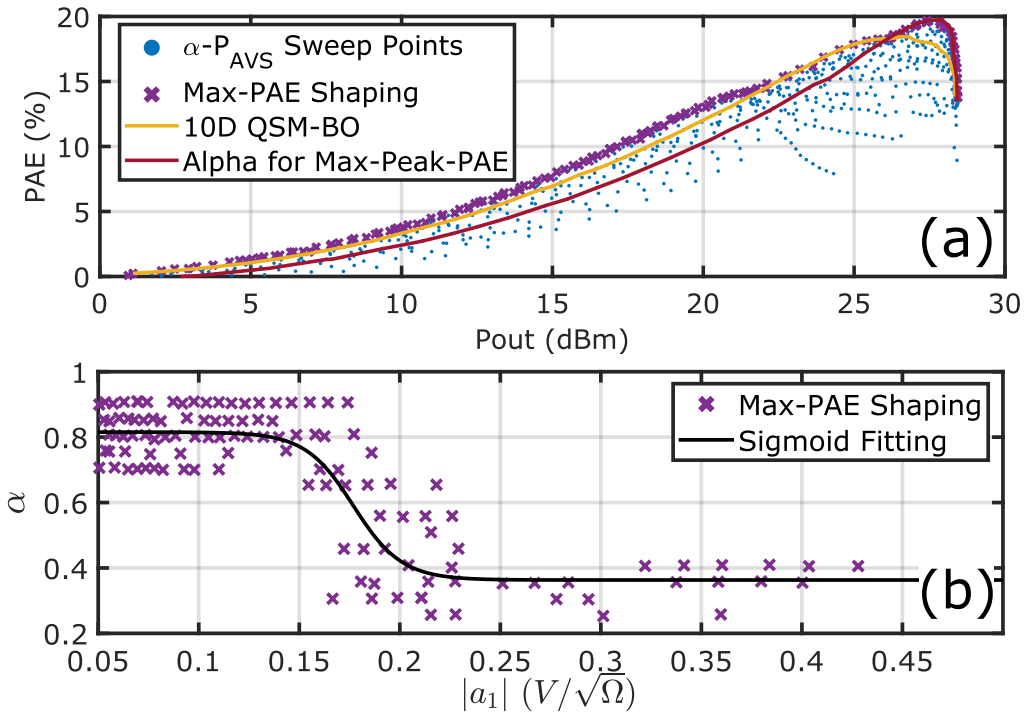

Figure 5.20: (a) PAE values while sweeping α and P_{AVS} of the 10D QSM-BO optimized PA, highlighting maximum PAE envelope. (b) Fitting using logistic function of the extracted shaping.

5.7 BO on Direct Modulated Measurements Results

5.7.1 Constant Digital Splitter

The BO was repeated using direct modulated measurements (Dir-BO) to validate the results of the QSM-BO described in the previous section. The Iterative behavior of the Dir-BO applied to the same 10 tuning variable (10D Dir-BO) is shown in Fig. 5.24. Tab. 5.5 compares the 10D Dir-BO to the results of the BO applied to the reduced sets of variables: α and ϕ (2D Dir-BO); α, ϕ, $V_{GG}^{A,D}$, $V_{GG}^{A,F}$, $V_{GG}^{M,D}$ and $V_{GG}^{M,F}$ (6D Dir-BO) [127]. The linearized dynamic gain and AM-PM characteristics of the compare optimal

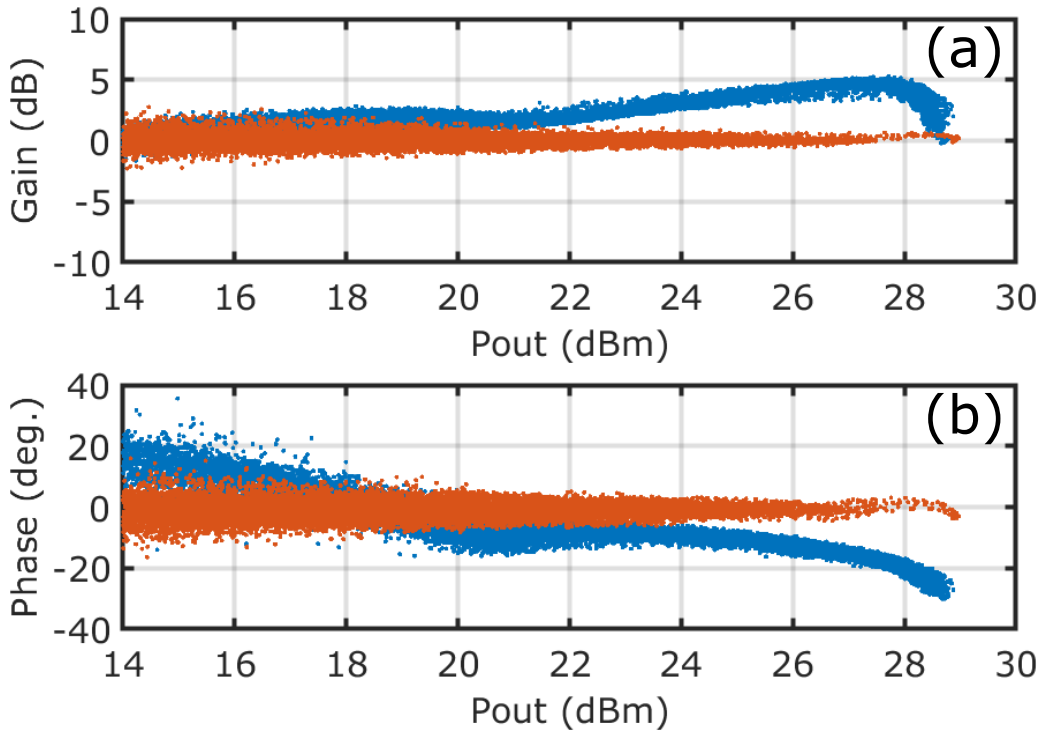

Figure 5.21: (a) Gain and (b) phase characteristics of the before and after linearization (the blue and red lines, respectively) of the max-PAE shaped DDPA.

Tuning Method	PAE (%)	P^{out}_{max} (dBm)	P^{out}_{RMS} (dBm)	EVM (dB)	ACPR (dB)
2D Dir-BO (Nominal Bias)	6.83	29.26	19.96	-44.89	-50.12
6D Dir-BO	9.22	29.95	20.52	-44.72	-49.16
10D Dir-BO	12.59	29.01	19.99	-48.14	-49.93
10D Dir-BO w/ Input Shaping	13.29	20.17	29.25	-45.03	-48.34

Table 5.5: Optimized PA efficiency, power and linearity FoMs evaluated using WB modulated measurements after DPD at the optimal points found running the Dir-BOs.

point found with the Dir-BOs are shown in Fig. 5.25.

5.7.2 Static Nonlinear Digital Splitter

The Dir-BO is applied to the tuning variables related to the shaped power splitter (see Tab. 5.1). Specifically, Dir-BO has been applied to the variable

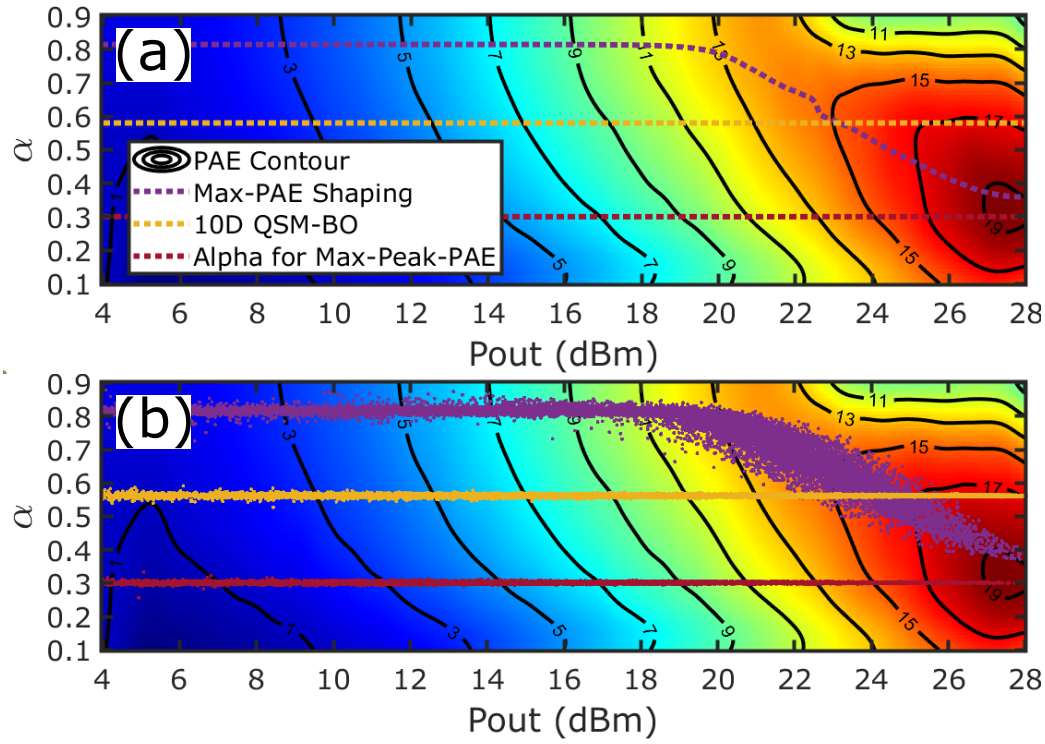

Figure 5.22: Heat-maps representing the PAE-α-P_{out} relationship. (a) α-P_{out} static relationships for the maximum PAE shaping, constant α obtained for QSM-BO, and constant α obtained for maximum peak PAE. (b) α-P_{out} relationships set applying modulated input excitation (after DUT linearization) for the maximum PAE shaping, constant α obtained for QSM-BO, and constant α obtained for maximum peak PAE.

r_i, r_f, and x_0 (d was left to a constant value). The bias-related variables and ϕ are kept constant, as extracted by the 10D Dir-BO. The dynamic gain and AM-PM characteristics of this shaping are shown in Fig. 5.26. Figure 5.27 and Tab. 5.6 compare the different shaping function obtained in this Sec. and in Sec. 5.6.2. It must be highlighted that in the two compared cased also the bias-rated variables were different, due to the different results given by the 10D QSM-BO and the 10D Dir-BO (Tab. 5.7). Figure 5.28 collects and compares the linearized spectra of the cases optimized using Dir-BO with the case shaped to maximize the PAE, it shows that the level of linearity achieved

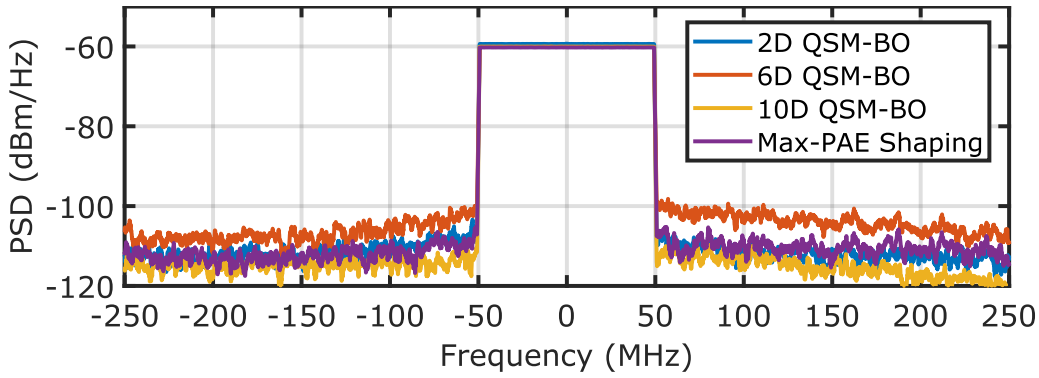

Figure 5.23: Spectra of the output RF signal after linearization at the optimal points found running the QSM-BOs.

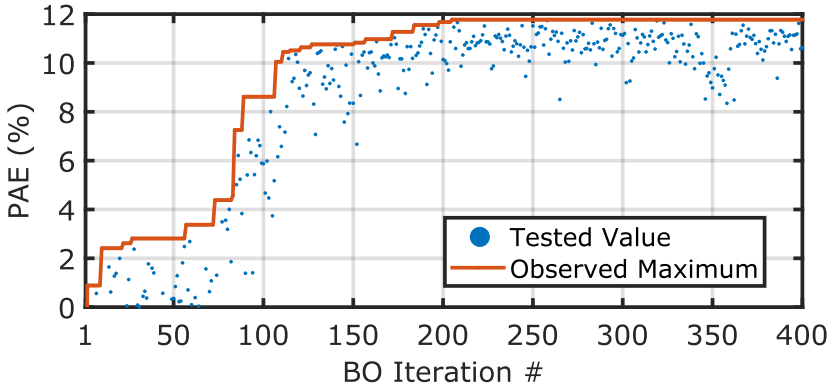

Figure 5.24: Value of the objective function through the iteration of the 10D Dir-BO.

Tuning Method	ϕ (deg.)	r_i	r_f	x_0 ($\frac{V}{\sqrt{\Omega}}$)	d ($\frac{\sqrt{\Omega}}{V}$)
10D QSM-BO w/ Max-PAE Input Shaping	-12	0.48	1.32	0.18	16.7
10D Dir-BO w/ Input Shaping	-17	**0.20**	**1.52**	**0.14**	16.7

Variables that are tuned by the Dir-BO are highlighted in bold.

Table 5.6: Comparison among the shaped-power-splitter-related tuning variables obtained in Sec. 5.6.2 and those obtained using Dir-BO.

after the DPD is substantially comparable among the whole optimal points (as assessed in Tab. 5.5).

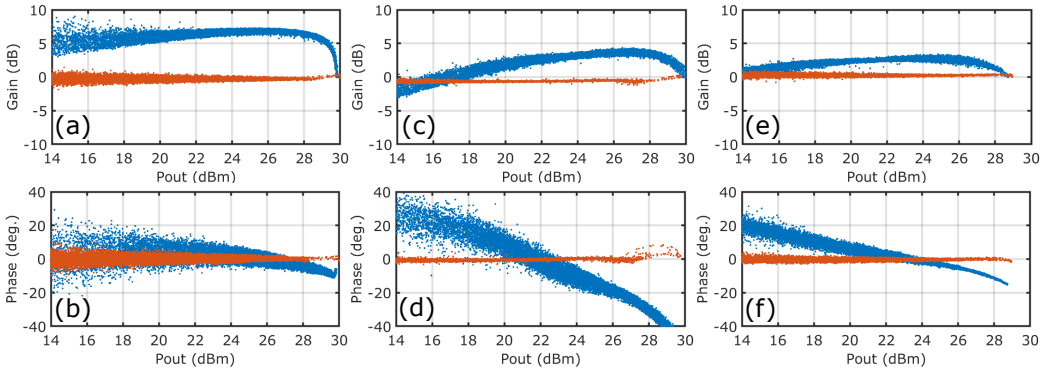

Figure 5.25: Gain and phase characteristics of the before and after linearization (the blue and red lines, respectively) of the DDPA after (a-b) 2D Dir-BO, (c-d) 6D Dir-BO, (e-f) 10D Dir-BO.

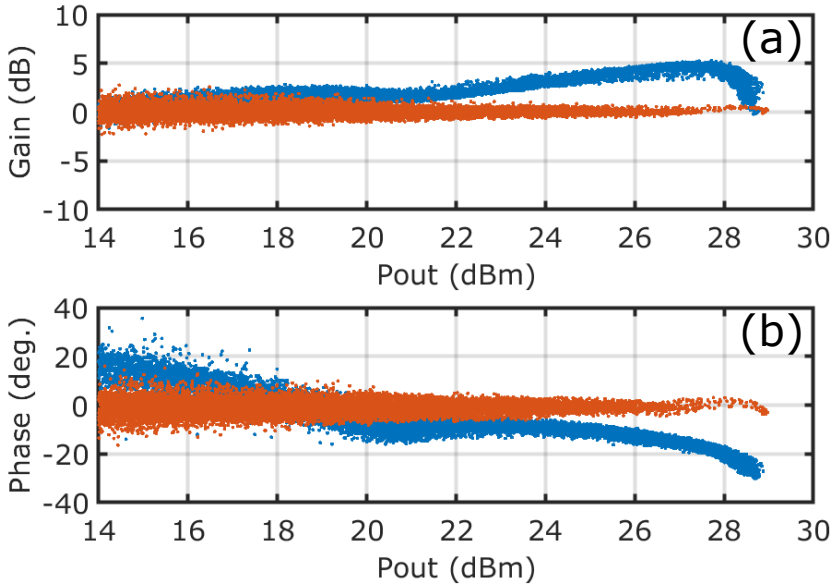

Figure 5.26: (a) Gain and (b) phase characteristics of the before and after linearization (the blue and red lines, respectively) of 10D Dir-BO optimized DDPA with input shaping.

5.8 Achievements

The Chapter describes a methodology aimed at enhancing the performance of a dual-input device in terms of PAE. The possibility given by the

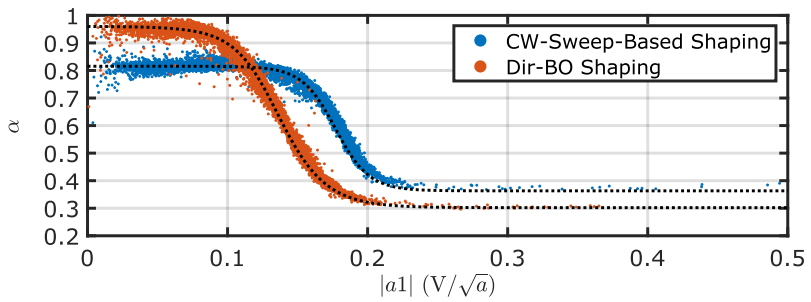

Figure 5.27: Comparison between the Maximum PAE input shaping obtained for the QSM-BO optimized DDPA and the shaping obtained for the Dir-BO optimized PA

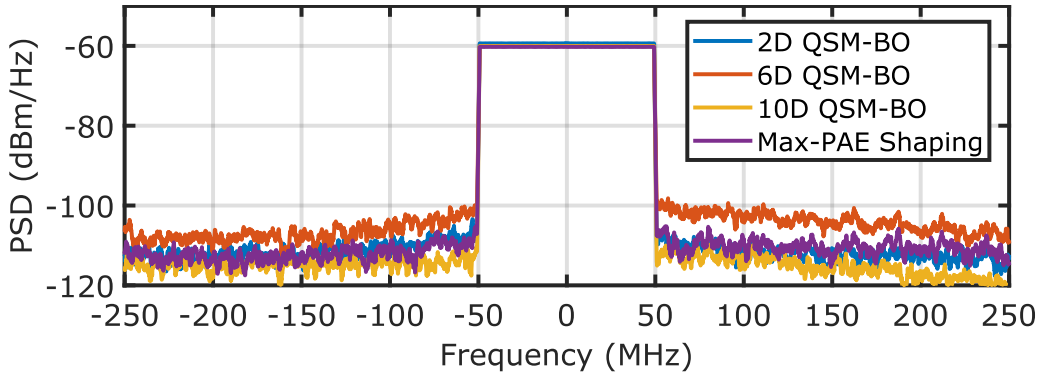

Figure 5.28: Spectra of the output RF signal after linearization at the optimal points found running the Dir-BOs.

DIC procedure and the setup to set an arbitrary relationship between the inputs, alongside with the QSM-BO, leads to an improvement up to 6% PAE, while keeping the same level of linearity as the nominal device (Tab. 5.4). It shows the improvement while maintaining good linearity level after linearization through DPD. The enhancement is achieved by performing a joint optimization of efficiency and linearity, considering the mutual effects of linearization and PAE-maximization throughout the process. The QSM approach, is validated testing the optimization with the a BO which leverage on direct modulated measurements. Specifically, Tables 5.4 and 5.5 indicate no significant differences between the performance of the QSM-BO and those

Tuning Method	2D QSM-BO	6D QSM-BO	10D QSM-BO	10D CW-BO (Max Peak PAE)	2D Dir-BO	6D Dir-BO	10D Dir-BO
α	**0.45**	**0.62**	**0.58**	**0.56**	**0.77**	**0.74**	**0.60**
ϕ (deg.)	**-28**	**7**	**-12**	**-16**	**-39**	**-17**	**-17**
$V_{GG}^{A,D}$ (V)	-2.25	**-2.26**	**-2.08**	**-2.08**	-2.25	**-2.54**	**-2.31**
$V_{GG}^{A,F}$ (V)	-2.00	**-2.56**	**-2.40**	**-2.40**	-2.00	**-2.55**	**-2.71**
$V_{GG}^{M,D}$ (V)	-1.85	**-1.70**	**-1.77**	**-1.77**	-1.85	**-1.83**	**-1.72**
$V_{GG}^{M,F}$ (V)	-1.83	**-2.98**	**-2.56**	**-2.56**	-1.83	**-2.37**	**-2.72**
$V_{DD}^{A,D}$ (V)	20	20	11.6	16.7	20	20	**15.80**
$V_{DD}^{A,F}$ (V)	20	20	17.3	14.5	20	20	**16.76**
$V_{DD}^{M,D}$ (V)	20	20	17.1	9.9	20	20	**17.08**
$V_{DD}^{M,F}$ (V)	20	20	16.0	15.8	20	20	**16.67**

Variables that are tuned by the BOs are highlighted in bold.

Table 5.7: Values of the tuning variables for DIDPA optimization.

obtained using direct modulated measurements and linearization.

Chapter 6

Conclusions and Future Works

6.1 Main Achievements

The aim of the thesis was to analyze the possibility of exploiting the additional degrees of freedom in multi-input architectures to improve their performance in terms of trade-offs among the main figures of merit: linearity, efficiency, and power. The proposed algorithms were tested on three different topologies of multi-input power amplifiers (PAs), each presenting different optimization challenges and objectives. On the PA array, a beam-dependent digital predistortion (BD-DPD) algorithm was tested to enhance the linearity of the system under varying PA load conditions (by varying the beam direction). On the supply-modulated PA (SM-PA), a gradient-based multi-objective optimization (MOO) algorithm was applied to optimize the trade-off between linearity and efficiency of the PA. Finally, a derivative-free algorithm, the Bayesian optimization (BO), was tested on a multi-input load-modulated amplifier, specifically a dual-input Doherty PA (DIDPA). The main research activity of this PhD was carried out at the University of Bologna, in cooperation with the EDM-LAB research group. For the implementation of the measurements and the development of the research described in Chapter 5 the collaboration with the Ferdinand Braun Institut (FBH) and two research periods (of three and six months) spent at the RF

Power Lab research group in Berlin were fundamental. These are the main outcomes the of the thesis:

- An architecture for BD-DPD is introduced, leveraging customized feature-based model reduction for beamformer arrays. The array-level application of feature-based reduction is independent of the number of PAs within the array. This feature-based approach facilitates a low-complexity DPD update for the array, adjusting it based on beam direction and RF power level, without requiring the extraction of a separate DPD coefficient set for each distinct operational scenario. The proposed BD-DPD demonstrates effectiveness in substantially mitigating in-band distortion and out-of-band residual regrowth in the DUT across all evaluated beam directions and PAPR levels.

- A new framework is proposed for generalized DPD of multiple-input single-output (MISO) PA architectures, demonstrated here for the specific case of SM-PA. The proposed MOO technique, based on a surrogate, automates the exploration of linearity-efficiency trade-offs for joint control of RF input and SM. This results in optimal ST for the SM, not identifiable through typical heuristic analysis on CW measurements. Moreover, the framework allows the implementation of dynamic generalized DPD on the SM (instead of static ST) and inherently considers input signal statistics. The achieved operational regimes outperform classical methods for ST not only in terms of the optimized variable, i.e., PAE, but also in terms of linearity for a given RF P_{out}.

- This work introduces a measurement system and methodology capable of measuring and optimizing multi-input devices using wideband (WB) modulated signals at a central frequency of 24 GHz. An iterative dual-input control (DIC) method is presented to control the relationship between the controlled ports, correcting preamplifier nonlinearities. The calibrated system is then employed at millimeter-wave frequencies to explore the performance of a DIDPA under various simulated input

splitting conditions.

- Chapter 5 outlines a method aimed at enhancing the performance of a dual-input device in terms of PAE, while maintaining good levels of linearity after linearization through DPD. The improvement is achieved by jointly optimizing efficiency and linearity, considering the mutual effects of linearization and PAE maximization throughout the process. The ability provided by the DIC procedure and the setup to establish an arbitrary relationship between inputs, along with QSM-BO, leads to a 6% PAE improvement while maintaining the same level of linearity as the nominal device. The QSM approach is validated by testing the optimization with a BO leveraging direct modulated measurements. Specifically, the results indicate no significant differences between the performance of QSM-BO and those obtained using direct modulated measurements and linearization.

6.2 Possible Topics for Future Work

For each architecture tested it is possible to think about a series of tests not explored throughout the thesis. In this context, the following are potential future works that could extend and enhance the findings presented in this thesis:

- Considering the work on the PA array described in Chapter 2, The beam-dependent DPD (BD-DPD) pre-training time can be reduced by implementing a more efficient design of experiment for pre-training set evaluation. By using a latin hypercube sampling of BD-DPD variable space composed by the beam direction and the input signal peak to average power ratio (PAPR). Moreover, the methodology can be applied including a 4-way MMIC PA in the transmitter chain to study chip-level EM coupling.

- Considering the work on the SM-PA described in Chapter 3, the method

feasibility and the actual optimal achieved are limited by the fidelity of the SuMo. Although a dual-input MP formulation was chosen in this work, more accurate modeling approaches could be adopted based on the application, ultimately reducing discrepancies between simulations and measurements and enhancing optimization reliability. While adapted in this case for PA performance improvement, the proposed surrogate-based MOO framework could be a valuable tool for optimizing the global PA transmitter or analyzing critical compromises like SM slew-rate limitations. Future work also involves application to wider modulation bandwidths and alternative PA topologies.

- Considering the on-wafer multi-port WB measurement setup exploited in Chapter 5, it is proven that the system produces stable measurements of good quality and that the correct targeted signals can be presented to the DUT within a limited time frame. Overall, these multiport measurements provide a proof of concept for the WB VNA-based configuration that will be expanded in the future in terms of bandwidth and the number of ports.

- As shown in Fig.5.22b of Chapter 5, the relationship set by the DIC applying modulated input excitation exhibits memory effects that deviate it from the desired static P_{out}-α relationship, achieving maximum PAE. This can be explained by the fact that in this experiment, the DIC procedure effectively establishes a static relationship between the two inputs a_1 and a_3, representing only the purple curve in Fig.5.22b, neglecting the dynamic effects of the DUT. It is conceivable that DUT performance can be improved by setting a dynamic relationship between a_1 and a_3 that compensates for the memory effects of the DUT and enforces the desired static α-P_{out} curve. This can theoretically be achieved with the experimental setup and is subject to future work.

6.3 List of Publications

6.3.1 International Journals

1. M. Mengozzi, G. P. Gibiino, A. M. Angelotti, C. Florian, A. Santarelli: *Beam-Dependent Active Array Linearization by Global Feature-Based Machine Learning*, published in "IEEE Microwave and Wireless Technology Letters", 2023.

2. M. Mengozzi, G. P. Gibiino, A. M. Angelotti, C. Florian, A. Santarelli, P. Colantonio: *Automatic Optimization of Input Split and Bias Voltage in Digitally Controlled Dual-Input Doherty RF PAs*, "ENERGIES", 2022, 15, Article number: 4892, pp. 1 - 16, 2022.

3. M. Mengozzi, A. M. Angelotti, G. P. Gibiino, C. Florian and A. Santarelli: *"Joint Dual-Input Digital Predistortion of Supply-Modulated RF PA by Surrogate-Based Multi-Objective Optimization*, "IEEE Transactions on Microwave Theory and Techniques," 2022.

4. M. Mengozzi, G. P. Gibiino, A. M. Angelotti, C. Florian, A. Santarelli: *GaN power amplifier digital predistortion by multi-objective optimization for maximum RF output power*, "MDPI-ELECTRONICS," 2021.

5. C. Schulze, M. Mengozzi, G. P. Gibiino, A. M. Angelotti, C. Florian, A. Santarelli, W. Heinrich, O. Bengtsson: *A VNA-Based Wideband Measurement System for Large-Signal Characterization of Multiport Circuitsn*, "IEEE Transactions on Microwave Theory and Techniques," 2023.

6.3.2 International Conferences

1. M. Mengozzi, A. M. Angelotti, G. P. Gibiino, C. Schulze, C. Florian, P. Colantonio, O. Bengtsson, A. Santarelli: *Wideband Automated Tuning of Ka-Band Dual Input Doherty MMIC PA using Bayesian opti-*

mization, presented at "18th European Microwave Integrated Circuits Conference," 2023.

2. M. Mengozzi, G. P. Gibiino, A. M. Angelotti, C. Schulze C. Florian, P. Colantonio, O. Bengtsson, A. Santarelli: *Wideband Automated Tuning of Ka-Band Dual Input Doherty MMIC PA using Bayesian Optimization*, presented at "101st ARFTG Microwave Measurement Conference," 2023.

3. M. Mengozzi, G. P. Gibiino, A. M. Angelotti, C. Florian, A. Santarelli: *Beam-Dependent Active Array Linearization by Global Feature-Based Machine Learning*, presented at "International Microwave Symposium 2023," 2023.

4. M. Mengozzi, G. P. Gibiino, A. M. Angelotti, C. Florian, A. Santarelli: *Over-the-Air Digital Predistortion of 5G FR2 Beamformer Array by exploiting Linear Response Compensation*, "International Microwave Symposium 2022," 2022.

5. M. Mengozzi, G. P. Gibiino, A. M. Angelotti, C. Florian, A. Santarelli: *Supply-Modulated PA Performance Enhancement by Joint Optimization of RF Input and Supply Control*, "Asia Pacific Microwave Conference 2020," 2020.

6. N. Lowenthal, G. P. Gibiino, C. Tamburini, M. Mengozzi, A. Romani, M. Crescentini, P. A. Traverso: *Automated Measurement Set-Up for the Electro-Mechanical Characterization of Piezoelectric Harvesters*, "2023 IEEE International Workshop on Metrology for Automotive," 2023.

Bibliography

[1] A. S. Tehrani, H. Cao, S. Afsardoost, T. Eriksson, M. Isaksson, and C. Fager, "A Comparative analysis of the complexity/accuracy tradeoff in power amplifier behavioral models," *IEEE Trans. Microw. Theory Techn.*, vol. 58, no. 6, pp. 1510–1520, 2010.

[2] Z. Wang, "Demystifying envelope tracking: Use for high-efficiency power amplifiers for 4g and beyond," *IEEE Microwave Magazine*, vol. 16, no. 3, pp. 106–129, 2015.

[3] H. Cao, H. M. Nemati, A. S. Tehrani, T. Eriksson, and C. Fager, "Digital predistortion for high efficiency power amplifier architectures using a dual-input modeling approach," *IEEE Trans. Microw. Theory Techn.*, vol. 60, no. 2, pp. 361–369, 2012.

[4] R. Darraji, F. M. Ghannouchi, and O. Hammi, "A dual-input digitally driven Doherty amplifier architecture for performance enhancement of Doherty transmitters," *IEEE Trans. Microw. Theory Techn.*, vol. 59, no. 5, pp. 1284–1293, 2011.

[5] T. Barton, "Not just a phase: Outphasing power amplifiers," *IEEE Microw. Mag.*, vol. 17, no. 2, pp. 18–31, 2016.

[6] T. Cappello, P. Pednekar, C. Florian, S. Cripps, Z. Popovic, and T. W. Barton, "Supply-and load-modulated balanced amplifier for efficient broadband 5G base stations," *IEEE Trans. Microw. Theory Techn.*, vol. 67, no. 7, pp. 3122–3133, 2019.

[7] J. Hoversten, S. Schafer, M. Roberg, M. Norris, D. Maksimovic, and Z. Popovic, "Codesign of PA, supply, and signal processing for linear supply-modulated RF transmitters," *IEEE Trans. Microw. Theory Techn.*, vol. 60, no. 6, pp. 2010–2020, 2012.

[8] M. Marchetti, M. J. Pelk, K. Buisman, W. E. Neo, M. Spirito, and L. C. de Vreede, "Active harmonic load-pull with realistic wideband communications signals," *IEEE Trans. Microw. Theory Techn.*, vol. 56, no. 12, pp. 2979–2988, 2008.

[9] A. M. Angelotti, G. P. Gibiino, T. S. Nielsen, D. Schreurs, and A. Santarelli, "Wideband active load-pull by device output match compensation using a vector network analyzer," *IEEE Trans. Microw. Theory Techn.*, vol. 69, no. 1, pp. 874–886, 2021.

[10] D. Saffar, N. Boulejfen, F. M. Ghannouchi, A. Gharsallah, and M. Helaoui, "Behavioral modeling of MIMO nonlinear systems with multivariable polynomials," *IEEE Trans. Microw. Theory Techn.*, vol. 59, no. 11, pp. 2994–3003, 2011.

[11] S. Amin, P. N. Landin, P. Händel, and D. Rönnow, "Behavioral modeling and linearization of crosstalk and memory effects in RF MIMO transmitters," *IEEE Trans. Microw. Theory Techn.*, vol. 62, no. 4, pp. 810–823, 2014.

[12] Z. A. Khan, E. Zenteno, P. Händel, and M. Isaksson, "Digital predistortion for joint mitigation of I/Q imbalance and MIMO power amplifier distortion," *IEEE Trans. Microw. Theory Techn.*, vol. 65, no. 1, pp. 322–333, 2016.

[13] K. Hausmair, P. N. Landin, U. Gustavsson, C. Fager, and T. Eriksson, "Digital predistortion for multi-antenna transmitters affected by antenna crosstalk," *IEEE Trans. Microw. Theory Techn.*, vol. 66, no. 3, pp. 1524–1535, 2017.

[14] A. Brihuega *et al.*, "Piecewise digital predistortion for mmWave active antenna arrays: Algorithms and measurements," *IEEE Trans. Microw. Theory Techn.*, vol. 68, no. 9, pp. 4000–4017, 2020.

[15] H. Zargar, A. Banai, and J. C. Pedro, "A new double input-double output complex envelope amplifier behavioral model taking into account source and load mismatch effects," *IEEE Trans. Microw. Theory Techn.*, vol. 63, no. 2, pp. 766–774, 2015.

[16] G. P. Gibiino, K. Łukasik, P. Barmuta, A. Santarelli, D. Schreurs, and F. Filicori, "A two-port nonlinear dynamic behavioral model of RF PAs subject to wideband load modulation," *IEEE Trans. Microw. Theory Techn.*, vol. 66, no. 2, pp. 831–844, 2017.

[17] G. P. Gibiino, G. Avolio, D. Schreurs, A. Santarelli, and F. Filicori, "A three-port nonlinear dynamic behavioral model for supply-modulated rf pas," *IEEE Trans. Microw. Theory Techn.*, vol. 64, no. 1, pp. 133–147, 2015.

[18] F. F. Tafuri, D. Sira, T. S. Nielsen, O. K. Jensen, J. H. Mikkelsen, and T. Larsen, "Memory models for behavioral modeling and digital predistortion of envelope tracking power amplifiers," *Microprocessors and Microsystems*, vol. 39, no. 8, pp. 879–888, 2015.

[19] S. Sharma and N. G. Constantin, "Nonlinear three-port representation of pas for embedded self-calibration of envelope-dependent dynamic biasing implementations," *IEEE Access*, vol. 7, pp. 172 796–172 815, 2019.

[20] P. L. Gilabert, G. Montoro, D. Vegas, N. Ruiz, and J. A. García, "Digital predistorters go multidimensional: DPD for concurrent multiband envelope tracking and outphasing power amplifiers," *IEEE Microw. Mag.*, vol. 20, no. 5, pp. 50–61, 2019.

[21] D. Rönnow, "pth-order inverse of the Volterra series for multiple-input multiple-output non-linear dynamic systems," *IET Circ., Dev. Syst.*, vol. 12, no. 4, pp. 403–412, 2018.

[22] X. Wang, Y. Li, C. Yu, W. Hong, and A. Zhu, "Digital predistortion of 5G massive MIMO wireless transmitters based on indirect identification of power amplifier behavior with OTA tests," *IEEE Trans. Microw. Theory Techn.*, vol. 68, no. 1, pp. 316–328, 2019.

[23] J. C. Pedro and N. B. Carvalho, "Designing band-pass multisine excitations for microwave behavioral model identification," *IEEE MTT-S International Microwave Symposium Digest*, vol. 2, pp. 791–794, 2004.

[24] K. A. Remley, D. F. Williams, D. M. Schreurs, and J. Wood, "Simplifying and interpreting two-tone measurements," *IEEE Transactions on Microwave Theory and Techniques*, vol. 52, no. 11, pp. 2576–2584, 2004.

[25] R. G. Meyer, M. J. Shensa, and R. Eschenbach, "Cross Modulation and Intermodulation in Amplifiers at High Frequencies," *IEEE Journal of Solid-State Circuits*, vol. 7, no. 1, pp. 16–23, 1972.

[26] N. Carvalho, K. Remley, D. Schreurs, and K. Gard, "Multisine signals for wireless system test and design," *IEEE Microwave Magazine*, vol. 9, no. 3, pp. 122–138, 2008.

[27] Y. Rolain, M. Zyari, E. Van Nechel, and G. Vandersteen, "A measurement-based error-vector-magnitude model to assess non linearity at the system level," in *2017 IEEE MTT-S International Microwave Symposium (IMS)*, 2017, pp. 1429–1432.

[28] A. M. Angelotti, G. P. Gibiino, C. Florian, and A. Santarelli, "Broadband error vector magnitude characterization of a gan power amplifier using a vector network analyzer," in *IEEE/MTT-S Int. Microw. Symp. Dig.*, 2020, pp. 747–750.

[29] M. H. Fadhel M. Ghannouchi, Oualid Hammi, *Behavioral Modeling and Predistortion of Wideband Wireless Transmitters.* Wiley, 2015.

[30] A. Zhu, J. C. Pedro, and T. J. Brazil, "Dynamic deviation reduction-based Volterra behavioral modeling of RF power amplifiers," *IEEE Transactions on Microwave Theory and Techniques*, vol. 54, no. 12, pp. 4323–4332, 2006.

[31] M. Isaksson and D. Rönnow, "A Kautz-Volterra behavioral model for RF power amplifiers," *IEEE MTT-S International Microwave Symposium Digest*, pp. 485–488, 2006.

[32] J. Chani-Cahuana, P. N. Landin, C. Fager, and T. Eriksson, "Iterative learning control for RF power amplifier linearization," *IEEE Trans. Microw. Theory Techn.*, vol. 64, no. 9, pp. 2778–2789, 2016.

[33] A. Brihuega, M. Turunen, L. Anttila, T. Eriksson, and M. Valkama, "On the power and beam dependency of load modulation in mmwave active antenna arrays," in *Proc. European Microw. Conf.*, 2021, pp. 680–683.

[34] E. Ng, Y. Beltagy, G. Scarlato, A. Ben Ayed, P. Mitran, and S. Boumaiza, "Digital predistortion of millimeter-wave RF beamforming arrays using low number of steering angle-dependent coefficient sets," *IEEE Trans. Microw. Theory Techn.*, vol. 67, no. 11, pp. 4479–4492, 2019.

[35] M. Mengozzi, G. P. Gibiino, A. M. Angelotti, C. Florian, and A. Santarelli, "Over-the-air digital predistortion of 5g fr2 beamformer array by exploiting linear response compensation," in *IEEE/MTT-S Int. Microw. Symp. Dig*, 2022, pp. 394–397.

[36] X. Liu *et al.*, "Beam-oriented digital predistortion for 5g massive mimo hybrid beamforming transmitters," *IEEE Trans. Microw. Theory Techn.*, vol. 66, no. 7, pp. 3419–3432, 2018.

[37] X. Wang, Y. Li, H. Yin, C. Yu, Z. Yu, W. Hong, and A. Zhu, "Digital predistortion of 5g multiuser mimo transmitters using low-dimensional feature-based model generation," *IEEE Trans. Microw. Theory Techn.*, vol. 70, no. 3, pp. 1509–1520, 2022.

[38] K. Hausmair *et al.*, "Prediction of Nonlinear Distortion in Wideband Active Antenna Arrays," *IEEE Trans. Microw. Theory Techn.*, vol. 65, no. 11, pp. 4550–4563, 2017.

[39] W. Chen, G. Lv, X. Liu, D. Wang, and F. M. Ghannouchi, "Doherty pas for 5g massive mimo: Energy-efficient integrated dpa mmics for sub-6-ghz and mm-wave 5g massive mimo systems," *IEEE Microwave Magazine*, vol. 21, no. 5, pp. 78–93, 2020.

[40] A. Piacibello, R. Giofrè, R. Quaglia, R. Figueiredo, N. Carvalho, P. Colantonio, V. Valenta, and V. Camarchia, "A 5-w gan doherty amplifier for ka-band satellite downlink with 4-ghz bandwidth and 17-db npr," *IEEE Microwave and Wireless Components Letters*, 2022.

[41] W. Hallberg, D. Nopchinda, C. Fager, and K. Buisman, "Emulation of doherty amplifiers using single-amplifier load–pull measurements," *IEEE Microwave and Wireless Components Letters*, vol. 30, no. 1, pp. 47–49, 2019.

[42] K. Freiberger, M. Wolkerstorfer, H. Enzinger, and C. Vogel, "Digital predistorter identification based on constrained multi-objective optimization of WLAN standard performance metrics," in *Proc. IEEE Int. Symp. Circ. Syst.*, 2015, pp. 862–865.

[43] L. Li, A. Ghazi, J. Boutellier, L. Anttila, M. Valkama, and S. S. Bhattacharyya, "Evolutionary multiobjective optimization for digital predistortion architectures," in *International Conference on Cognitive Radio Oriented Wireless Networks*, 2016, pp. 498–510.

[44] C. Kantana, R. Ma, M. Benosman, and Y. Komatsuzaki, "A hybrid heuristic search control assisted optimization of dual-input doherty power amplifier," in *Proc. European Microwave Conference 2021*, 2022, pp. 126–129.

[45] T. Wang, W. Li, R. Quaglia, and P. L. Gilabert, "Machine-learning assisted optimisation of free-parameters of a dual-input power amplifier for wideband applications," *Sensors*, vol. 21, no. 8, 2021. [Online]. Available: https://www.mdpi.com/1424-8220/21/8/2831

[46] W. Li, A. Bogusz, J. Lees, R. Quaglia, S. Cripps, G. Montoro, and P. L. Gilabert, "Performance modeling and shaping function extraction for dual-input load modulated power amplifiers," in *2023 IEEE/MTT-S International Microwave Symposium - IMS 2023*, 2023, pp. 203–206.

[47] J. Peng, S. He, W. Shi, T. Yao, J. Wu, and J. Wang, "Adaptive signal separation for dual-input doherty power amplifier," *IEEE Transactions on Microwave Theory and Techniques*, vol. 68, no. 1, pp. 121–131, 2020.

[48] H. Cao, J. Qureshi, T. Eriksson, C. Fager, and L. de Vreede, "Digital predistortion for dual-input doherty amplifiers," in *2012 IEEE Topical Conference on Power Amplifiers for Wireless and Radio Applications*, 2012, pp. 45–48.

[49] W. Li, G. Montoro, W. Thompson, K. Chuang, and P. L. Gilabert, "Digital shaping and linearization of a dual-input load-modulated balanced amplifier," in *2023 International Workshop on Integrated Nonlinear Microwave and Millimetre-Wave Circuits (INMMIC)*, 2023, pp. 1–3.

[50] J. C. Cahuana, P. Landin, D. Gustafsson, C. Fager, and T. Eriksson, "Linearization of dual-input doherty power amplifiers," in *2014 International Workshop on Integrated Nonlinear Microwave and Millimetre-wave Circuits (INMMiC)*, 2014, pp. 1–3.

[51] E. Guillena, W. Li, P. L. Gilabert, and G. Montoro, "Prediction of the optimal phase shift between control signals in dual-input power amplifiers," in *2020 International Workshop on Integrated Nonlinear Microwave and Millimetre-Wave Circuits (INMMiC)*, 2020, pp. 1–3.

[52] W. Li, G. Montoro, and P. L. Gilabert, "Digital linearization of wideband envelope tracking power amplifiers for mobile terminals," *IEEE Transactions on Microwave Theory and Techniques*, vol. 71, no. 1, pp. 48–58, 2023.

[53] R. Ma *et al.*, "Machine-learning based digital doherty power amplifier," in *Proc. IEEE Int. Symp. RF Int. Tech.*, 2018, pp. 1–3.

[54] C. Kantana, M. Benosman, R. Ma, and Y. Komatsuzaki, "A system approach for efficiency enhancement and linearization technique of dual-input doherty power amplifier," *IEEE Journal of Microwaves*, vol. 3, no. 1, pp. 115–133, 2023.

[55] C. Kantana, "System Approach for Optimizing a Low-Complexity Digital Predistortion Model for RF Power Amplifier Linearization," Theses, Universite Paris-Est, Dec. 2021. [Online]. Available: https://theses.hal.science/tel-03606606

[56] M. Mengozzi, G. P. Gibiino, A. M. Angelotti, C. Florian, and A. Santarelli, "Beam-dependent active array linearization by global feature-based machine learning," *IEEE Microwave and Wireless Technology Letters*, vol. 33, no. 6, pp. 895–898, 2023.

[57] Y. Li, X. Wang, and A. Zhu, "Complexity-reduced model adaptation for digital predistortion of RF power amplifiers with pretraining-based feature extraction," *IEEE Trans. Microw. Theory Techn.*, vol. 69, no. 3, pp. 1780–1790, 2021.

[58] P. Barmuta, G. P. Gibiino, F. Ferranti, A. Lewandowski, and D. M.-P. Schreurs, "Design of experiments using centroidal voronoi tessellation,"

IEEE Trans. Microw. Theory Techn., vol. 64, no. 11, pp. 3965–3973, 2016.

[59] D. Morgan, Z. Ma, J. Kim, M. Zierdt, and J. Pastalan, "A generalized memory polynomial model for digital predistortion of RF power amplifiers," *IEEE Trans. Signal Process.*, vol. 54, no. 10, pp. 3852–3860, 2006.

[60] L. Li, A. Ghazi, J. Boutellier, L. Anttila, M. Valkama, and S. S. Bhattacharyya, "Design space exploration and constrained multiobjective optimization for digital predistortion systems," in *Proc. IEEE Int. Conf. App. Sys., Arch. Proc.*, 2016, pp. 182–185.

[61] M. Mengozzi, G. P. Gibiino, A. M. Angelotti, C. Florian, and A. Santarelli, "Gan power amplifier digital predistortion by multi-objective optimization for maximum rf output power," *Electronics*, vol. 10, no. 3, 2021. [Online]. Available: https://www.mdpi.com/2079-9292/10/3/244

[62] J. Barkate *et al.*, "Fast, simultaneous optimization of power amplifier input power and load impedance for power-added efficiency and adjacent-channel power ratio using the power smith tube," *IEEE Trans. Aerosp. Electron. Syst.*, vol. 52, no. 2, pp. 928–937, 2016.

[63] P. Chen, J. Xia, B. M. Merrick, and T. J. Brazil, "Multiobjective Bayesian optimization for active load modulation in a broadband 20-W GaN Doherty power amplifier design," *IEEE Trans. Microw. Theory Techn.*, vol. 65, no. 3, pp. 860–871, 2017.

[64] S. Niu, A. Koushik, R. Ma, K. H. Teo, S. Shinjo, and Y. Komatsuzaki, "Stochastically approximated multiobjective optimization of dual input digital Doherty power amplifier," in *Proc. IEEE Int. Workshop Comp. Intell. App.*, 2017, pp. 147–152.

[65] C.-H. Chen *et al.*, "Circuit-Simulation-Based Design Optimization of 3.5 GHz Doherty Power Amplifier via Multi-Objective Evolutionary Algorithm and Unified Optimization Framework," in *Proc. IEEE Int. Symp. RF Int. Tech.* IEEE, 2020, pp. 76–78.

[66] N. Knudde *et al.*, "Data-efficient bayesian optimization with constraints for power amplifier design," in *Proc. IEEE MTT-S Int. Conf. Num. Electromag. Multiphys. Modeling Optim.*, 2018, pp. 1–3.

[67] T. Cappello, C. Florian, D. Niessen, R. P. Paganelli, S. Schafer, and Z. Popovic, "Efficient X-band transmitter with integrated GaN power amplifier and supply modulator," *IEEE Trans. Microw. Theory Techn.*, vol. 67, no. 4, pp. 1601–1614, 2019.

[68] A. Zhu, P. J. Draxler, C. Hsia, T. J. Brazil, D. F. Kimball, and P. M. Asbeck, "Digital predistortion for envelope-tracking power amplifiers using decomposed piecewise Volterra series," *IEEE Trans. Microw. Theory Techn.*, vol. 56, no. 10, pp. 2237–2247, 2008.

[69] P. L. Gilabert and G. Montoro, "3-D distributed memory polynomial behavioral model for concurrent dual-band envelope tracking power amplifier linearization," *IEEE Trans. Microw. Theory Techn.*, vol. 63, no. 2, pp. 638–648, 2015.

[70] G. P. Gibiino, A. Santarelli, D. Schreurs, and F. Filicori, "Two-input nonlinear dynamic model inversion for the linearization of envelope-tracking RF PAs," *IEEE Microw. Wirel. Compon. Lett.*, vol. 27, no. 1, pp. 79–81, 2016.

[71] N. Wolff, W. Heinrich, and O. Bengtsson, "A novel model for digital predistortion of discrete level supply-modulated rf power amplifiers," *IEEE Microw. Wirel. Compon. Lett.*, vol. 26, no. 2, pp. 146–148, 2016.

[72] P. Bronders, J. Lataire, T. Coppens, G. Pailloncy, S. Gustafsson, Y. Rolain, and G. Vandersteen, "Precompensation of supply dynamics of

dynamic power supply transmitters using a linear parameter-varying model," *IEEE Transactions on Microwave Theory and Techniques*, vol. 67, no. 1, pp. 278–287, 2019.

[73] M. Mengozzi, A. M. Angelotti, G. P. Gibiino, C. Florian, and A. Santarelli, "Joint dual-input digital predistortion of supply-modulated rf pa by surrogate-based multi-objective optimization," *IEEE Transactions on Microwave Theory and Techniques*, vol. 70, no. 1, pp. 35–49, 2022.

[74] M. Mengozzi, G. P. Gibiino, A. M. Angelotti, C. Florian, and A. Santarelli, "Supply-Modulated PA Performance Enhancement by Joint Optimization of RF Input and Supply Control," in *Proc. IEEE Asia-Pacific Microw. Conf.*, 2020, pp. 585–587.

[75] J. Chani-Cahuana, P. N. Landin, C. Fager, and T. Eriksson, "Iterative learning control for RF power amplifier linearization," *IEEE Trans. Microw. Theory Techn.*, vol. 64, no. 9, pp. 2778–2789, 2016.

[76] M. B. Yelten, T. Zhu, S. Koziel, P. D. Franzon, and M. B. Steer, "Demystifying surrogate modeling for circuits and systems," *IEEE Circ. Sys. Mag.*, vol. 12, no. 1, pp. 45–63, 2012.

[77] S. Koziel and S. Ogurtsov, "Multi-objective design of antennas using variable-fidelity simulations and surrogate models," *IEEE Trans. Antennas Propag.*, vol. 61, no. 12, pp. 5931–5939, 2013.

[78] I. Couckuyt, S. Koziel, and T. Dhaene, "Surrogate modeling of microwave structures using kriging, co-kriging, and space mapping," *Int. J. Numer. Model.*, vol. 26, no. 1, pp. 64–73, 2013.

[79] D. Gorissen, I. Couckuyt, P. Demeester, T. Dhaene, and K. Crombecq, "A surrogate modeling and adaptive sampling toolbox for computer based design," *J. Machine Learning Research*, vol. 11, no. 68, pp. 2051–2055, 2010.

[80] B. Liu, D. Zhao, P. Reynaert, and G. G. Gielen, "GASPAD: A general and efficient mm-wave integrated circuit synthesis method based on surrogate model assisted evolutionary algorithm," *IEEE Trans. Comput.-Aided Design Integr. Circuits Syst.*, vol. 33, no. 2, pp. 169–182, 2014.

[81] P. Barmuta, F. Ferranti, G. P. Gibiino, A. Lewandowski, and D. Schreurs, "Compact behavioral models of nonlinear active devices using response surface methodology," *IEEE Trans. Microw. Theory Techn.*, vol. 63, no. 1, pp. 56–64, 2014.

[82] C. J. Bastos-Filho, L. M. de Freitas, E. d. A. Barboza, and J. F. Martins-Filho, "Investigating the Creation of a Surrogate Model for Adaptive Control of Amplifier Operating Point Using Machine Learning," in *Int. Conf. Transp. Opt. Net.*, 2020, pp. 1–4.

[83] M. Kaisa, *Nonlinear Multiobjective Optimization*, ser. International Series in Operations Research & Management Science. Boston, USA: Kluwer Academic Publishers, 1999, vol. 12.

[84] N. Wolff, W. Heinrich, and O. Bengtsson, "Highly efficient 1.8-ghz amplifier with 120-mhz class-g supply modulation," *IEEE Trans. Microw. Theory Techn.*, vol. 65, no. 12, pp. 5223–5230, 2017.

[85] R. Pintelon and J. Schoukens, *System identification: a frequency domain approach*. John Wiley & Sons, 2012.

[86] R. H. Byrd, M. E. Hribar, and J. Nocedal, "An interior point algorithm for large-scale nonlinear programming," *SIAM J. Optim.*, vol. 9, no. 4, pp. 877–900, 1999.

[87] G. P. Gibiino, J. Couvidat, G. Avolio, D. Schreurs, and A. Santarelli, "Supply-terminal 40 MHz BW characterization of impedance-like nonlinear functions for envelope tracking PAs," in *Proc. ARFTG Microw. Meas. Conf.*, 2016, pp. 1–4.

[88] P. Bronders, J. Lataire, T. Coppens, G. Pailloncy, S. Gustafsson, Y. Rolain, and G. Vandersteen, "Precompensation of supply dynamics of dynamic power supply transmitters using a linear parameter-varying model," *IEEE Trans. Microw. Theory Techn.*, vol. 67, no. 1, pp. 278–287, 2019.

[89] A. Cidronali, N. Giovannelli, T. Vlasits, R. Hernaman, and G. Manes, "A 240W dual-band 870 and 2140 MHz envelope tracking GaN PA designed by a probability distribution conscious approach," in *IEEE MTT-S Int. Microw. Symp. Dig.*, 2011, pp. 1–4.

[90] Y. Rolain, M. Zyari, E. Van Nechel, and G. Vandersteen, "A measurement-based error-vector-magnitude model to assess non linearity at the system level," in *IEEE MTT-S Int. Microw. Symp. Dig.*, June 2017, pp. 1429–1432.

[91] M. Mengozzi, G. P. Gibiino, A. M. Angelotti, A. Santarelli, C. Florian, and P. Colantonio, "Automatic optimization of input split and bias voltage in digitally controlled dual-input doherty rf pas," *Energies*, vol. 15, no. 13, p. 4892, 2022.

[92] C. F. Campbell, K. Tran, M.-Y. Kao, and S. Nayak, "A k-band 5w doherty amplifier mmic utilizing 0.15 μm gan on sic hemt technology," in *2012 IEEE Compound Semiconductor Integrated Circuit Symposium (CSICS)*, 2012, pp. 1–4.

[93] V. Valenta, I. Davies, N. Ayllon, S. Seyfarth, and P. Angeletti, "High-gain gan doherty power amplifier for ka-band satellite communications," in *2018 IEEE Topical Conference on RF/Microwave Power Amplifiers for Radio and Wireless Applications (PAWR)*, 2018, pp. 29–31.

[94] K. Nakatani, Y. Yamaguchi, Y. Komatsuzaki, S. Sakata, S. Shinjo, and K. Yamanaka, "A ka-band high efficiency doherty power amplifier mmic

using gan-hemt for 5g application," in *2018 IEEE MTT-S International Microwave Workshop Series on 5G Hardware and System Technologies (IMWS-5G)*, 2018, pp. 1–3.

[95] D. J. Shepphard, J. Powell, and S. C. Cripps, "An efficient broadband reconfigurable power amplifier using active load modulation," *IEEE Microw. Wirel. Compon. Lett.*, vol. 26, no. 6, pp. 443–445, 2016.

[96] K. Miettinen, *Nonlinear multiobjective optimization*. Springer Science & Business Media, 2012, vol. 12.

[97] A. M. Angelotti, G. P. Gibiino, T. S. Nielsen, A. Santarelli, and J. Verspecht, "Impact of broadband modulation in active load-pull on-wafer measurements of gan hemts," in *ARFTG Microwave Measurement Conference*, 2022, pp. 1–4.

[98] P. I. Frazier, "Bayesian optimization," in *Recent Advances in Optimization and Modeling of Contemporary Problems*, 2018, pp. 255–278.

[99] C. E. Rasmussen and C. K. I. Williams, *Gaussian processes for machine learning.*, ser. Adaptive computation and machine learning. MIT Press, 2006.

[100] J. Snoek, H. Larochelle, and R. P. Adams, "Practical bayesian optimization of machine learning algorithms," in *Advances in Neural Information Processing Systems*, F. Pereira, C. Burges, L. Bottou, and K. Weinberger, Eds., vol. 25. Curran Associates, Inc., 2012. [Online]. Available: https://proceedings.neurips.cc/paper_files/paper/2012/file/05311655a15b75fab86956663e1819cd-Paper.pdf

[101] J. M. Lafleur, "Heuristic method for identifying concave pareto frontiers in multi-objective dynamic programming problems," *AIAA journal*, vol. 52, no. 3, pp. 496–503, 2014.

[102] G. P. Gibiino, A. M. Angelotti, A. Santarelli, and P. A. Traverso, "Error vector magnitude measurement for power amplifiers under wideband load impedance mismatch: System-level analysis and vna-based implementation," *Measurement*, vol. 187, p. 110254, 2022.

[103] O. Bengtsson, S. Paul, and C. Schulze, "A 26 ghz gan-mmic with integrated switches for discrete level supply modulation," in *IEEE MTT-S Int. Microw. Symp. Dig.*, 2021, pp. 527–530.

[104] N. Wolff, W. Heinrich, and O. Bengtsson, "Class-g supply modulation for mimo and radar with phased array antennas," in *Proc. German Microw. Conf.*, 2019.

[105] C. Nogales, L. Marzall, G. Lasser, and Z. Popovic, "Dynamic supply modulation of a 6 - 12 ghz transmit array," in *IEEE Wireless and Microwave Technology Conf.*, 2023, pp. 140–143.

[106] "Scalable Performance Oscilloscopes, DPO70000SX Series Datasheet, Tektronix, 11 Apr 2023 55W 30662-27," Tektronik.

[107] "Infiniium UXR-B Series Oscilloscopes, Datasheet 3123-1313EN, Keysight Technologies, June 28, 2023," Keysight Technologies.

[108] S. Gustafsson, M. Thorsell, J. Stenarson, and C. Fager, "An oscilloscope correction method for vector-corrected rf measurements," *IEEE Trans. Instrum. Meas.*, vol. 64, no. 9, pp. 2541–2547, 2015.

[109] "RS FSW SIGNAL AND SPECTRUM ANALYZER - Continuing innovation in RF performance and usability, Product Brochure Version 14.00, Rohde und Schwarz, May 2023," Rohde und Schwarz.

[110] "Signal Analyzers X-Series, Product Brochure, 5992-1316EN, Keysight Technologies, March 16, 2023," Keysight Technologies.

[111] G. Avolio, G. Pailloncy, D. Schreurs, M. V. Bossche, and B. Nauwelaers, "On-wafer lsna measurements including dynamic-bias," in *Proc. European Microw. Conf.*, 2009, pp. 930–933.

[112] S. Gustafsson, M. Thorsell, K. Buisman, and C. Fager, "Vector-corrected nonlinear multi-port iq-mixer characterization using modulated signals," in *IEEE MTT-S Int. Microw. Symp. Dig.*, 2017, pp. 1433–1436.

[113] A. M. Angelotti, G. P. Gibiino, T. Nielsen, F. F. Tafuri, and A. Santarelli, "Three port non-linear characterization of power amplifiers under modulated excitations using a vector network analyzer platform," in *IEEE MTT-S Int. Microw. Symp. Dig.*, 2018, pp. 1021–1024.

[114] W. S. El-Deeb, N. Boulejfen, and F. M. Ghannouchi, "A multiport measurement system for complex distortion measurements of nonlinear microwave systems," *IEEE Trans. Instrum. Meas.*, vol. 59, no. 5, pp. 1406–1413, 2010.

[115] M. Litchfield, T. Reveyrand, and Z. Popović, "Load modulation measurements of x-band outphasing power amplifiers," *IEEE Trans. Microw. Theory Techn.*, vol. 63, no. 12, pp. 4119–4129, 2015.

[116] J. Verspecht, A. Stav, J. P. Teyssier, and S. Kusano, "Characterizing amplifier modulation distortion using a vector network analyzer," in *Proc. ARFTG Microw. Meas. Conf.*, 2019, pp. 1–4.

[117] J. Verspecht, T. Nielsen, A. Stav, J. Dunsmore, and J.-P. Teyssier, "Modulation distortion analysis for mixers and frequency converters," in *Proc. ARFTG Microw. Meas. Conf.*, 2020, pp. 1–4.

[118] T. Niubó-Alemán, C. Liang, Y. Hahn, J. A. Reynoso-Hernández, J.-P. Teyssier, and P. Roblin, "Time-domain characterization and linearization of a dual-input power amplifier using a vector network analyzer as

the receiver," *IEEE Trans. Microw. Theory Techn.*, vol. 69, no. 4, pp. 2386–2398, 2021.

[119] A. M. Angelotti, G. P. Gibiino, A. Santarelli, and P. A. Traverso, "Broadband measurement of error vector magnitude for microwave vector signal generators using a vector network analyzer," *IEEE Trans. Intrum. Meas.*, vol. 71, pp. 1–11, 2022.

[120] J. Verspecht, A. Stav, T. Nielsen, and S. Kusano, "The vector component analyzer: A new way to characterize distortions of modulated signals in high-frequency active devices," *IEEE Microw. Mag.*, vol. 23, no. 12, pp. 86–96, 2022.

[121] T. Niubó-Alemán *et al.*, "Calibrated digital predistortion using a vector network analyzer as the receiver," in *Proc. ARFTG Microw. Meas. Conf.*, 2019, pp. 1–4.

[122] C. Schulze, M. Mengozzi, G. P. Gibiino, A. M. Angelotti, C. Florian, A. Santarelli, W. Heinrich, and O. Bengtsson, "A vna-based wideband measurement system for large-signal characterization of multiport circuits," *IEEE Trans. Microw. Theory Techn.*, 2023.

[123] C. Schulze, W. Heinrich, J. Dunsmore, and O. Bengtsson, "Wideband vector corrected measurements on a modified vector network analyzer (vna) system," in *Proc. ARFTG Microw. Meas. Conf.*, 2022, pp. 1–4.

[124] M. Mengozzi, G. P. Gibiino, A. M. Angelotti, C. Florian, A. Santarelli, C. Schulze, and O. Bengtsson, "Modulated-input control and linearization of a multi-port millimeter-wave pa by vna-based calibrated wideband measurements," in *Proc. ARFTG Microw. Meas. Conf.*, 2023, pp. 1–4.

[125] A. Rumiantsev and N. Ridler, "Vna calibration," *IEEE Microw. Mag.*, vol. 9, no. 3, pp. 86–99, Jun. 2008.

[126] T. Reveyrand, A. Courty, M. Portelance, P. Medrel, P. Bouysse, and J.-M. Nébus, "Automatic vector signal generator calibration method suitable for multiport large-signal measurements," in *Proc. ARFTG Microw. Meas. Conf.*, 2019, pp. 1–4.

[127] M. Mengozzi, A. M. Angelotti, G. P. Gibiino, C. Schulze, C. Florian, P. Colantonio, O. Bengtsson, and A. Santarelli, "Wideband automated tuning of ka-band dual input doherty mmic pa using bayesian optimization," in *2023 18th European Microwave Integrated Circuits Conference (EuMIC)*, 2023, pp. 1–4.